



The
University
Of
Sheffield.

**Complex Self-Assembly of Amphiphilic and Polyphilic
Liquid Crystalline Compounds**

By:

Huanjun Lu

A thesis submitted in partial fulfilment of the requirements for the degree of
Doctor of Philosophy

The University of Sheffield
Faculty of Engineering
Department of Materials Science and Engineering

Submission Date 30/09/2017

Acknowledgements

I am most grateful to Dr. Xiangbing Zeng and Professor Goran Ungar for giving me this opportunity to do this challenging research work with financial support in their research group, and for their most valuable guidance, advice and encouragement in all stages of my PhD studies. Without their self-giving help, it would have been impossible for me to finish it.

My special thanks go to Professor Carsten Tschierske and members of his group, of Martin-Luther-University Halle-Wittenberg in Germany, for synthesising those materials and carrying out initial measurements.

I would like to thank Diamond Light Source (U.K.) and European Synchrotron Radiation Facility (France) for providing the beamtimes on different beam lines over the last four years.

I would like to acknowledge the Department of Materials Science and Engineering of the University of Sheffield for the financial support of this work, and staff of the Department of Materials Science and Engineering for their care and attention.

I would like to thank China Scholarship Council (CSC) for their financial support.

I would also like to thank my family for their support. Also, I would give my special thanks to my best friend Qianqian Wang, my boyfriend Fuyuan Tang and my cute kitten Goudaner. Without their understanding and company, I would never be able to conquer the difficulties.

Abstract

One of the most intriguing properties of liquid crystalline compounds is their ability to self-assemble into nanoscale entities, in the simplest cases as layers, columns, or spherical micelles, leading to their many applications in fields such as microelectronics, nanofabrication, medical etc. Understanding how such self-assembly can be controlled through molecular design is hence of paramount importance. Factors such as molecular shape and flexibility, interactions between different moieties, polarity and chirality all contribute to determine the exact mode of self-assembly of such a compound, as well as external controls through the use of temperature, solvent, electric and magnetic field.

In this project three different series of compounds: X-shaped molecules, Polycatenar compounds, and Bolaamphiphiles with swallow-tailed side groups, were examined. Their complex modes of self-assembly have been studied using mainly X-ray diffraction methods, supplemented by Polarized Optical Microscopy, Differential Scanning Calorimetry, and for chiral phases Circular Dichroism Spectroscopy.

In the X-shaped molecules, in addition to “chess-board” two-coloured honeycomb columns with square cross-sections, several complex 3D phases with different tetragonal symmetries have been observed, their structures determined and molecular model constructed.

In polycatenar compounds, we have studied the transitions from a recently found chiral isotropic phase (through dynamic mirror symmetry breaking of achiral compounds) to a bicontinuous cubic phase, either an achiral double network cubic or a chiral triple-network cubic phase. We have also found the formation of chiral SmQ phase in such achiral compounds, and have solved its structure – a long standing puzzle in liquid crystals for more than 30 years. In addition, a number of non-cubic phases, most of them suspected to be bicontinuous, have been identified and for most of them the space group symmetries have been determined, and tentative structural models proposed.

In a number of bolaamphiphiles, with swallow-tailed side groups, a new single-diamond bicontinuous cubic phase has been discovered. The rigid aromatic cores are found to form bundles and such bundles form the segments of the single-diamond network with the side groups filling the rest of the space.

Contents

CHAPTER 1 Introduction1

1.1 Liquid Crystal: General Concept	1
1.1.1 Definition and classification	1
1.1.2 Rod-like molecules and LC phases they form	2
1.1.3 Disc-like molecules and phases they form	2
1.2 T- and X- shaped molecules	3
1.2.1 T-shaped molecules	3
1.2.2 X-shaped molecules	5
1.3 Bicontinuous cubic phases and dynamic mirror symmetry breaking	7
1.3.1 Bicontinuous cubic phases	7
1.3.2 Dynamic mirror symmetry breaking	10
1.4 Aims and objectives	11

CHAPTER 2 Experimental Methods and Analysis14

2.1 Small Angle X-ray Scattering (SAXS)	14
2.1.1 Basic Introduction to SAXS	14
2.1.2 The Set-up of SAXS Experiments	16
2.2 Polarized Optical Microscopy (POM)	17
2.3 Differential Scanning Calorimetry (DSC)	20
2.4 Circular Dichroism (CD) Spectroscopy	21

CHAPTER 3 Liquid Crystalline Structures Formed by X-shaped Polyphiles with semiperfluorinated and Carbosilane Lateral Chains24

3.1 Introduction	24
3.2 Results and discussion	26
3.2.1 High-temperature phase	27
3.2.2 Middle-temperature phase	29
3.2.3 Low-temperature phase	31
3.3 Conclusion	33

CHAPTER 4 Liquid Crystalline Structures Formed by X-shaped Polyphiles with Semiperfluorinated and Hydrocarbon Lateral Chains37

4.1 Introduction	37
4.2 Results and Discussion	38
4.2.1 One-colored p4mm Phase	39
4.2.2 Two-colored p4mm Phase	40
4.2.3 Rectangular p2mm Phase	41
4.2.4 Wigwam-like 3D P4/mmm Phase	44
4.2.5 Re-entrant p2mm Phase	47
4.3 Conclusion	50

CHAPTER 5 Spontaneous Mirror Symmetry Breaking in Polycatenar Molecules by CD Spectroscopy52

5.1 Introduction	52
5.2 Compounds	55
5.3 Results and Discussions	59
5.3.1 SAXS Results	59
5.3.1.1 $Ia\bar{3}d$ Phase	61
5.3.1.2 $Im\bar{3}m$ Phase	64

5.3.1.3 The chiral isotropic liquid phase	67
5.3.2 Chirality changes during phase transitions by CD spectroscopy	67
5.3.2.1 Iso – Iso ^[*] transition in compound A4	69
5.3.2.2 Iso – Iso ^[*] - $Ia\bar{3}d$ phase transitions in compound B8	69
5.3.2.3 Iso – Iso ^[*] - $Im\bar{3}m$ phase transitions in compound B9	71
5.4. Conclusions	73

CHAPTER 6 Smectic-Q Phase – the First Non-cubic Bicontinuous Phase with Orthogonal Twisted Columns75

6.1 Introduction	75
6.2 Results and Discussions	77

CHAPTER 7 Distorted Cubic and Other 3D Phases in Polycatenar Compounds89

7.1 Introduction	89
7.2 Results and Discussions	90
7.2.1 The distorted $Ia\bar{3}d$ phase	90
7.2.2 The distorted $Im\bar{3}m$ phase	96
7.2.3 The diffused $Ia\bar{3}d$ phase	97
7.2.4 The orthorhombic $P2_12_12_1$ phase	98
7.3 Conclusions	103

CHAPTER 8 Double Gyroid and Single Diamond Network Cubic Phases Formed from Bundled Bolaamphiphiles with a Terphenyl Core and a Swallow-Tailed Side Group105

8.1 Introduction	105
8.2 Results and Discussions	107
8.2.1 Compound C16	107
8.2.2 Compound C18	111
8.2.3 Compound C20	115
8.2.4 Compound C22	116
8.3 Conclusion	118
Conclusions and Future Work	119

Chapter 1 Introduction

1.1 Liquid Crystal: General Concept

1.1.1 Definition and classification

Liquid crystal (LC) is a state of matter that is intermediate between liquid and crystal. Like the crystal, a liquid crystal possesses long range orientational or positional order, or both, but often in reduced dimensions (Figure 1.1). At the same time, the molecules in a liquid crystal do not have fixed positions hence liquid crystal is able to flow like a liquid [1,2]. Such unique combination of physical properties of LCs make them an important group of materials for various domestic and industrial applications. The most notable application of LCs is in LC displays, utilizing the anisotropy in the optical properties of LCs, and the abilities for LC molecules to follow the direction of an external electric field [3,4].

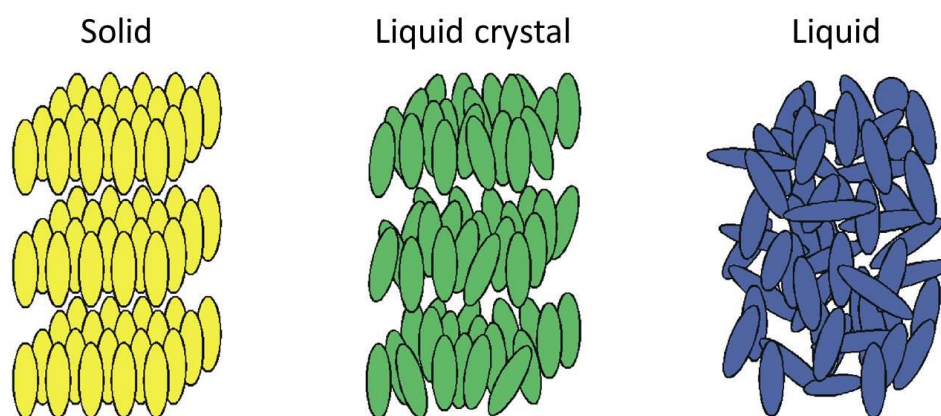


Figure 1.1 Schematic drawings of a rod-like molecule in solid, liquid crystal and liquid phases [5].

Liquid crystals can be classified to be either thermotropic or lyotropic. While in thermotropic LCs the phase transitions are a result of change in sample temperature only, in lyotropics a solvent is used and phase transitions are affected by the type and concentration of solvent as well [1,6,7].

1.1.2 Rod-like molecules and LC phases they form

The simplest LC forming molecules are rod-like. Typically they contain a rigid aromatic rod-like core, which gives molecules required shape anisotropy for the formation of LC phases, and flexible end chains for flexibility and mobility [8]. The most commonly found LC phases in such rod-like molecules are nematic and smectic phases (Figure 1.2). In the nematic phase there is only long range orientational order with no positional order, i.e. the positions of the molecules are random but they tend to orient in the same direction (director n). In the smectic phases, in addition to orientational order, the molecules form layers hence there is 1-dimensional positional order. There are Smectic-A (SmA) and Smectic-C (SmC) phases, depending on whether the director of the molecules n is parallel (SmA) or tilted (SmC) to the layers normal [1,9].

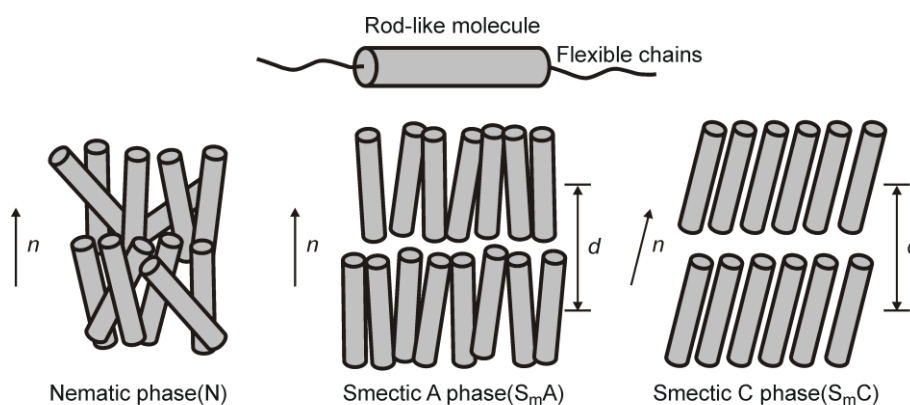


Figure 1.2 Nematic and smectic phases formed by rod-like molecules [5].

1.1.3 Disc-like molecules and phases they form

In disc-like molecules, the rigid aromatic core takes the shape of a disc [1,10,11]. Such disc-like molecules can form nematic, columnar and lamellar columnar phases, as shown in Figure 1.3. In the nematic phase, the director is perpendicular to the discs. In the columnar and lamellar columnar phases, the discs stack on top of each other and form columns, which then pack on 2d (typically hexagonal) or 1d lattices.

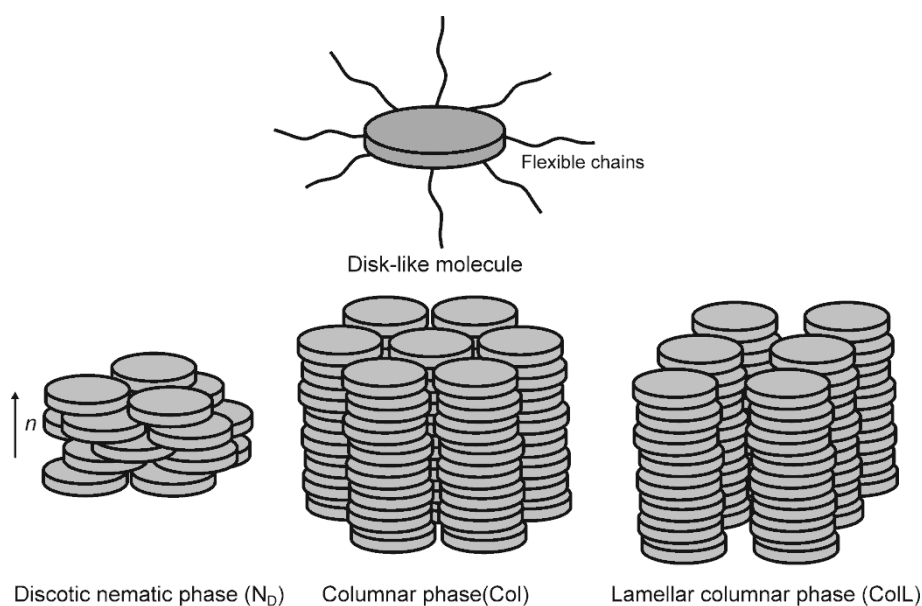


Figure 1.3 Nematic, columnar and lamellar columnar phases formed by disc-like molecules [5].

1.2 T- and X- shaped molecules

1.2.1 T-shaped molecules

T-shaped molecules can be viewed as a modification of the rod-like molecules, by attaching to the rigid rod-like core an extra flexible side-group [12,13]. This simple modification has since been found to be able to produce a rich mine of complex LC phases. There are two major groups of T-shaped molecules called bola-amphiphiles and facial-amphiphiles respectively. In a bola-amphiphile molecule attached to the rigid aromatic core are two hydrogen bonding glycerol end-groups, and an aliphatic (sometimes partially fluorinated) side group. In a facial amphiphile the two end groups are aliphatic, while the side group is hydrophilic.

A summary of different LC phases found in bola-amphiphiles, with increasing length of aliphatic side groups, is schematically shown in Figure 1.4 [14]. When the side chain length is short, smectic phase is formed as in normal rod-like molecules. With increasing length of side groups, honeycomb columnar structures with polygonal cross-sections form. In the honeycomb structures, the rigid aromatic cores form the frameworks of the honeycomb, connected at the corners through hydrogen bonding between their end groups, with side

groups fill the column interior. While the side length of the polygonal honeycombs is determined by the length of the rigid core, the number of sides increases with increasing side group chain length, from rhombic, square, pentagonal, hexagonal, to stretched hexagonal and pentagonal where the side length become twice of that of molecular backbone. Further increase of side chain length leads to the formation of lamellar phase, where side groups and molecular backbones separate into neighbouring layers. Further micro-phase separation between the aromatic core and end groups leads to the formation of nematic (Lam_N) and smectic-like (Lam_{Sm}) substructures in the layers of molecular backbones.

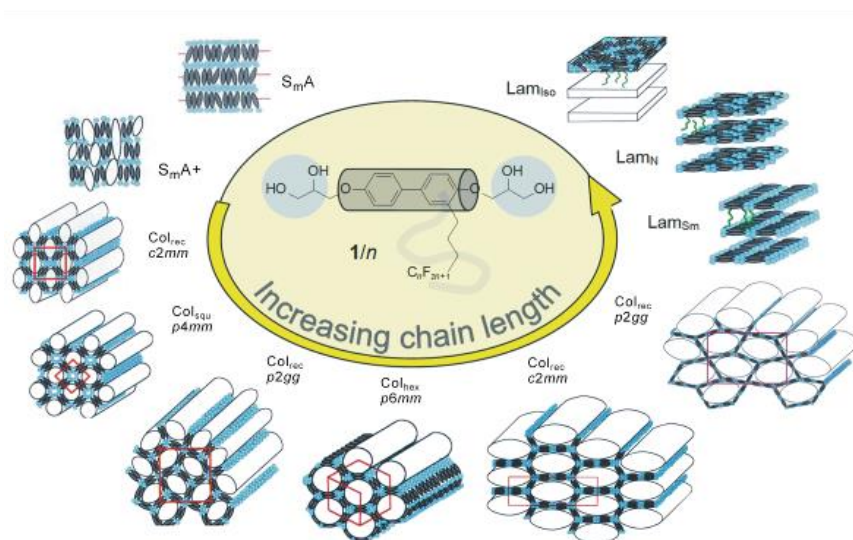


Figure 1.4 LC phases formed by bola-amphiphiles, with increasing chain length of the side group [14].

In facial amphiphiles the chain lengths of both end- and side-groups can be changed [15], with increasing of side chain length has the same effect as decreasing the end chain length. A phase sequence, similar to that found in bola-amphiphiles, from smectic to honeycombs [16] and then to lamellar phases is observed, with the role of end- and side groups simply exchanged. It is also worth mentioning that a 3D hexagonal phase is also found in facial amphiphiles, by polyphilic side groups forming channels penetrating through smectic layers of alternating aromatic cores and aliphatic end groups [17].

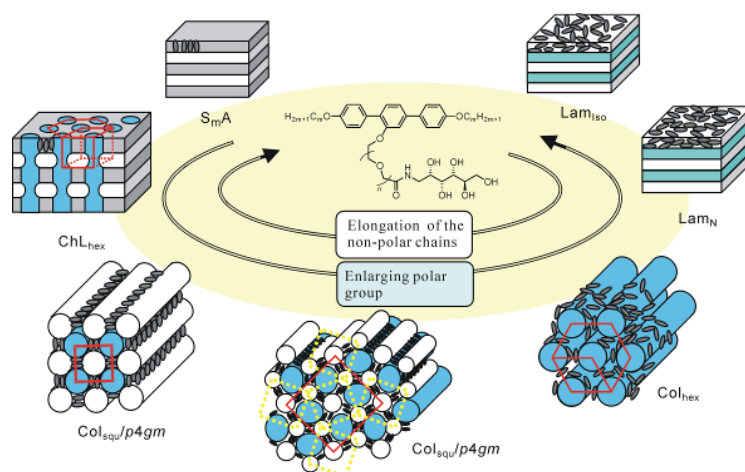


Figure 1.5 LC phases formed by bola-amphiphiles, with changing chain lengths of the end- and side groups [14].

1.2.2 X-shaped molecules

X-shaped molecules are generated by adding two side groups on the opposite sides of the rigid aromatic core (Figure 1.6). If the two side groups are chemically the same or similar, the X-shaped molecules are triphilic like the T-shaped molecules, and they form similar honeycomb columnar structures with polygonal cross-sections. The main difference is that while in T-shaped molecules the walls of the honeycombs are formed by two molecules back-to-back with their side chains pointing in opposite directions, in X-shaped molecules the wall is only one molecule thick, with the two side groups of the same molecules going in two neighbouring honeycomb channels (Figure 1.6) [18].

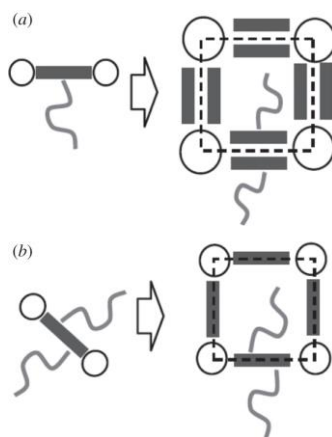


Figure 1.6 Formation of square honeycomb structures from (a) T-shaped molecules and (b) X-shaped molecules [19].

More complex honeycomb structures will result if the two side groups are chemically distinct and X-shaped molecules become tetra/poly-philic. As shown in Figure 1.7, for such a compound as the two side groups tend to form their separate but neighbouring triangular columns, a two-coloured triangular honeycomb phase is formed. The degree of mixing between the two side groups can in fact be tuned by changing temperature, leading to a critical transition between the two-coloured (with phase separated side groups) and single colour (side groups mixed) honeycombs.

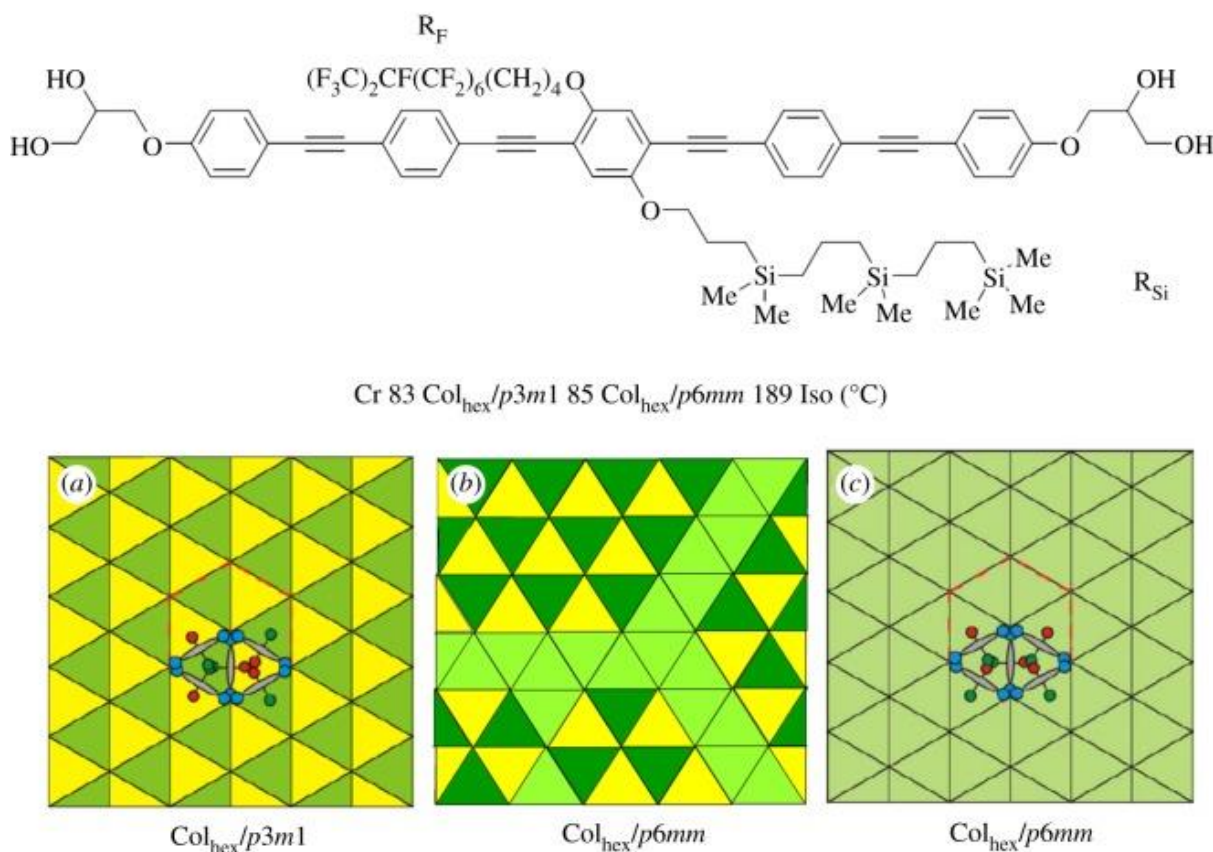


Figure 1.7 Formation of two-coloured (a) and single colour (c) triangular columnar structures from X-shaped molecules. (b) A change of degree of mixing with increasing temperature leads to a critical transition between the two phases [19].

When the sizes of the two side groups are changed relative to each other in the X-shaped molecules, such that the desired shape of polygons occupied by one side group is different to that of the other, more complex LC phases with different corresponding single to multi-coloured tilings of the plane occur. This is further complicated by the geometrical limitation of how a plane can be partitioned by polygons of different shapes. A complete phase separation between the two side groups is not always possible hence a compromise must be found. Examples of such phases are Kagome (triangular + hexagonal columns) [20], two

coloured hexagonal (hexagonal columns with two different degrees of mixing of side groups), mixed triangular, square and rhombic columns (Figure 1.8) [21], giant octagon (combined square, pentagonal and hexagonal columns) [22] and Zeolite structures [23].

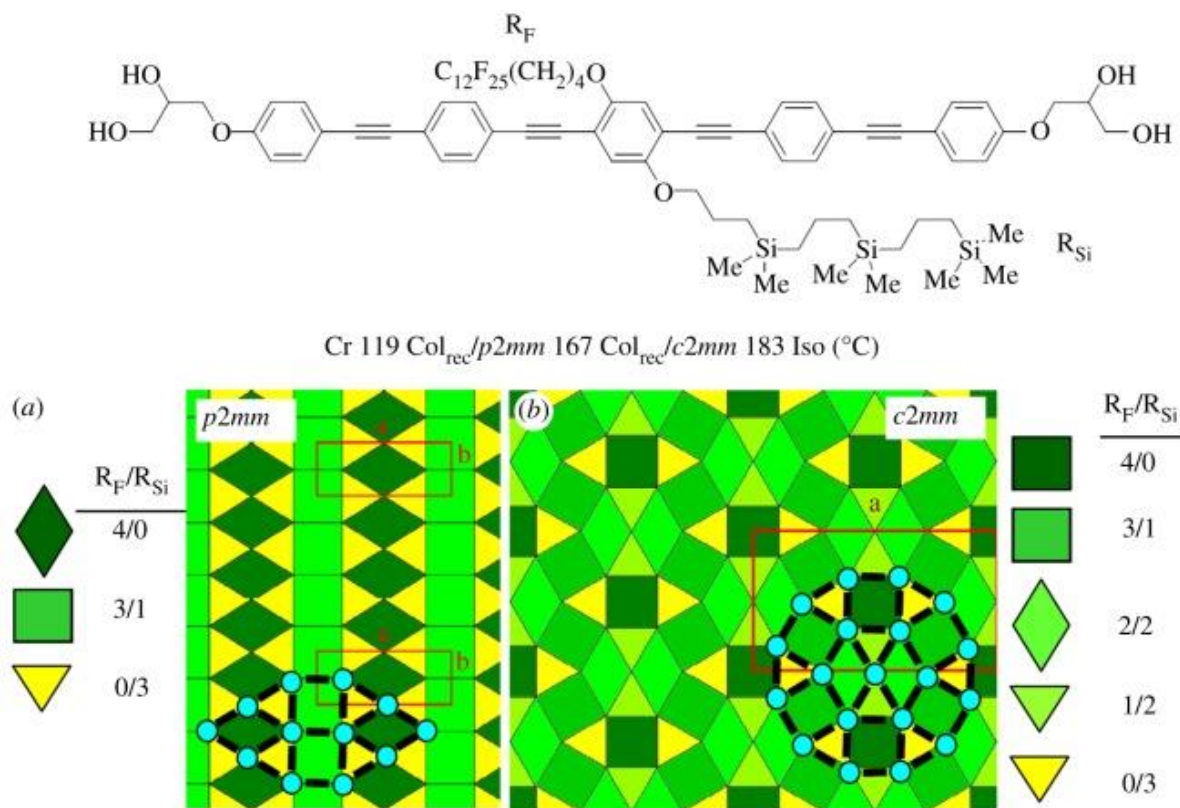


Figure 1.8 Multicolour tilings formed by a polyphilic X-shaped molecule, with (a) three and (b) five different kinds of tiles [19].

1.3 Bicontinuous cubic phases and dynamic mirror symmetry breaking

1.3.1 Bicontinuous cubic phases

Bicontinuous cubic phases are a special group of LC phases formed typically by amphiphilic LC compounds, with cubic symmetry and where the subspaces of both moieties, hydrophilic and hydrophobic for example, are 3-dimensionally continuous. This is in contrast to other LC phases when the molecules self-assemble into discrete layers, columns and micelles. There are three well known examples of such phases, the G (double Gyroid) phase with space group $Ia\bar{3}d$, the D (double Diamond) phase with space group $Pn\bar{3}m$, and the P (Plumber's

nightmare) phase with space group $Im\bar{3}m$) (Figure 1.9) [1]. In all three cases one kind of the moieties of the molecules form two interpenetrating but never intersecting networks, while the other moieties stay around the 3D infinite periodic minimum surface (IPMS) in between the two networks [24]. Each network consists of column like straight segments, branching out at junction points. The number of segments joining each other at each junction, is 3, 4 and 6, respectively for the G, D and P phases. In the LC phase diagram, such cubic phases are often found in between the lamellar and the columnar phases, when one of the moieties of the molecules prefer forming layers while the other moieties prefer forming columns.

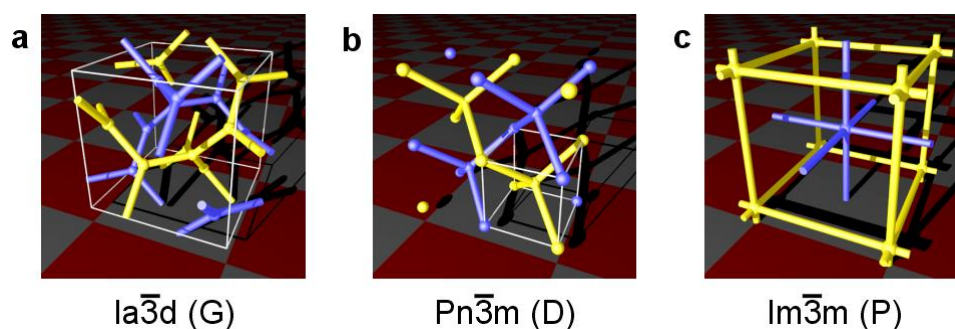


Figure 1.9 Network representation of the three bicontinuous cubic phases [25].

While all three cubic phases have been reported in lyotropic systems, in thermotropic LCs the Gyroid $Ia\bar{3}d$ phase is the most prevalent [26]. Figure 1.10 shows how the Gyroid $Ia\bar{3}d$ phase can be formed by self-assembly from different LC compounds. In inverse lyotropic systems the network channels are occupied by the water [27]; in polycatenar compounds the networks are formed by stacking of rigid cores into columnar segments [28,29,30,31]; in a polysiloxane with polycatenar side groups the networks are taken by the polymer [32]; and in a bola-amphiphile with swallow-tailed side groups, the network segments are formed from axial bundles of the rigid aromatic core (parallel instead of perpendicular to the segment direction) [33]. Recently, the first confirmed $Pn\bar{3}m$ bicontinuous cubic phase is also found to be formed by such bundled bolaamphiphiles (Figure 1.11) [34].

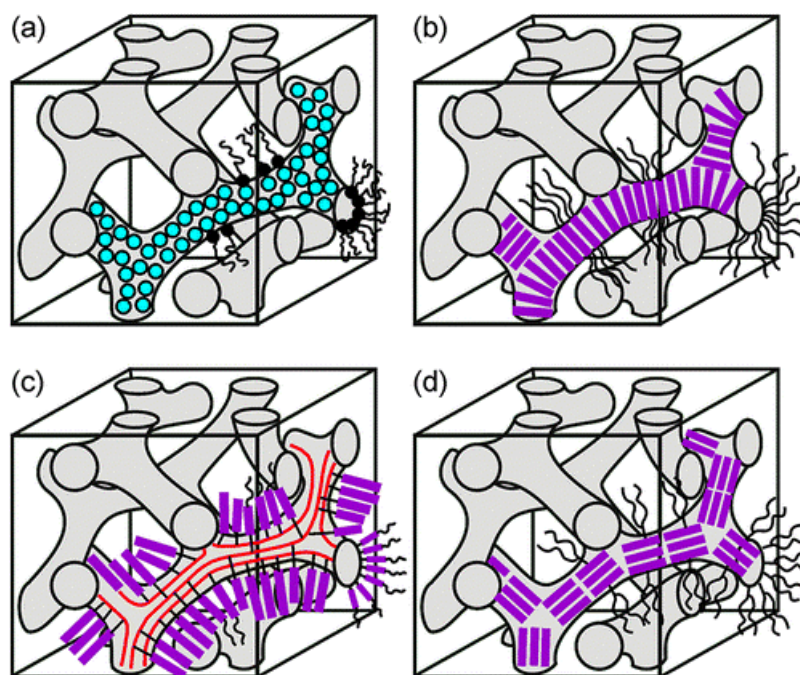


Figure 1.10 Schematic drawings showing how the Gyroid $Ia\bar{3}d$ phase can be formed by self-assembly (a) in an inverse lyotropic phase with water in the channels, (b) in polycatenar thermotropic LCs, (c) in a polysiloxane with hemiphasmid polycatenar side groups, and (d) in a skeletal network structure of H-bonded axial mesogen bundles of bola-amphiphiles with swallow-tailed side groups. [33]

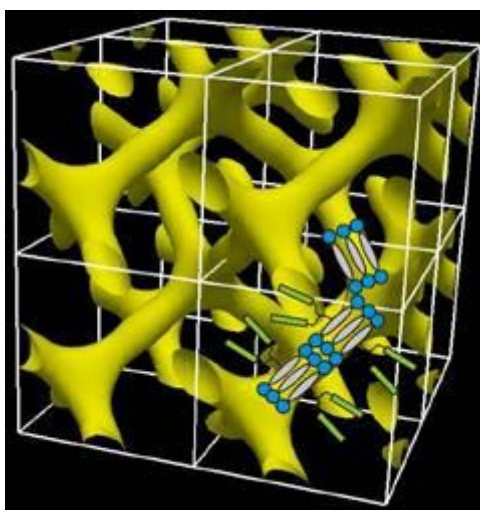


Figure 1.11 Reconstructed electron density map of the bicontinuous $Pn\bar{3}m$ cubic phase. Schematic drawings of molecules overlaid on top show how bundled rigid molecular cores form the straight network segments [34].

Another confirmed thermotropic bicontinuous cubic LC phase has the same $Im\bar{3}m$ symmetry as the P phase mentioned above but a completely different structure. The phase has so far only been found in polycatenar LC compounds. On the basis of a reconstructed electron

density map of the phase, it has been proposed that it has a triple-network structure (Figure 1.12) [25, 35,36], and in which the network segments are formed similarly as shown above in Figure 1.10b. This phase will be called triple-network cubic phase in this thesis, even though a different structural model of the phase, consisting of both networks and micelles, has been proposed by Kutsumizu et al. [37].

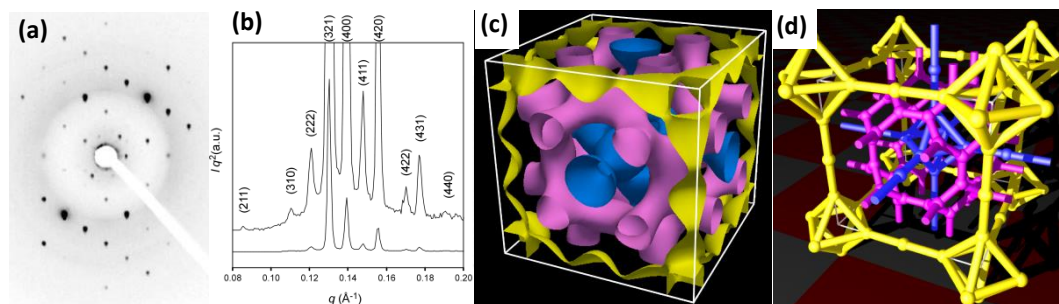


Figure 1.12 X-ray diffraction patterns of the triple network cubic phase of (a) a single crystal sample and (b) a powder sample. (c) Reconstructed electron density map showing high electron density regions and (d) its network representation [25].

1.3.2 Dynamic mirror symmetry breaking

More recently, optical studies (POM and CD spectroscopy) have demonstrated that the triple network cubic phase, despite it being observed in achiral polycatenar compounds, is in fact chiral. On the other hand, the double network $Ia\bar{3}d$ phase, is always achiral [38,39]. Moreover, a chiral isotropic phase ($Iso^{[*]}$) has also been found in some of these compounds at temperatures above their cubic phases, before it transforms to the normal achiral isotropic phase (Iso) [40]. On the basis of such observations, it has been proposed that the rigid aromatic cores of polycatenar molecules form chiral columns, by molecular twist along network segments (Figure 1.13). The handedness of the chiral segments must be kept the same to avoid clashes at network junctions, as a consequence each network in the $Ia\bar{3}d$ and the triple network cubic phases, must be homochiral. While in the $Ia\bar{3}d$ phase the space group symmetry enforces that the two networks have exactly the opposite handedness, so that there is no overall chirality of the phase. In the $Im\bar{3}m$, phase the handedness of the three networks are either the same, or they do not cancel each other completely.

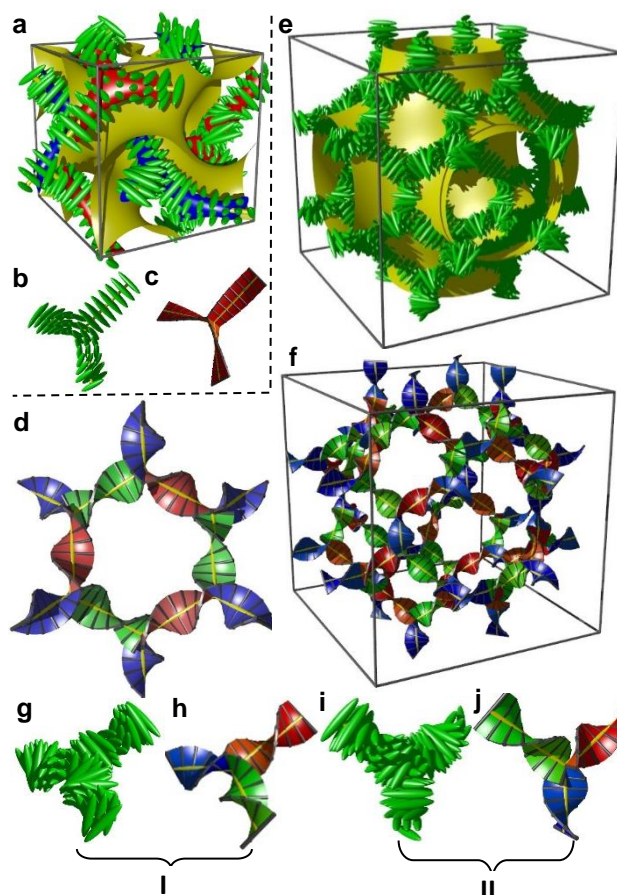


Figure 1.13 (a-c) The two networks (red and blue) of the $Ia\bar{3}d$ phase decorated with schematic mesogens (rod-like molecular cores, green) showing the molecular twist along the network segments. The gyroid minimum surface is also shown (yellow). (d-j) The same but for the middle of the three networks of the triple-network cubic phase. This network closely follows the Schwartz P-type minimum surface (shown in yellow). [38]

1.4 Aims and objectives

The aim of this PhD project is to understand the principles of self-assembly by studying polyphilic molecules with different designed geometry.

More specifically, these include

- X-shaped molecules which form chess-board honeycomb structures and related complex 3D phases (Chapter 3 and 4);
- The formation of chiral/achiral isotropic/cubic phases and their transitions in achiral polycartenar molecules (Chapter 5);

- The structure of the chiral tetragonal SmQ phase observed in achiral compounds (Chapter 6) and many other related chiral/achiral cubic/noncubic phases (Chapter 7).
- Study of the single diamond network bicontinuous $Fd\bar{3}m$ phase found in bolaamphiphiles with swallow-tailed side groups (Chapter 8).

References

1. D. Demus et al., Handbook of Liquid Crystals. Vol. 1-3. 1998. Wiley-VCH: Weinheim, Germany.
2. K. Satyendra, Liquid crystals: experimental study of physical properties and phase transitions. 2001, Cambridge University Press, UK.
3. H. Kawamoto, The history of liquid-crystal displays. Proceedings of the IEEE, 2002. 90(4): p. 460-500.
4. D. Pauluth and K. Tarumi, *Journal of Materials Chemistry* 2004, **14**, 1219.
5. F. Liu, Complex Supramolecular Self-assembly of T- and X-shaped Amphiphiles. PhD thesis, University of Sheffield, 2009.
6. G. Vertogen, Thermotropic liquid crystals, fundamentals. 1987. Springer-Verlag, Berlin.
7. C. Fong, T. Le and C. J. Drummond, *Chem. Soc. Rev.* 2012, **41**, 1297.
8. S. Chandrasekhar, Liquid Crystals, 1992. 2nd Edition, Cambridge University Press, UK.
9. G. W. Gray, Smectic liquid crystals: textures and structures, 1984. Leonard Hill, Glasgow.
10. S. Kumar, *Chem. Soc. Rev.* 2006, **35**, 83.
11. S. Kumar, Chemistry of discotic liquid crystals: from monomers to polymers, 2011. Taylor & Francis, London.
12. M. Kolbel, T. Beyersdorff, X. H. Cheng, C. Tschierske, J. Kain and S. Diele, *J. Am. Chem. Soc.* 2001, **123**, 6809.
13. C. Tschierske, *Nature* 2002, **419**, 681.
14. X. Cheng, M. Prehm, M. K. Das, J. Kain, U. Baumeister, S. Diele, D. Leine, A. Blume and C. Tschierske, *J. Am. Chem. Soc.* 2003, **125**, 10977.
15. B. Chen, U. Baumeister, G. Pelzl, M. K. Das, X. Zeng, G. Ungar and C. Tschierske, *J. Am. Chem. Soc.* 2005, **127**, 16578.
16. B. Chen, X. B. Zeng, U. Baumeister, G. Ungar and C. Tschierske, *Science* 2005, **307**, 96.
17. B. Chen, X. B. Zeng, U. Baumeister, S. Diele, G. Ungar and C. Tschierske, *Angew. Chem., Int. Ed.* 2004, **43**, 4621.
18. R. Kieffer, M. Prehm, B. Glettner, K. Pelz, U. Baumeister, F. Liu, X. B. Zeng, G. Ungar and C. Tschierske, *Chem. Commun.* 2008, **0**, 3861.

19. C. Tschierske, C. Nürnberger, H. Ebert, B. Glettner, M. Prehm, F. Liu, X. B. Zeng and G. Ungar, *Interface Focus* 2012, **2**, 669.
20. B. Glettner, F. Liu, X. B. Zeng, M. Prehm, U. Baumeister, M. Walker, M. A. Bates, P. Boesecke, G. Ungar and C. Tschierske, *Angew. Chem. Int. Ed.* 2008, **47**, 9063.
21. X. B. Zeng, R. Kieffer, B. Glettner, C. Nürnberger, F. Liu, K. Pelz, M. Prehm, U. Baumeister, H. Hahn, H. Lang, G. A. Gehring, C. H. M. Weber, J. K. Hobbs, C. Tschierske and G. Ungar, *Science*, 2011, **331**, 1302.
22. F. Liu *et al.*, *Nature Comm.* 2012, **3**, 1104.
23. S. Poppe, A. Lehmann, A. Scholte, M. Prehm, X. B. Zeng, G. Ungar and C. Tschierske, *Nature Comm.* 2015, **6**, 8037.
24. A. H. Schoen, Infinite periodic minimal surfaces without intersections (NASA Technical Note D-5541, Washington DC).
25. X. B. Zeng, G. Ungar and M. Impéror-Clerc, *Nature Materials* 2005, **4**, 562.
26. S. Diele, *Curr. Opin. Colloid Interface Sci.* 2002, **7**, 333.
27. S. M. Gruner, *J. Phys. Chem.* 1989, **93**, 7562.
28. A. M. Levelut and M. Clerc, *Liq. Cryst.* 1998, **24**, 105.
29. S. Kutsumizu, *Curr. Opin. Solid State Mater. Sci.* 2002, **6**, 537.
30. M.A. Alam, J. Motoyanagi, Y. Yamamoto, T. Fukushima, J. Kim, K. Kato, M. Takata, A. Saeki, S. Seki, S. Tagawa and T. Aida, *J. Am. Chem. Soc.* 2009, **131**, 17722
31. S. N. Chvalun, M. A. Shcherbina, A. N. Yakunin, J. Blackwell and V. Percec, *Polym. Sci. Ser. A* 2007, **49**, 158.
32. G. Ungar and V. Percec, resented at the 14th International Liquid Crystal Conference, Pisa, Italy, 1992.
33. F. Liu, M. Prehm, X. B. Zeng, C. Tschierske and G. Ungar, *J. Am. Chem. Soc.* 2014, **136**, 6846.
34. X. B. Zeng, M. Prehm, G. Ungar, C. Tschierske and F. Liu, *Angew. Chem. Int. Ed.* 2016, **55**, 8324.
35. M. Impéror-Clerc, *Curr. Opin. Colloid Interface Sci.* 2005, **9**, 370.
36. X. B. Zeng, L. Cseh, G. H. Mehl and G. Ungar, *J. Mater. Chem.* 2008, **18**, 2953.
37. K. Ozawa, Y. Yamamura, S. Yasuzuka, H. Mori, S. Kutsumizu and K. Saito, *J. Phys. Chem. B* 2008, **112**, 12179.
38. C. Dressel, F. Liu, M. Prehm, X. B. Zeng, G. Ungar, and C. Tschierske, *Angew. Chem. Inter. Ed.* 2014, **126**, 13331.
39. S. Kutsumizu, S. Miisako, Y. Miwa, M. Kitagawa, Y. Yamamura and K. Saito, *Phys.Chem.Chem.Phys.* 2016, **18**, 17341.
40. C. Dressel, T. Reppe, M. Prehm, M. Brautzsch and C. Tschierske, *Nature Chem.* 2014, **6**, 971.

Chapter 2 Experimental Methods and Analysis

2.1 Small Angle X-ray Scattering (SAXS)

2.1.1 Basic Introduction to SAXS

Compared with normal crystals, liquid crystals only have periodic order at molecular level, resulting in sharp Bragg peaks at low diffraction angles. In this way, Small angle X-ray scattering (SAXS), which usually records the elastic scattering of X-ray at scattering angle below 5° , provides an essential method to investigate the structure of liquid crystals. The principle of SAXS is the same as normal X-ray diffraction [1]. A beam of incident X-ray will diffract when passing through a crystal. The relationship between the reflecting lattice planes (or Miller planes) of spacing d and the angle of reflection θ obeys Bragg's Law, which is:

$$n\lambda = 2d\sin\theta \quad (2.1)$$

Where n is an integer (the order of reflection or diffraction), λ is the wavelength of the incident X-ray. In the experiments, we usually use the first order diffraction, *i.e.* $n=1$. This is based on the fact that the n^{th} order diffraction of lattice plane with Miller indices (h, k, l) , is the same as the first order diffraction of the plane with indices (nh, nk, nl) .

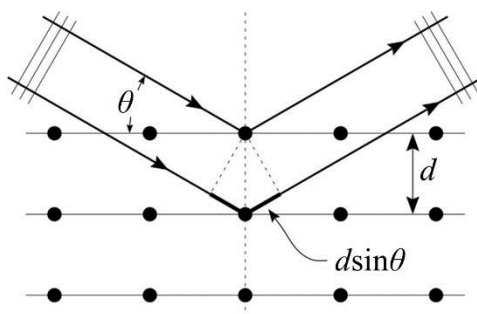


Figure 2.1 Scheme of Bragg's Law: parallel rays reflected from points on neighbouring planes. The angle of incidence/reflection to the planes is θ . The lattice plane spacing is d . Hence the path difference is $2d\sin\theta$.

In order to have a clearer way to describe the lattice and the crystal structure, a reciprocal space vector \vec{q} is defined. Its value is shown below:

$$q = \frac{4\pi}{\lambda} \sin \theta \quad (2.2)$$

Combining equations (2.1) and (2.2), the q value of a diffraction peak is simply $2\pi/d$, where d is the spacing of the corresponding lattice planes. Consequently a one-to-one relationship can be established between vector \vec{q} of a diffraction peak, and Miller planes in a periodic lattice. This leads to an alternative way of defining \vec{q} , utilizing the concept of reciprocal lattice. While a periodic crystal lattice can be described by three unit cell vectors \vec{a} , \vec{b} and \vec{c} , for a (hkl) Miller plane the corresponding vector $\vec{q}_{(hkl)}$ equals to $h\vec{a}^* + k\vec{b}^* + l\vec{c}^*$. Thus,

$$\begin{aligned} q^2_{(hkl)} &= (h\vec{a}^* + k\vec{b}^* + l\vec{c}^*) \cdot (h\vec{a}^* + k\vec{b}^* + l\vec{c}^*) \\ &= h^2 a^{*2} + k^2 b^{*2} + l^2 c^{*2} + 2hka^* b^* \cos\gamma + 2klb^* c^* \cos\alpha + \\ &\quad 2hla^* c^* \cos\beta \end{aligned} \quad (2.3)$$

This equation provides the basis, from the positions (q or 2θ) of X-ray diffraction peaks, for their indexing and determination of lattice parameters, and from there the assignment of lattice types and space groups of the periodic structures.

The other important information of an X-ray diffraction pattern is the intensities of the diffraction peaks, and the contribution of each molecule in a unit cell to that is a vector. This vector can be expressed as a complex number $A \cdot \exp(i\phi)$, with the amplitude A proportional to the atomic scattering factor f , and phase angle ϕ depends on the positions of atoms in the unit cell \vec{r} . The contributions from all atoms in a unit cell simply add together and result in the structure factor $F(\vec{q}_{hkl})$. Thus,

$$\begin{aligned} F(\vec{q}_{hkl}) &= \sum_j f_j \exp(i\vec{r}_j \cdot \vec{q}) = \sum_j f_j \exp[2\pi i(hx_j + ky_j + lz_j)] \\ &= \sum_j f_j \cos[2\pi(hx_j + ky_j + lz_j)] + i \sum_j f_j \sin[2\pi(hx_j + ky_j + lz_j)] \end{aligned} \quad (2.4)$$

Where $2\pi(hx_j + ky_j + lz_j)$ is the phase angle ϕ_j of the j^{th} atom in the unit cell with fractional coordinates (x_j, y_j, z_j) .

Since in molecules and atoms the predominant contributor to X-ray scattering are electrons, a crystal structure can be expressed by its electron density distribution $\rho(\vec{r})$ in the unit cell. Subsequently, the structure factor can be expressed by:

$$F(\vec{q}) = \int \rho(\vec{r}) \exp(i\vec{r} \cdot \vec{q}) d\vec{r} \quad (2.5)$$

Mathematically, the structure factor $F(\vec{q})$ is the Fourier transform of the electron density distribution $\rho(\vec{r})$. Equation 2.5 can be rewritten as:

$$\begin{aligned} F(\vec{q}) &= \int_{-\infty}^{+\infty} \rho(\vec{r}) \exp(i\vec{r} \cdot \vec{q}) d\vec{r} \\ &= \int_{-\infty}^0 \rho(\vec{r}) \exp(i\vec{r} \cdot \vec{q}) d\vec{r} + \int_0^{\infty} \rho(\vec{r}) \exp(i\vec{r} \cdot \vec{q}) d\vec{r} \\ &= \int_0^{\infty} \rho(-\vec{r}) \exp(-i\vec{r} \cdot \vec{q}) d\vec{r} + \int_0^{\infty} \rho(\vec{r}) \exp(i\vec{r} \cdot \vec{q}) d\vec{r} \end{aligned} \quad (2.6)$$

In X-ray crystallography, the diffraction intensity measures the square of the structure factor amplitude $|F(\vec{q})|^2$ only, in this case, the scalar magnitude $F(\vec{q})$ can be obtained from the experiments, but the information about the phase angles is lost. For a centrosymmetric structure, the electron density of $\rho(x, y, z)$ equals to that of $\rho(-x, -y, -z)$. In this case, the equation can be simplified as:

$$\begin{aligned} F(\vec{q}) &= \int_0^{\infty} \rho(-\vec{r}) \exp(-i\vec{r} \cdot \vec{q}) d\vec{r} + \int_0^{\infty} \rho(\vec{r}) \exp(i\vec{r} \cdot \vec{q}) d\vec{r} \\ &= \int_0^{\infty} \rho(\vec{r}) \exp(-i\vec{r} \cdot \vec{q}) d\vec{r} + \int_0^{\infty} \rho(\vec{r}) \exp(i\vec{r} \cdot \vec{q}) d\vec{r} \\ &= 2 \int_0^{\infty} \rho(\vec{r}) \cos(\vec{r} \cdot \vec{q}) d\vec{r} \end{aligned} \quad (2.7)$$

As the imaginary part of the scattered wave is zero, when the value of the structure factor is positive, the phase angle is zero. When it's negative, the phase angle is π .

Considering that the Fourier transformation is reversible, the electron density ρ can be described as:

$$\begin{aligned} \rho(x, y, z) &= \int F(\vec{q}) \exp(-i\vec{r} \cdot \vec{q}) d\vec{q} = \sum_{hkl} F(hkl) \exp(-i\vec{r} \cdot \vec{q}) \\ &= \sum_{hkl} F(hkl) \exp[-2\pi i(hx + ky + lz)] \end{aligned} \quad (2.8)$$

Combined with the information about the shape of the molecule, the volume and electron density of each moiety, the proper phase combination can be determined. Thus the electron density map can be reconstructed.

2.1.2 The Set-up of SAXS Experiments

The SAXS experiments were carried out mostly using synchrotron beamtime at the Diamond Light Source. The synchrotron beam is produced by accelerating electrons

in a curved orbit through a magnetic field. When the high-speed electrons change their direction, a series of photons with different energies, such as X-rays, will be released. As the flux of the photons is very high, extremely high intensity beams can be generated. In this thesis, powder samples were used in SAXS experiments. The samples were prepared in 1.0mm glass capillaries and then fixed on the Linkam hot stage. The error of the temperature measurement can be controlled within ± 0.2 °C. Pilatus P3-2M 2D detector is used to record the diffraction patterns. Simultaneous WAXS is also recorded, which is particularly useful in determining whether a phase is liquid crystalline or crystalline. A beam stop is put in front of the detector to protect the detector against damage from the direct beam.

2.2 Polarized Optical Microscopy (POM)

Polarized optical microscopy (POM) [2] is considered as one of the most fundamental research methods when dealing with liquid crystal samples. With the help of the POM experiments, the liquid crystalline phase transition temperatures can be determined, and certain LC phase types can be identified from their typical textures.

In a polarized optical microscope, there are two crossed polarizing filters (the polarizer and the analyzer). When both of them are inserted into the optical path without the sample, no light can pass through and the field of view is dark. However, if an optically anisotropic sample is put between these two filters, the polarization state of the light will be changed and thus coloured pictures can be seen. One example of an optical anisotropic material is a liquid crystal. In a liquid crystal, the refraction index of a polarized incident beam is dependent on its orientation to the optical axis of the liquid crystal. Consequently, when a beam of light passes through a LC sample, it will split into two components which are an ordinary ray (perpendicular) and an extraordinary ray (parallel). These two rays are polarized perpendicular to each other. As they have different refractive indices (n_o and n_e), the two beams propagate through sample at different speeds (v_o and v_e). The phase difference Γ between the two components at depth d can be defined as:

$$\Gamma = \frac{2\pi}{\lambda}(n_e - n_o)d \quad (2.9)$$

where λ is the wavelength of the incident light beam. As a consequence, the incident linearly polarized light becomes elliptical polarized and thus can pass through the crossed analyzer. The intensity I of the observed light is given by:

$$I = I_0 \sin^2 2\theta \sin^2 \frac{\Gamma}{2} \quad (2.10)$$

where I_0 is the intensity of the emergent light from the polarizer, θ is the angle between the polarizer and the optical axis of the sample. According to this equation, in the homeotropically aligned region, where $\theta = 0$, the field of view will be dark. Also, the brightness of the field of view would change during the rotation of the sample.

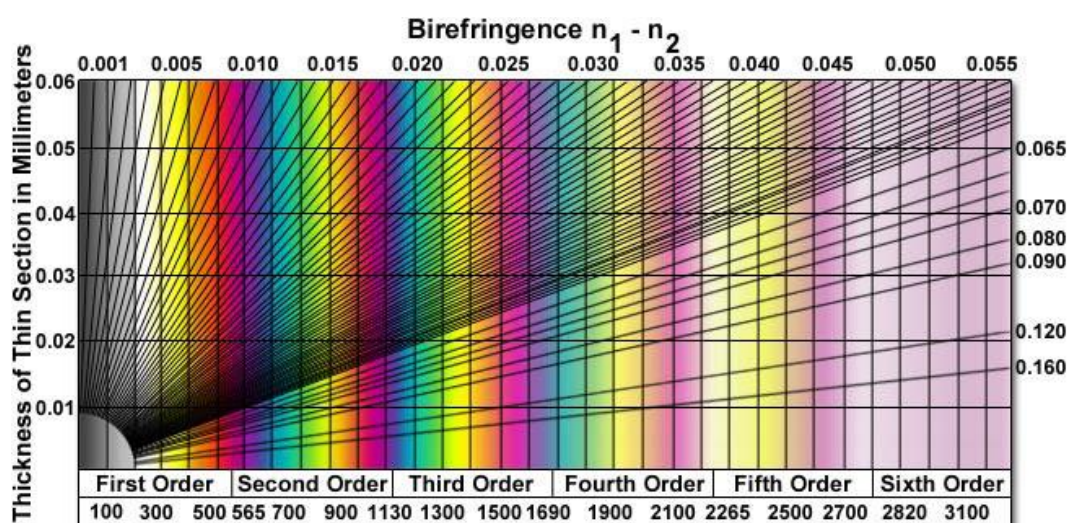


Figure 2.2 The interference colour chart. The interference colour can be correlated with the actual retardation (bottom horizontal axis), thickness (left hand vertical axis), and birefringence (top and right hand axes) of the sample. If two of the three variables are known, the remaining one can be determined by drawing a line from the lower left hand corner to the upper and right hand boundaries. [3]

In order to have a better understanding of the orientation of the molecules, a retardation plate is often used in POM experiments. The retardation plate is made from anisotropic materials, which can slow down the propagating speed in a certain direction. By convention, the northeast-southwest direction is usually the slow axis of the retardation plate. This retardation results in a change of the presented color. For all the possible retardations, the interference color can be plotted on a chart as shown in Figure 2.2. To make the condition easier and clearer, we usually prepare samples which start with the first-order grey. In the case of a $1-\lambda$ retardation plate is used, the retardation in the slow axis would be 550 nm. If the northeast-southwest direction is

also the slow direction of the sample, then the presented color will be second-order blue. Otherwise, if the slow axis is the fast direction of the sample, then first-order yellow will be observed.

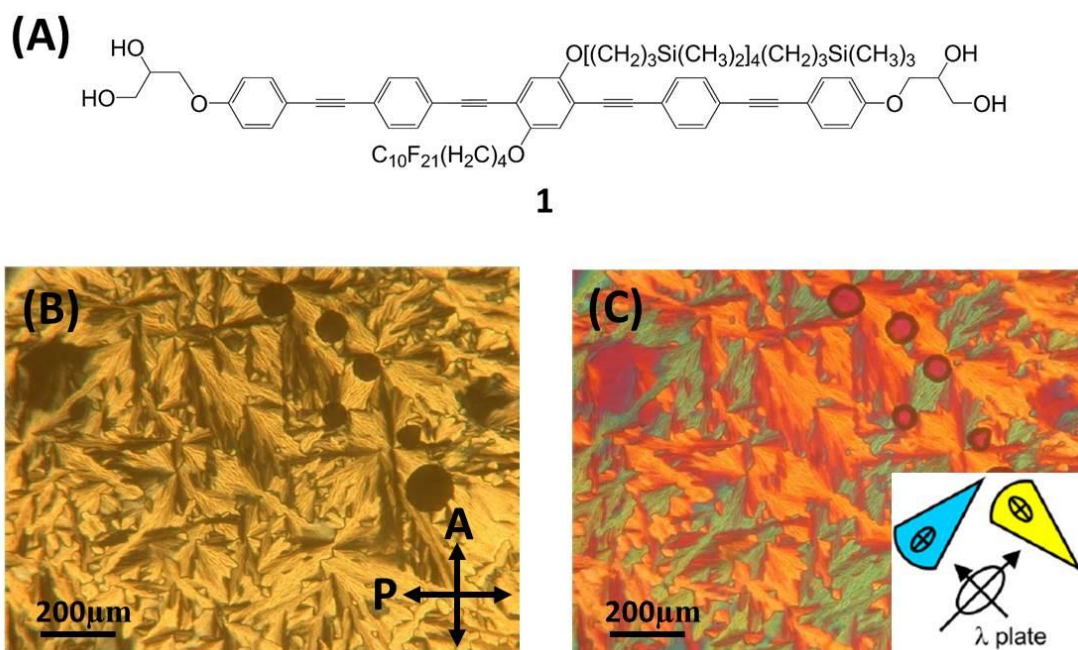


Figure 2.3 (A) Molecular structure of compound **1**; (B) Texture between crossed polarizers at $T = 105\text{ }^{\circ}\text{C}$; (C) Texture recorded at the same temperature with λ retarder plate; in the fans the high-index axis is radial; The indicatrix orientation in the λ -plate and in the two types of fans is shown in the inset.

As an example, X-shaped compound **1** shows optical textures typical for columnar phase at $T = 105\text{ }^{\circ}\text{C}$ (see Figure 2.3B). Indicated by the textures recorded with a λ retardation plate, the high refractive axis, which is also the long axis of the p-conjugated cores, is parallel to the blue fans (see Figure 2.3C). Thus, the X-shaped molecules lie radially in the fans. Since the columns are tangential, the molecules are perpendicular to the columns.

The microscope used in this thesis is an Olympus BX-50. A $1-\lambda$ retardation plate is added in some of the experiments. The light source is incandescent. A digital camera and the Image-Pro Plus software from MediaCybernetics are used to capture and process the optical textures.

2.3 Differential Scanning Calorimetry (DSC)

Differential scanning calorimetry [4] is a thermal analysis technique, which measures the different amount of heat required by the sample and reference during heating and cooling. When the sample undergoes phase transitions, glass transitions or chemical reactions, it will absorb or release heat. To keep both the sample and the reference at the same temperature, a thermal compensator will increase or decrease the heat which flows to the sample. If an endothermic process takes place, for example, the phase transition from solid to liquid, more heat is required to flow to the sample. On the contrary, an exothermic phase transition requires less heat.

The result of a DSC experiment is a curve shows the relationship between the heat flux (vertical axis) and the temperature or time (horizontal axis). If there is no phase transition or other reactions, it's only the difference caused by the specific heat capacities of the sample and the reference need to be compensated. In this case, the baseline of the experiment is obtained. To maintain a flat and smooth baseline, the reference should have a stable heat capacity and have no reactions in the experimental temperature range. When a thermal reaction takes place, a positive or negative peak is shown. By integrating the peak, the enthalpy of the transition can be calculated by the following equation:

$$\Delta H = KA \quad (2.11)$$

where ΔH is the enthalpy of transition, K is the calorimetric constant, and A is the area under the curve. For different instruments, the calorimetric constant is different. To measure the constant, a standard sample which has stable thermal performances and known enthalpies of transitions can be analyzed.

Differential scanning calorimetry is now widely used in many research fields, such as liquid crystals, polymers, oxidative stability and drug analysis. With this technique, the small phase transitions, as well as the transitions temperatures and the enthalpies can be observed and analyzed.

2.4 Circular Dichroism (CD) Spectroscopy

Circular dichroism (CD) [5] refers to the property of a chiral material which has different absorption of left-handed and right-handed Circularly polarized lights. CD spectroscopy offers a useful method to measure the chirality of optically active chiral molecules. Its basic principle is explained below.

Electromagnetic radiation is a transverse wave, which consists of an electric and a magnetic field. These two fields oscillate perpendicular to each other and to the propagating direction. When the oscillation of the electric field is in a single plane, linearly polarized light is produced. If a horizontal linearly polarized light and a vertical linearly polarized light are added together, then a variety of linearly or non-linearly polarized light can be obtained. For example, when the horizontal and the vertical linearly polarized light have the same amplitude and are in phase with each other, a linear light polarized at 45 degrees is shown. Moreover, when they are out of phase by a quarter-wave, a helix, which known as circularly polarized light occurs. In a circularly polarized light, the electric field vector has a constant magnitude and rotates helically along the propagation direction. The circularly polarized light can be either left-handed or right-handed.

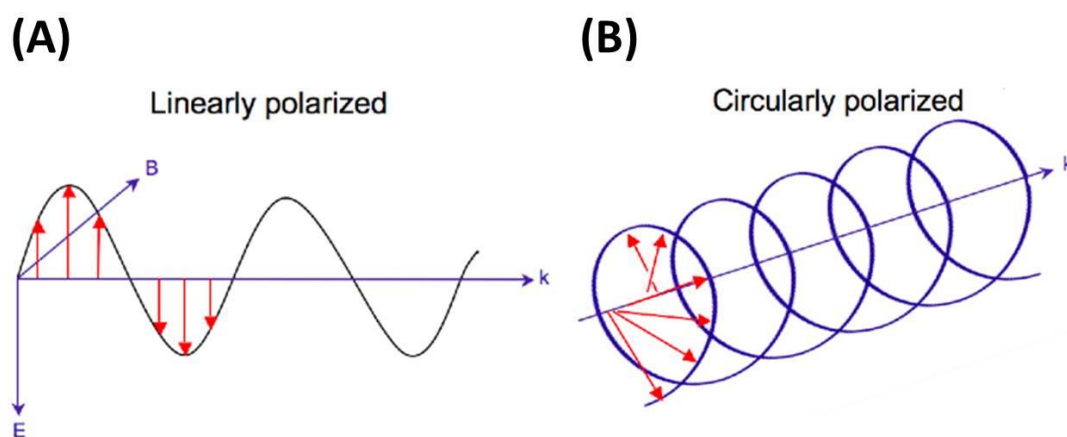


Figure 2.4 Electric (E) and magnetic (B) field vectors in linearly polarized light (A) and circularly polarized light (B); the red arrows show the direction of the electric field vector [6].

According to Lambert-Beer law:

$$I = I_0 \exp(-\epsilon t) \quad (2.12)$$

where I and I_0 are the intensity of the transmitted and incident light, respectively; ε is extinction coefficient; t is time. For chiral materials, the left-handed and right-handed lights are absorbed to different extents:

$$\varepsilon_L \neq \varepsilon_R \quad (2.13)$$

Thus, the magnitudes of the electric field vectors of the right-circularly and left-circularly polarized light are different. When the two components are added together, elliptically polarized light is produced (see Figure 2.5).

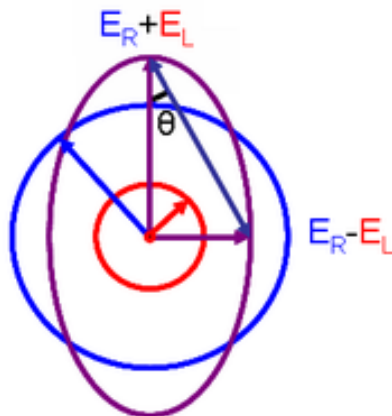


Figure 2.5 Elliptical polarized light (violet) is composed of unequal contributions of right (blue) and left (red) circular polarized light; E_R and E_L are the magnitudes of the electric field vectors of the right-circularly and left-circularly polarized light, respectively; θ is ellipticity of the polarization [6].

Circular dichroism is the difference between the extent to the absorbed right-handed light and left-handed light:

$$\Delta\varepsilon = \varepsilon_R - \varepsilon_L \quad (2.14)$$

In CD spectroscopy experiments, the chirality is reported by the degrees of ellipticity of the polarization θ . By definition,

$$\tan\theta = \frac{E_R - E_L}{E_R + E_L} \quad (2.15)$$

where E_R and E_L are the magnitudes of the electric field vectors of the right-circularly and left-circularly polarized light, respectively. Since the intensity I of light is proportional to the square of the electric-field vector E^2 , thus,

$$\tan\theta \propto (I_R - I_L)^{1/2} \propto (\varepsilon_R - \varepsilon_L)^{1/2} \quad (2.16)$$

In this thesis, the CD experiments were carried out at station B23, Diamond light source. The high photon flux, as well as the small cross section (about 1mm x 2mm)

of the beam, improves the signal-to-noise of the experiments and enables the measurement of smaller volumes of sample. The spectral range we used is from 200 to 500 nm. Experimental data are recorded by a photo multiplier tube. The samples are prepared by melting between two quartz plates. Then the plates are placed on top of a Linkam hot stage for temperature control during the experiment.

References

1. International Tables for Crystallography, Volumes A and B, 2006, Dordrecht : Published for the International Union of Crystallography by Kluwer Academic,
2. L. C. Sawyer, Polymer Microscopy, 1987, London : Chapman and Hall.
3. W. Nesse, Introduction to Optical Mineralogy, 1991, Oxford University Press, New York. 2nd Edition.
4. G. W. H. Hoehne, Differential Scanning Calorimetry : an Introduction for Practitioners, 1996, Berlin; London: Springer.
5. N. Kobayashi, A. Muranaka and J. Mack, Circular Dichroism and Magnetic Circular Dichroism Spectroscopy for Organic Chemists, 2012, Cambridge: RSC publishing.
6. Wikipedia, https://en.wikipedia.org/wiki/Circular_dichroism, accessed sept. 2017.

Chapter 3

Liquid Crystalline Structures Formed by X-shaped Polyphiles with semiperfluorinated and Carbosilane Lateral Chains

3.1 Introduction

The self-assembled structures observed in block copolymers have attracted much attention owing to their diverse morphologies and potential applications¹⁻⁶. Numerous ordered structures, such as columnar, lamellar, spherical and tubular phases can be produced through microphase segregation or self-assembly of block copolymers²⁻⁶. Block copolymers with functional groups can also offer opportunities for the investigations of the correlations between nanostructure and functionality⁷⁻¹¹. Especially, liquid crystalline (LC) block copolymers can provide a method to explore the influence of the topological structures of block copolymers on their liquid crystalline phase behavior, the arrangement of mesogenic units, as well as the meso-phase transitions¹²⁻¹⁵. Nowadays, LC block copolymers with well-designed morphologies have been investigated in developing advanced functional materials especially in some aspects like optics, electronics and photo-responsive materials¹⁶⁻²⁴. Compared with traditional linear-linear LC block copolymers, LC polymers with special topological structures, such as star-branched molecules, have more functional groups and better defined morphologies, so they are expected to form more complex and interesting soft-matter structures instead of simple lamellar, nematic and columnar LC phases^{15, 25-27}. In star-branched LC compounds, some of them are produced by connecting mesogenic units to the end of the star-branched polymers, the others are synthesized by replacing the side-chains of bolaamphiphiles and facial amphiphiles²⁸. For the latter ones, their liquid crystalline characteristics are given by the incompatibilities of different moieties rather than mesogenic groups. These molecules with two or more incompatible components are also call

polyphiles^{29, 30}. A variety of interesting LC structures have been reported by these kind of star-branched LC polyphiles^{31, 32}.

In this chapter, we explored an X-shaped polyphile and studied its LC phase behavior at different temperatures. With the help of small angle X-ray scattering (SAXS) and many other research techniques, the structure of each phase can be accurately defined. Moreover, reconstructed electron density maps and relevant computer simulations are also carried out to confirm the structures as well as give a suitable model for the packing of molecules.

3.2 Results and discussion

The X-shaped compound **1** consists of a rigid rod-like aromatic core with a carbosilane and a semiperfluorinated alkyl chain attached laterally to opposite sides of the aromatic moiety. The molecular structure is shown in Figure 3.1.

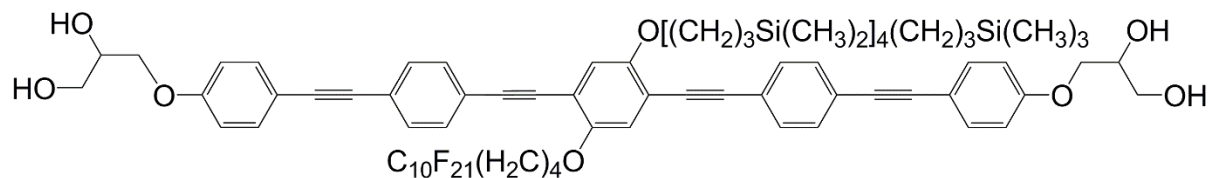


Figure 3.1 Molecular structure of compound **1**

We studied the phase behavior of this compound on cooling. SAXS results shows that this compound forms 3 different phases in the temperature range between 86 and 130 °C (Figure 3.2).

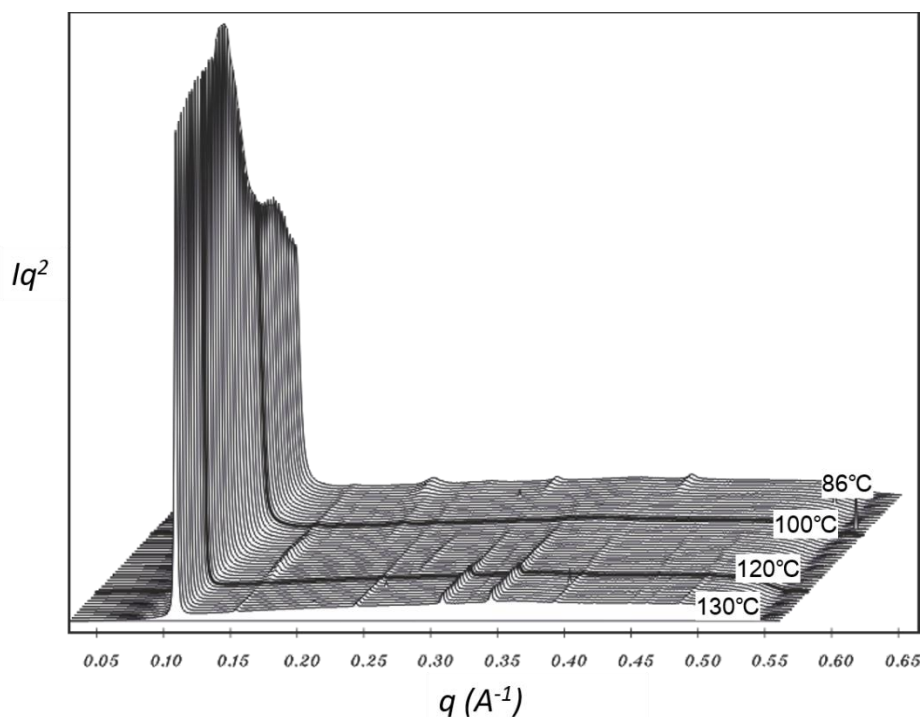


Figure 3.2 Continuous heating run of compound **1** from 86 °C to 130 °C (back to front), SAXS diffractograms were recorded every 1 °C; the horizontal axis is scattering factor q ; the vertical axis is Lorentz-corrected intensity; $P4/mmm$ phase is formed below 100 °C; between 100 °C and 120 °C, it's $I4/mmm$ phase; above 120 °C, $p4mm$ phase is shown.

3.2.1 High-temperature phase

The high-temperature phase occurs between 130 and 120 °C. The diffraction pattern of compound **1** at 130 °C is shown in Figure 3.3A.

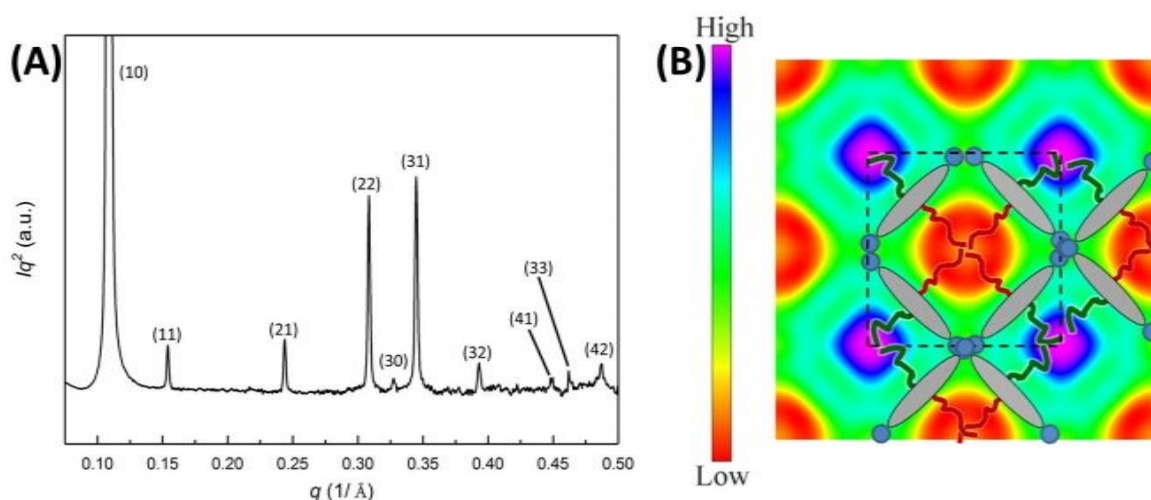


Figure 3.3 (A) SAXS diffraction pattern of compound **1** at 130 °C; (B) Reconstructed electron density map of the high-temperature phase, in the molecule model, the red moiety stands for the carbosilane chain and the green stands for the semiperfluorinated chain

Table 3.1 Experimental and calculated d -spacings of the observed SAXS reflections of the square phase in compound **1** at 130 °C. All intensities values are Lorentz and multiplicity corrected.

(hk)	$d_{\text{obs.}} - \text{spacing} / \text{Å}$	$d_{\text{cal.}} - \text{spacing} / \text{Å}$	intensity	phase
(10)	57.8	57.8	100	π
(11)	40.8	40.9	0.49	π
(20)	28.9	28.9	0.04	0
(21)	25.8	25.8	0.67	π
(22)	20.4	20.4	2.74	0
(30)	19.2	19.3	0.10	π
(31)	18.2	18.3	3.19	0
(32)	16.0	16.0	0.31	0
(41)	14.0	14.0	0.14	0
(33)	13.6	13.6	0.18	π
(42)	12.9	12.9	0.47	π
$a = 57.8 \text{ Å}$				

According to the SAXS results above, the reflections can be indexed on a square lattice, plane group $p4mm$, with the lattice parameter $a = 57.8 \text{ Å}$. The length of the rigid aromatic moiety measured in *Materials Studio* is 39.5 Å , so the lattice parameter a is about $\sqrt{2}$ times to the length of the aromatic rod. Considering this relationship, the aromatic rods may lie perpendicularly as a square in a lattice with the vertices in the middle of each edge of the lattice. We also reconstructed an electron density map to further investigate the arrangement

of the molecules (Figure 3.3B). In this electron density map, the high-density purple region is made up of the semiperfluorinated chains and the low-density red region is filled with the carbosilane chains. It can be seen from the electron density map that both the high-density and the low-density regions form squares with the middle-density green region acting as boundaries. Combined with the length of the molecule, it suggests that the aromatic moieties form a chessboard-like square honeycomb net with carbosilane and semiperfluorinated chains filling the alternative “chessboard” cells.

Simulations are also carried out to confirm the proposed structure. Both of the scattering factor of the carbosilane moiety (f_a) and the semiperfluorinated moiety (f_b) contribute to the structure factor F . The coordinate of the carbosilane moiety is considered as (0, 0), thus the coordinate of the semiperfluorinated moiety should be $(\frac{1}{2}, \frac{1}{2})$. The structure factor F is also corrected by Gaussian function. The simulation equations and procedure are showed below.

$$f_a = \frac{4 \sin(q_x a) \sin(q_y a)}{q_x q_y} \text{ (if } q_y = 0, f_a = \frac{4a \sin(q_x a)}{q_x} \text{),}$$

$$f_b = \frac{4 \sin(q_x b) \sin(q_y b)}{q_x q_y} \text{ (if } q_y = 0, f_b = \frac{4b \sin(q_x b)}{q_x} \text{),}$$

$$F = f_a * s_a + f_b \cos(\pi h + \pi k) * s_b,$$

$$G(q) = F \exp\left(-\frac{q^2 * l_n^2}{q_0^2}\right)$$

Table 2 Simulations for compound **1** at 130 °C

hk	$d / \text{Å}$	$q / \text{Å}^{-1}$	$q_x / \text{Å}^{-1}$	$q_y / \text{Å}^{-1}$	f_a	f_b	F_{hkl}	$F_{hkl} * G(q)$	Intensity (cal.)	Intensity (obs.)
10	57.8	0.109	0.077	0.077	-539	275	-815	-782	100	100
11	40.8	0.154	0.154	0	-312	230	-82.4	-76.0	0.94	0.49
20	28.9	0.217	0.154	0.154	-121	163	42.3	35.9	0.21	0.04
21	25.8	0.243	0.231	0.077	18.8	126	-107	-87.1	1.24	0.67
22	20.4	0.308	0.308	0	172	42.2	215	155	3.93	2.74
30	19.2	0.327	0.231	0.231	-0.66	57.2	-57.9	-40.1	0.26	0.10
31	18.2	0.345	0.309	0.154	66.9	29.2	96.0	63.9	0.67	3.19
32	16.0	0.393	0.385	0.077	95.4	-27.4	123	72.5	0.86	0.31
41	14.0	0.449	0.458	0.274	2.70	-16.6	19.3	9.67	0.02	0.14
33	13.6	0.462	0.462	0	-22.9	-66.3	-89.2	-43.0	0.30	0.18
42	12.9	0.487	0.462	0.154	-8.87	-47.0	-55.9	-24.8	0.10	0.47

(Edge length of the carbosilane square $a = 14.0 \text{ Å}$, edge length of the semiperfluorinated square $b = 9.0 \text{ Å}$, the height parameter $s_a = -1.03$, $s_b = 1$, Gaussian parameter $q_0 = 0.45$)

The simulation shows that the calculated intensities can fit the observed intensities quite well. Thus it can further support our predicted structure about the high-temperature phase.

3.2.2 Middle-temperature phase

The middle-temperature phase occurs between 120 and 100 °C. The diffraction pattern of compound **1** at 110 °C is shown in Figure 3.4A.

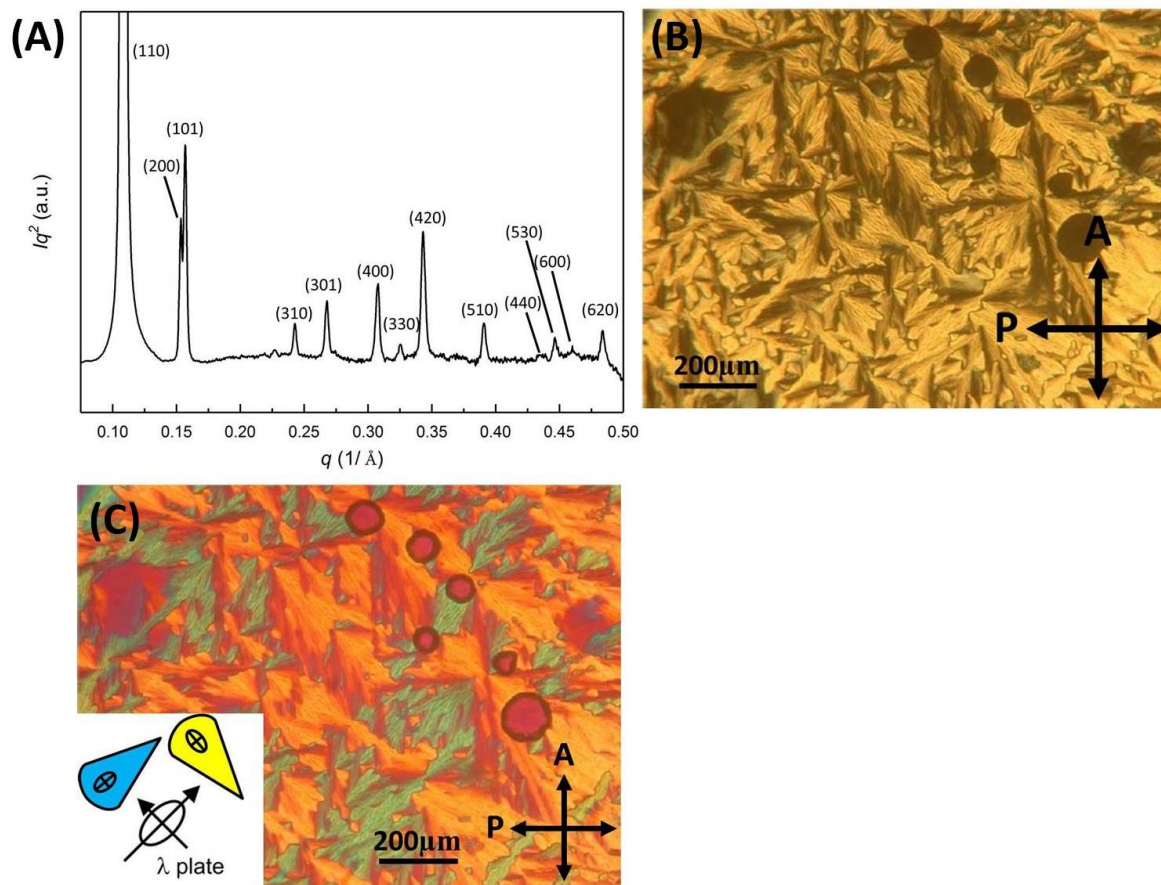


Figure 3.4 (A) SAXS diffraction pattern of compound **1** at 110 °C; (B) Texture between crossed polarizers at $T = 105$ °C; (C) Texture recorded at the same temperature with λ retarder plate; in the fans the high-index axis is radial; The indicatrix orientation in the λ -plate and in the two types of fans is shown in the inset.

Table 3.3 Experimental and calculated d -spacings of the observed SAXS reflections of the square phase in compound **1** at 110 °C. All intensities values are Lorentz and multiplicity corrected.

(hkl)	$d_{\text{obs.}} - \text{spacing} / \text{Å}$	$d_{\text{cal.}} - \text{spacing} / \text{Å}$	intensity	phase
(110)	57.8	57.8	100	π
(200)	40.8	40.9	1.55	0
(101)	40.2	40.2	1.63	0
(220)	28.9	28.9	0.017	0
(310)	25.7	25.8	0.30	0
(301)	23.4	23.5	0.71	0
(400)	20.4	20.4	0.89	
(330)	19.2	19.2	0.12	π
(420)	18.2	18.3	1.53	π
(510)	16.0	16.0	0.43	

(440)	14.4	14.4	0.012	
(530)	14.1	14.0	0.20	
(600)	13.6	13.6	0.055	
(620)	12.9	12.9	0.47	
$a = 81.7 \text{ \AA}, c = 46.2 \text{ \AA}$				

The reflections can be indexed on a body centred tetragonal lattice, space group $I4/mmm$, with the lattice parameter $a = 81.7 \text{ \AA}$, $c = 46.2 \text{ \AA}$. Combined with the texture of this phase, which contains the Maltase crosses and homeotropically aligned regions, it indicates a columnar liquid crystalline phase. Indicated by the texture recorded with a λ retardation plate, the high refractive axis, which is also the long axis of the p-conjugated cores, is parallel to the blue fans (Figure 3.4C). Thus, the X-shaped molecules lie radially in the fans. Since the columns are tangential, the molecules are perpendicular to the columns. In the reconstructed electron density map (Figure 3.5), the high-density blue columns are filled with semiperfluorinated chains and the red ones are carbosilane columns. Different from the high-temperature phase, these columns are not straight. Their radii change periodically along the columnar axis. This is because that in this compound, the carbosilane chain is more flexible than the semiperfluorinated chain. When the temperature decreases, the carbosilane chains will shrink more than the semiperfluorinated chains. They can't form a "chessboard" anymore. So the carbosilane columns tend to distort and even break down to fit the decrease of volume.

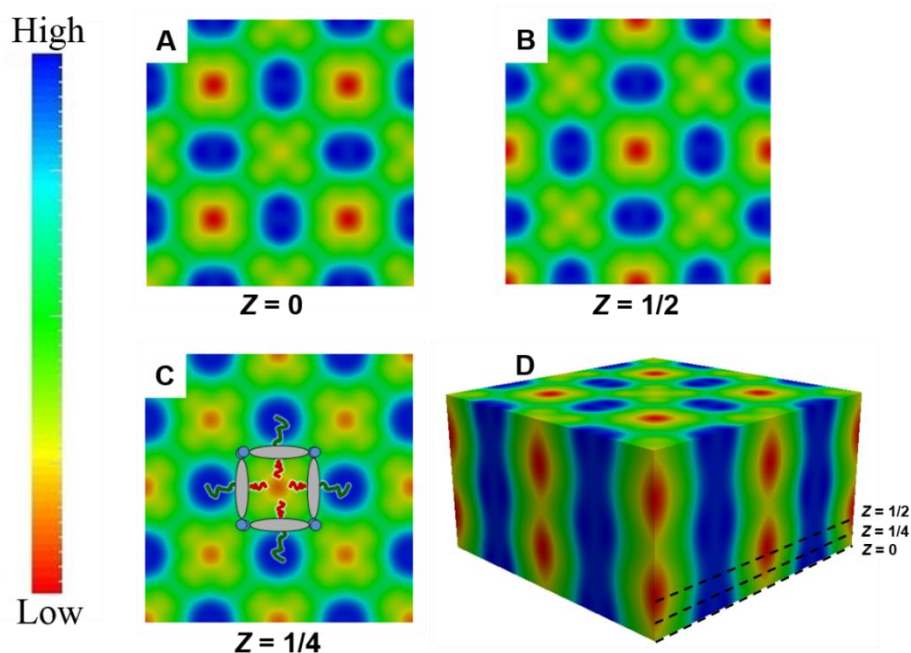


Figure 3.5 Reconstructed electron density map of the middle-temperature phase

3.2.3 Low-temperature phase

The low-temperature phase occurs between 100 and 86 °C. The diffraction pattern of compound **1** at 90 °C is shown in Figure 3.6.

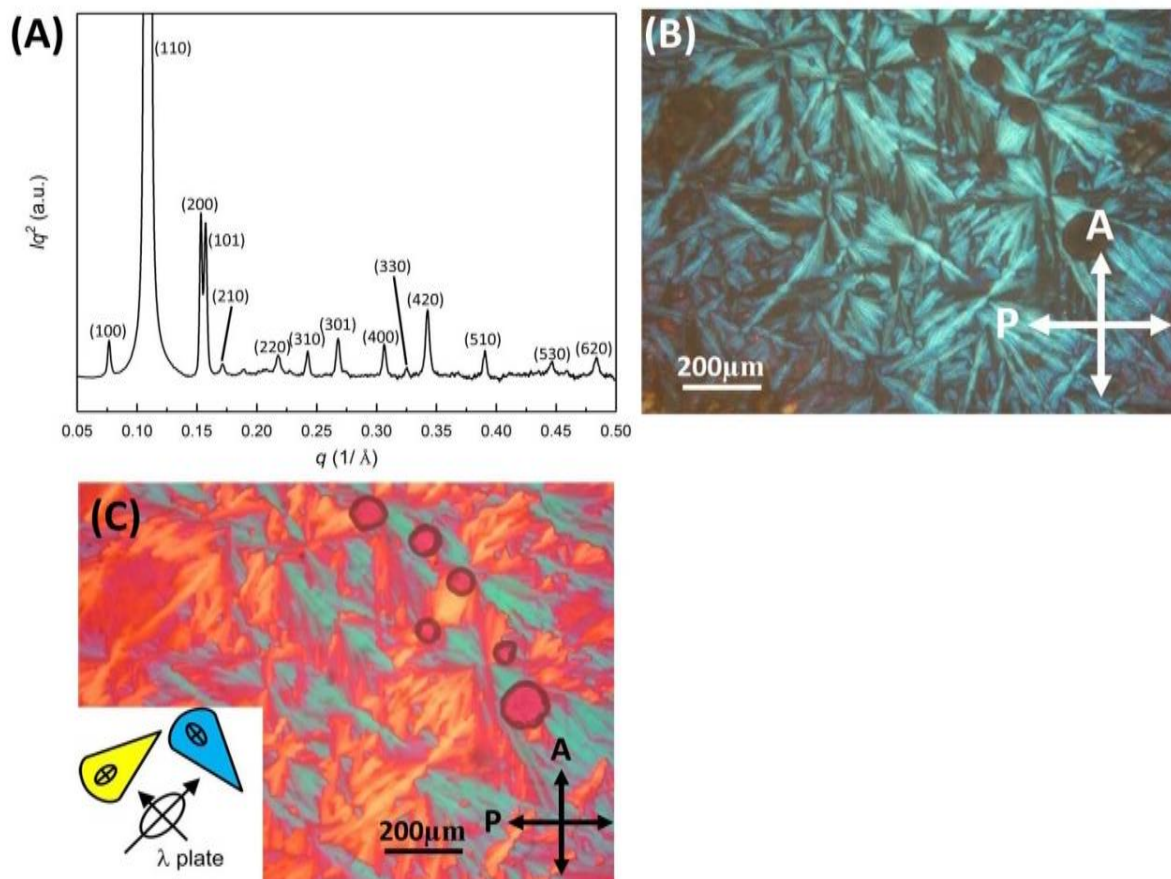


Figure 3.6 (A) SAXS diffraction pattern of compound **1** at 90 °C; (B) Texture between crossed polarizers at $T = 95$ °C; (C) Texture recorded at the same temperature with λ retarder plate; in the fans the high-index axis is radial; The indicatrix orientation in the λ -plate and in the two types of fans is shown in the inset.

Table 3.4 Experimental and calculated d -spacings of the observed SAXS reflections of the square phase in compound **1** at 90 °C. All intensities values are Lorentz and multiplicity corrected.

(hkl)	$d_{\text{obs.}} - \text{spacing} / \text{\AA}$	$d_{\text{cal.}} - \text{spacing} / \text{\AA}$	intensity	phase
(100)	82.1	82.0	0.85	π
(110)	57.8	58.0	100	π
(200)	41.0	41.0	0.89	0
(101)	39.9	39.9	0.92	0
(210)	36.7	36.7	0.041	π
(220)	28.9	29.0	0.066	0
(310)	25.9	25.9	0.058	0
(301)	23.5	23.4	0.081	0
(320)	22.7	22.7		
(400)	20.5	20.5	0.052	
(410)	19.9	19.9		

(330)	19.4	19.3	0.010	
(420)	18.3	18.3	0.10	π
(430)	16.4	16.4		
(510)	16.1	16.1	0.026	
(520)	15.3	15.2		
(440)	14.6	14.5		
(530)	14.1	14.1	0.0075	
(600)	13.7	13.7		
(610)	13.5	13.5		
(620)	13.0	13.0	0.020	
$a = 82.0 \text{ \AA}, c = 45.7 \text{ \AA}$				

The reflections can be indexed on a tetragonal lattice, space group $P4/mmm$, with the lattice parameter $a = 82.0 \text{ \AA}$, $c = 45.7 \text{ \AA}$. Similarly with the middle-temperature phase, the texture of this phase also suggests a liquid crystalline columnar phase. However, when adding a λ -plate to the polarizer, the texture of the low-temperature phase (Figure 3.6C) shows an inversion of the birefringence in the middle-temperature phase (Figure 3.4C). While in the homeotropically aligned regions, the birefringence remain the same. This result indicates that the orientation of the columns doesn't change and the aromatic rods in the cylinder walls may have different directions.

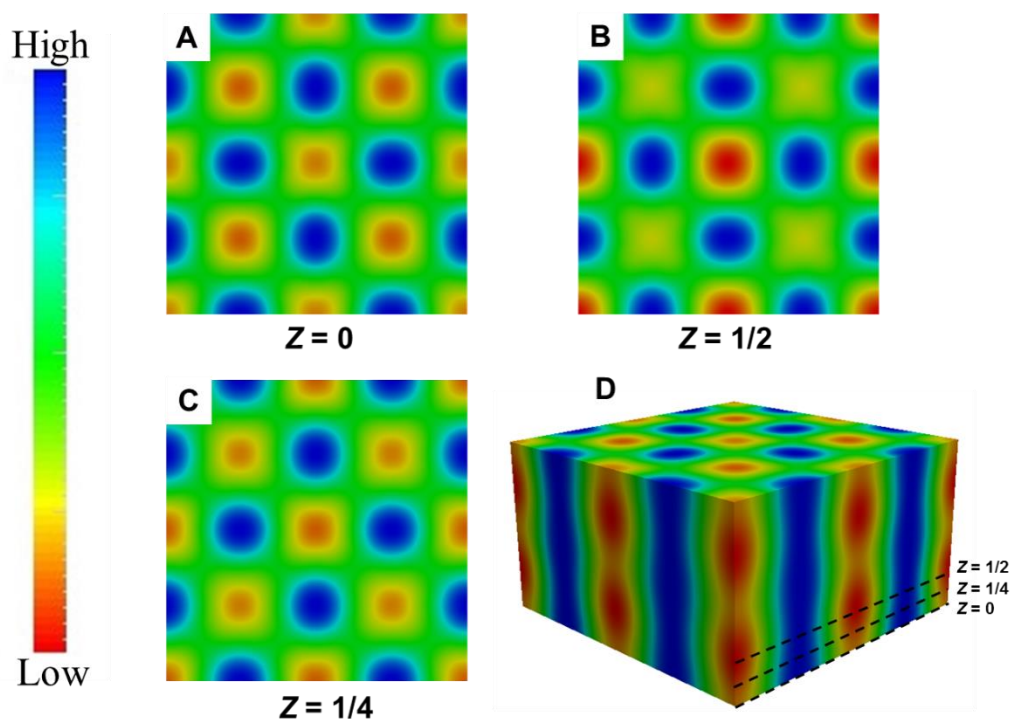


Figure 3.7 Reconstructed electron density map of the low-temperature phase

The electron density map shows that all the columns are again continuous. However, one of the two carbosilane columns now has a significantly reduced cross-section. Polarized optical micrographs show that birefringence had reversed from negative to positive upon the transition from middle-temperature phase to low-temperature phase, implying that some aromatic rods had reoriented from being normal to being parallel to the columns. Therefore we propose the tentative model of the low-temperature phase shown in Figure 3.8.

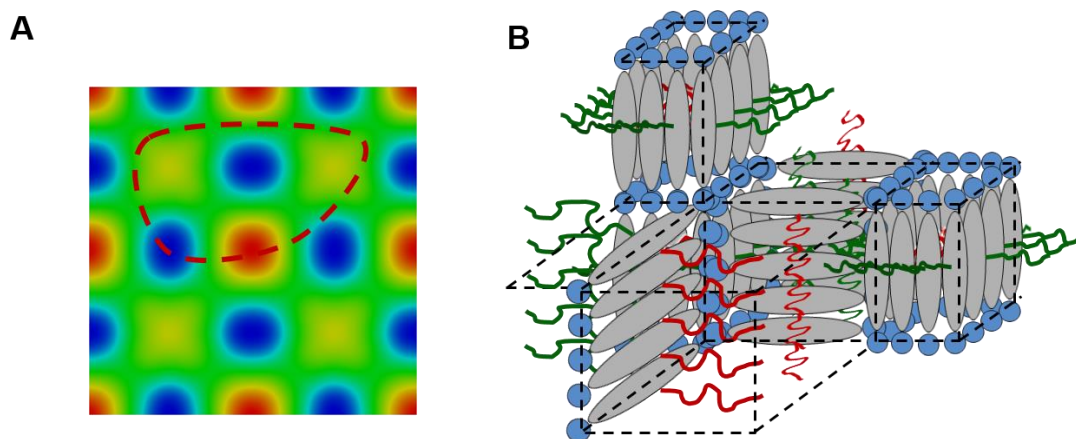


Figure 3.8 Model of the low-temperature phase. A: top view. B: perspective view of circled area in A.

3.3 Conclusion

The X-shaped polyphile **1**, which consists of a rigid rod-like aromatic core with a carbosilane and a semiperfluorinated alkyl chain attached laterally to opposite sides of the aromatic moiety, forms three different liquid crystalline phases when cooling from 130 to 86 °C. The structures of these phases are determined by SAXS. At high temperature, the compound forms a 2D square lattice ($Col_{sq}/p4mm$ phase). It has a chessboard-like honeycomb structure in which the aromatic rods build the net and the carbosilane and semiperfluorinated chains fill up the cells. A reconstructed electron density map and relevant simulations are carried out to confirm this structure. On cooling, the flexible carbosilane chains shrink into a smaller volume. With the decreasing volume of one moiety, the chessboard-like structure is broken. To meet this change, the carbosilane columns distort and even break down into rows of periodic discrete “blobs”. Thus the molecule forms a 3D $I4/mmm$ phase at an intermediate temperature. For lower temperatures, a 3D $P4/mmm$ phase is formed. According to the polarized optical micrographs, the orientation of some aromatic rods in the cylinder walls

change from horizontal to vertical. In the electron density map, it results in the different radii of the two carbosilane columns as well as the continuous of the columns. In future work, we will try to make models for the three phases and have a better understanding of the packing of the molecules in the structures.

Reference

1. Glettner, B.; Liu, F.; Zeng, X.; Prehm, M.; Baumeister, U.; Walker, M.; Bates, M. A.; Boesecke, P.; Ungar, G.; Tschierske, C., Liquid-Crystalline Kagome. *Angewandte Chemie-International Edition* 2008, **47**, 9063-9066.
2. Bucknall, D.; Anderson, H., Polymers get organized. *Science* 2003, **302**, 1904-1905.
3. Park, C.; Yoon, J.; Thomas, E. L., Enabling nanotechnology with self assembled block copolymer patterns. *Polymer* 2003, **44**, 6725-6760.
4. Klok, H.-A.; Lecommandoux, S., Solid-state structure, organization and properties of peptide - Synthetic hybrid block copolymers. *Peptide Hybrid Polymers* 2006, **202**, 75-111.
5. Abetz, V.; Simon, P. F. W., Phase behaviour and morphologies of block copolymers. *Block Copolymers I* 2005, **189**, 125-212.
6. Forster, S.; Antonietti, M., Amphiphilic block copolymers in structure-controlled nanomaterial hybrids. *Advanced Materials* 1998, **10**, 195-217.
7. Widawski, G.; Rawiso, M.; Francois, B., Self-organized honeycomb morphology of star-polymer polystyrene films. *Nature* 1994, **369**, 387-389.
8. Jenekhe, S. A.; Chen, X. L., Self-assembly of ordered microporous materials from rod-coil block copolymers. *Science* 1999, **283**, 372-375.
9. de Boer, B.; Stalmach, U.; Nijland, H.; Hadziioannou, G., Microporous honeycomb-structured films of semiconducting block copolymers and their use as patterned templates. *Advanced Materials* 2000, **12**, 1581-1583.
10. Leclere, P.; Hennebicq, E.; Calderone, A.; Brocorens, P.; Grimsdale, A. C.; Mullen, K.; Bredas, J. L.; Lazzaroni, R., Supramolecular organization in block copolymers containing a conjugated segment: a joint AFM/molecular modeling study. *Progress in Polymer Science* 2003, **28**, 55-81.
11. Ikkala, O.; ten Brinke, G., Functional materials based on self-assembly of polymeric supramolecules. *Science* 2002, **295**, 2407-2409.
12. Walther, M.; Finkelmann, H., Structure formation of liquid crystalline block copolymers. *Progress in Polymer Science* 1996, **21**, 951-979.
13. Poser, S.; Fischer, H.; Arnold, M., LC side group block and graft copolymers - Synthesis and structure/property relationships. *Progress in Polymer Science* 1998, **23**, 1337-1379.
14. Lee, M.; Cho, B. K.; Zin, W. C., Supramolecular structures from rod-coil block copolymers. *Chemical Reviews* 2001, **101**, 3869-3892.

15. *Handbook of Liquid Crystals*. Wiley-VCH: 1998.
16. Stupp, S. I.; LeBonheur, V.; Walker, K.; Li, L. S.; Huggins, K. E.; Keser, M.; Amstutz, A., Supramolecular materials: Self-organized nanostructures. *Science* 1997, **276**, 384-389.
17. Mao, G. P.; Wang, J. G.; Clingman, S. R.; Ober, C. K.; Chen, J. T.; Thomas, E. L., Molecular design, synthesis, and characterization of liquid crystal coil diblock copolymers with azobenzene side groups. *Macromolecules* 1997, **30**, 2556-2567.
18. Hamley, I. W.; Castelletto, V.; Lu, Z. B.; Imrie, C. T.; Itoh, T.; Al-Hussein, M., Interplay between smectic ordering and microphase separation in a series of side-group liquid-crystal block copolymers. *Macromolecules* 2004, **37**, 4798-4807.
19. Anthamatten, M.; Zheng, W. Y.; Hammond, P. T., A morphological study of well-defined smectic side-chain LC block copolymers. *Macromolecules* 1999, **32**, 4838-4848.
20. Tenneti, K. K.; Chen, X. F.; Li, C. Y.; Tu, Y. F.; Wan, X. H.; Zhou, Q. F.; Sics, I.; Hsiao, B. S., Perforated layer structures in liquid crystalline rod-coil block copolymers. *Journal of the American Chemical Society* 2005, **127**, 15481-15490.
21. Tian, Y. Q.; Watanabe, K.; Kong, X. X.; Abe, J.; Iyoda, T., Synthesis, nanostructures, and functionality of amphiphilic liquid crystalline block copolymers with azobenzene moieties. *Macromolecules* 2002, **35**, 3739-3747.
22. Yu, H. F.; Okano, K.; Shishido, A.; Ikeda, T.; Kamata, K.; Komura, M.; Iyoda, T., Enhancement of surface-relief gratings recorded on amphiphilic liquid-crystalline diblock copolymer by nanoscale phase separation. *Advanced Materials* 2005, **17**, 2184-2188.
23. Saishoji, A.; Sato, D.; Shishido, A.; Ikeda, T., Formation of Bragg gratings with large angular multiplicity by means of the photoinduced reorientation of azobenzene copolymers. *Langmuir* 2007, **23**, 320-326.
24. Wang, D.; Ye, G.; Zhu, Y.; Wang, X., Photoinduced Mass-Migration Behavior of Two Amphiphilic Side-Chain Azo Diblock Copolymers with Different Length Flexible Spacers. *Macromolecules* 2009, **42**, 2651-2657.
25. He, X. H.; Huang, L.; Liang, H. J.; Pan, C. Y., Self-assembly of star block copolymers by dynamic density functional theory. *Journal of Chemical Physics* 2002, **116**, 10508-10513.
26. He, X. H.; Huang, L.; Liang, H. J.; Pan, C. Y., Localizations of junction points of ABC 3-miktoarm star terpolymers. *Journal of Chemical Physics* 2003, **118**, 9861-9863.
27. Lu, T.; He, X. H.; Liang, H. J., Ordered microstructures by assembly of ABC 3-miktoarm star terpolymers and linear homopolymers. *Journal of Chemical Physics* 2004, **121**, 9702-9707.
28. Ungar, G.; Tschierske, C.; Abetz, V.; Holyst, R.; Bates, M. A.; Liu, F.; Prehm, M.; Kieffer, R.; Zeng, X.; Walker, M.; Glettner, B.; Zywockinski, A., Self-Assembly at Different Length Scales: Polyphilic Star-Branched Liquid Crystals and Miktoarm Star Copolymers. *Advanced Functional Materials* 2011, **21**, 1296-1323.
29. Tournilhac, F.; Bosio, L.; Nicoud, J. F.; Simon, J., Polyphilic molecules - synthesis and mesomorphic properties of a 4 block molecule. *Chemical Physics Letters* 1988, **145**, 452-454.
30. Pensec, S.; Tournilhac, F. G.; Bassoul, P.; Durliat, C., Synthesis and structural studies of

polyphilic mesogens with central or terminal perfluoroalkyl chains. *Journal of Physical Chemistry B* 1998, **102**, 52-60.

31. Tschierske, C., Liquid crystal engineering - new complex mesophase structures and their relations to polymer morphologies, nanoscale patterning and crystal engineering. *Chemical Society Reviews* 2007, **36**, 1930-1970.

32. Ward, M. D.; Horner, M. J., Structure and order in soft matter: symmetry transcending length scale. *Crystengcomm* 2004, **6**, 401-407.

Chapter 4

Liquid Crystalline Structures Formed by X-shaped Polyphiles with Semiperfluorinated and Hydrocarbon Lateral Chains

4.1 Introduction

Liquid crystalline (LC) compounds with well-defined topological morphologies, such as X-shape, T-shape or other star-branched shapes, can self-assemble into numerous novel 2D and 3D ordered structures¹. X-shaped polyphiles, which usually consist of a rigid aromatic rod and two flexible lateral chains have been reported to form a series of interesting honeycomb-like liquid crystal phases and 3D ordered mesophases^{2, 3}. Compared with T-shaped molecules, X-shaped compounds have two unequal side groups, which offer the possibility of forming more complex liquid crystalline structures.

In Chapter 3, we explored the liquid crystalline phase behavior of an X-shaped polyphile which contains a semiperfluorinated alkyl side chain and a carbosilane side chain. Chessboard-like honeycombs and 3D columnar phases are observed. When changing the carbosilane side chain into a more flexible hydrocarbon alkyl chain, more novel LC structures can be expected. One example is the two-colored LC Kagome which has high density hexagons containing the semiperfluorinated chains and low density triangles containing the nonfluorinated alkyl chains². Based on such results, an X-shaped polyphile with semiperfluorinated and hydrocarbon side chains are designed and examined.

4.2 Results and Discussion

Compound **2** is made up of an oligo(phenyleneethynylene)-based rigid rod with a glycerol group in each end, a hydrocarbon alkyl lateral chain and a semiperfluorinated lateral chain. The molecular structure is shown in Figure 4.1.

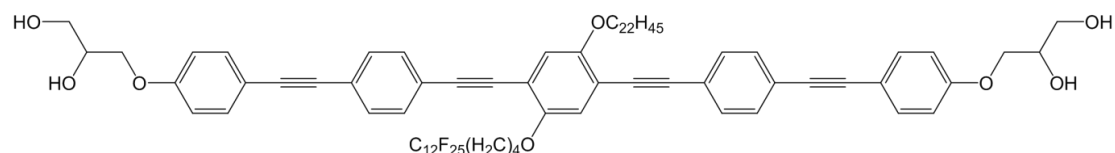


Figure 4.1 Molecular structure of compound **2**

Powder small angle X-ray scattering (SAXS) results show that this compound forms five different phases on cooling from 180 to 100 °C (Figure 4.2). The first two phases are both square $p4mm$ phase, but with different lattice parameters. Then a slight lattice distortion takes place, which resulting in a rectangular $p2mm$ phase. After that, a 3D tetragonal $P4/mmm$ phase is observed. At still lower temperature, the $p2mm$ phase is re-formed.

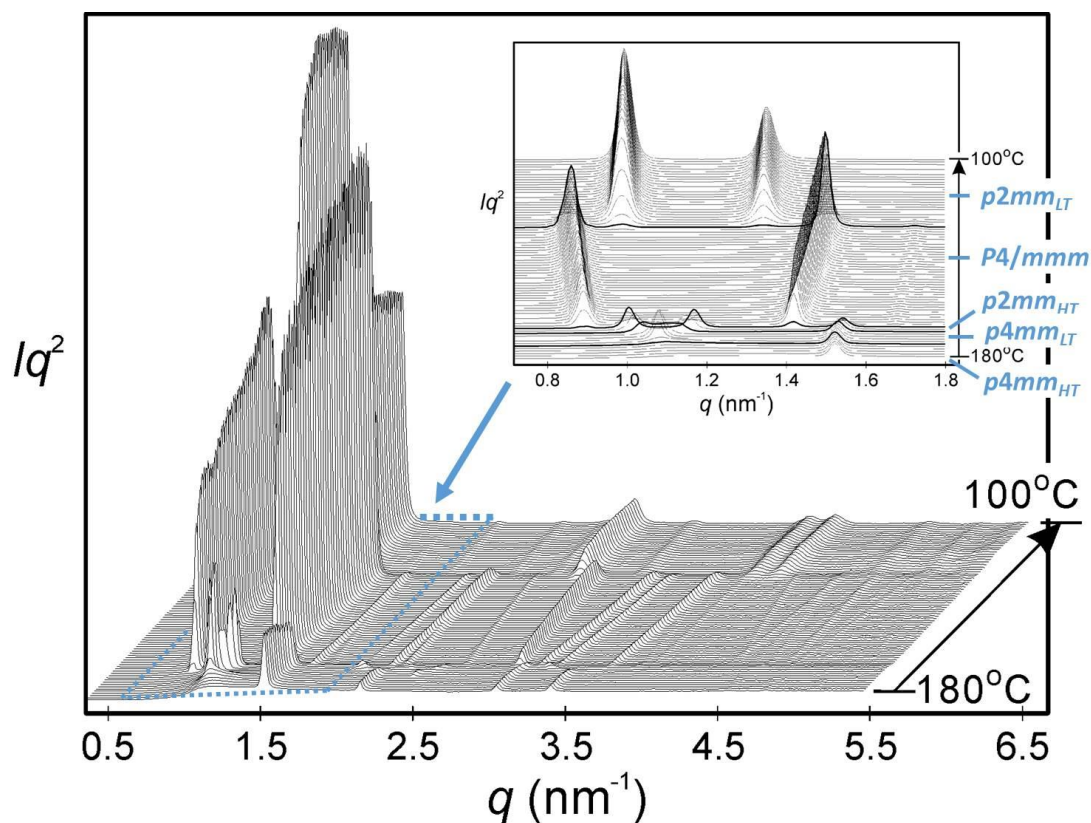


Figure 4.2 Continuous cooling run of compound **2** from 180 °C to 100 °C (back to front), SAXS

diffractograms were recorded every 1 °C; the horizontal axis is scattering factor q ; the vertical axis is Lorentz-corrected intensity; the inset is a zoomed-in version of the diffractograms when q is between 0.7 nm^{-1} and 1.8 nm^{-1} .

4.2.1 One-colored $p4mm$ Phase

The high-temperature $p4mm$ phase ($p4mm_{HT}$) occurs between 180 and 175 °C. The diffraction pattern of compound **2** at 180 °C is shown in Figure 4.3A.

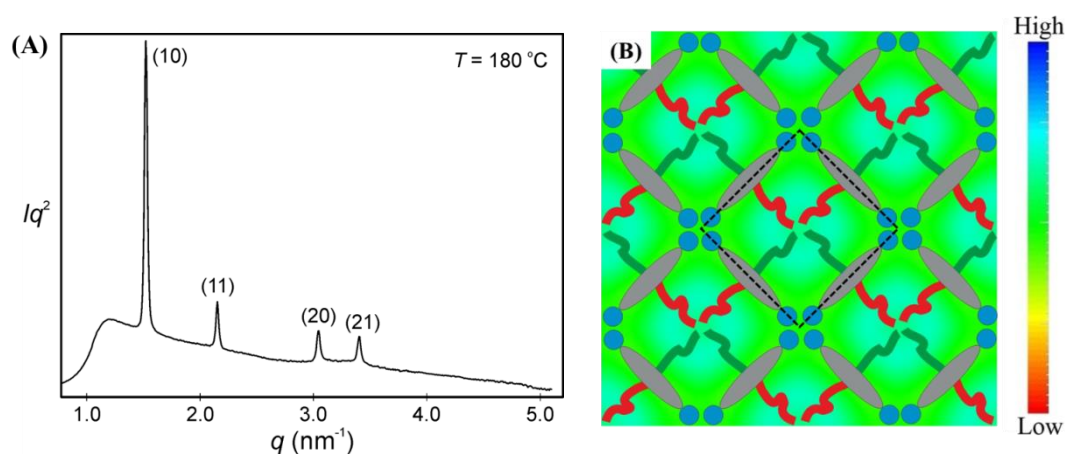


Figure 4.3 (A) Small-angle powder diffractogram of the $p4mm_{HT}$ phase of compound **2** recorded at 180 °C; (B) Reconstructed electron density map of the $p4mm_{HT}$ phase; in the molecule model, the green moiety stands for the alkyl chain and the red stands for the semiperfluorinated chain.

The SAXS results suggest that at high temperature the molecule forms a 2D square lattice (plane group $p4mm$) with the lattice parameter $a = 4.13 \text{ nm}$. The experimental and calculated d -spacings of the SAXS reflections are listed in Table 4.1. The electron density map is also reconstructed using the intensity and the phase angle of each peak (Figure 4.3B). This map shows a square honeycomb in which all the cells are the same and have a slightly higher electron density than the green “walls”. Considering that the lattice parameter is very close to the length of the rigid aromatic rod, we assume that the molecules lie along the edges of the unit cells with the alkyl chains and the semiperfluorinated chains mixing and filling the honeycomb cells.

Table 4.1 Experimental and calculated d -spacings of the observed SAXS reflections of the square phase in compound **2** at 180 °C. All intensities values are Lorentz and multiplicity corrected.

(hk)	$d_{\text{obs.}}$ -spacing (nm)	$d_{\text{cal.}}$ -spacing (nm)	<i>intensity</i>	<i>phase</i>
(10)	4.13	4.13	100.0	0
(11)	2.92	2.92	14.9	0
(20)	2.06	2.06	12.3	π
(21)	1.85	1.85	5.4	π
$a_{\text{squ}} = 4.13 \text{ nm}$				

4.2.2 Two-colored $p4mm$ Phase

The low-temperature $p4mm$ phase ($p4mm_{LT}$) occurs between 175 and 171 °C. The diffraction pattern of compound **2** at 171 °C is shown in Figure 4.4A.

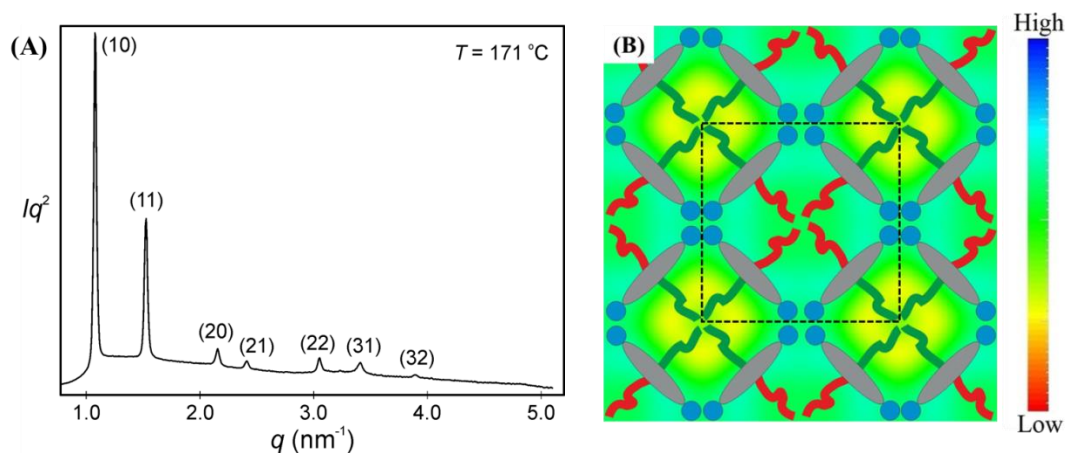


Figure 4.4 (A) Small-angle powder diffractogram of the $p4mm_{LT}$ phase of compound **2** recorded at 171 °C; (B) Reconstructed electron density map of the $p4mm_{LT}$ phase; in the molecule model, the green moiety stands for the alkyl chain and the red stands for the semiperfluorinated chain.

According to the SAXS results, the reflections can be indexed on a square lattice, also with plane group $p4mm$. Compared with the $p4mm_{HT}$ phase, the lattice parameter a increases to 5.83 nm, which is about $\sqrt{2}$ times of the molecular length. The reconstructed electron density map also shows a square honeycomb. However, this time two kinds of honeycomb cells with different colors are gained. Half of the cells

have a slightly higher electron density than the walls, while the rest is slightly lower. This suggests that the alkyl chains and semiperfluorinated chains may be partially separated (in our color scale, pure alkyl and semiperfluorinated chains would perform red and sky-blue, respectively). In this case, the aromatic moieties retain the same honeycomb net as in the $p4mm_{HT}$ phase, while the cells are filled with F-rich and F-poor lateral chains alternatively. As a result, a chess-board like square honeycomb is formed.

Table 4.2 Experimental and calculated d -spacings of the observed SAXS reflections of the square phase in compound **2** at 171 °C. All intensities values are Lorentz and multiplicity corrected.

(hk)	$d_{\text{obs.}}$ –spacing (nm)	$d_{\text{cal.}}$ –spacing (nm)	<i>intensity</i>	<i>phase</i>
(10)	5.83	5.83	100.0	0
(11)	4.12	4.12	53.3	π
(20)	2.91	2.91	8.15	π
(21)	2.61	2.61	1.72	π
(22)	2.06	2.06	5.64	0
(31)	1.84	1.84	3.76	0
(32)	1.61	1.62	0.77	π
$a_{\text{squ}} = 5.83 \text{ nm}$				

4.2.3 Rectangular $p2mm$ Phase

The high-temperature $p2mm$ phase ($p2mm_{HT}$) only occurs in 3 degrees, from 171 to 168 °C. The diffraction pattern of compound **2** at 168 °C is shown in Figure 4.5A.

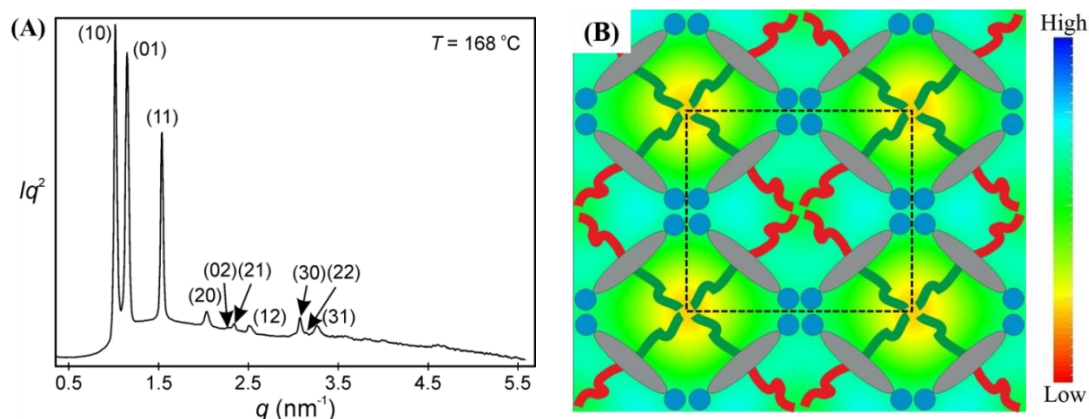


Figure 4.5 (A) Small-angle powder diffractogram of the $p2mm_{HT}$ phase of compound **2** recorded at 168 °C; (B) Reconstructed electron density map of the $p2mm_{HT}$ phase; in the molecule model, the green moiety stands for the alkyl chain and the red stands for the semiperfluorinated chain.

The continuous cooling run of the SAXS experiment shows that the diffraction peaks (10), (20) and (21) of the $p4mm_{LT}$ phase split into two peaks, respectively in the temperature range between 169 and 167 °C. This suggests that a lattice distortion happens and a new phase is formed. By indexing these peaks, a 2D rectangular $p2mm$ phase is obtained. The unit cell parameters are 6.16 nm and 5.47 nm (Table 4.3).

Table 4.3 Experimental and calculated d -spacings of the observed SAXS reflections of the rectangular phase $Col_{rec}/p2mm$ in compound **2** at 168 °C. All intensities values are Lorentz and multiplicity corrected.

(hk)	$d_{obs.}$ -spacing (nm)	$d_{cal.}$ -spacing (nm)	<i>intensity</i>	<i>phase</i>
(10)	6.16	6.16	93.7	0
(01)	5.47	5.47	100.0	0
(11)	4.09	4.09	25.8	π
(20)	3.09	3.08	6.7	π
(02)	2.75	2.73	0.8	π
(21)	2.69	2.68	1.0	π
(12)	2.50	2.50	1.7	π
(30)	2.05	2.05	1.6	/

(22)	2.04	2.04	3.2	/
(31)	1.93	1.92	3.2	/
$a = 6.16 \text{ nm}, b = 5.47 \text{ nm}$				

The reconstructed electron density map of the $p2mm_{HT}$ phase has a similar color with that in the $p4mm_{LT}$ phase, which is also made up with a green aromatic net and two-colored F-rich and F-poor cells (Figure 4.5B). However, with the temperature decreasing, the volumes of the flexible lateral chains would reduce. In this case, they can't fill the square cells any more. Consequently, the squares contract into rhombs in order to satisfy the shrink of the chains. A rhombic honeycomb is therefore formed.

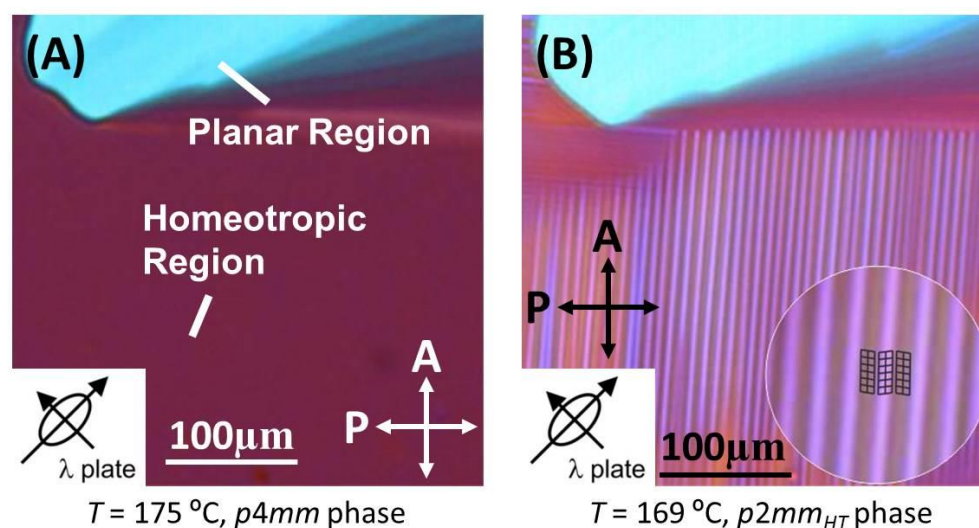


Figure 4.6 Texture of the $p4mm$ (A) and the $p2mm_{HT}$ (B) phase between crossed polarizers (with λ retarder plate); the homeotropically aligned region becomes weakly birefringent on cooling from the $p4mm$ to the $p2mm$ phase; the formation of stripes is explained in the inset.

The polarized optical microscopy experiment offers a more straightforward way to observe and understand the $p2mm_{HT}$ phase. The homeotropic region of the $p4mm$ phase is always dark under a polarized optical microscope, which results in red with the addition of a λ retarder plate (Figure 4.6A). When cooling from the uniaxial $p4mm$ phase to the biaxial $p2mm$ phase, weakly birefringent stripes turned up in this region (Figure 4.6B). The different colors of the stripes represent the different orientations of

the molecules within the stripes. When the squares distort into rhombs, the molecules can choose to tilt towards both sides. Thus molecules with different orientations are generated. The model of the arrangement of the molecules is shown in the magnified circle in Figure 4.6B.

4.2.4 Wigwam-like 3D $P4/mmm$ Phase

The $P4/mmm$ phase appears below the $p2mm_{HT}$ phase, from 168 to 125 °C. The diffraction pattern of compound **2** at 160 °C is shown in Figure 4.7A.

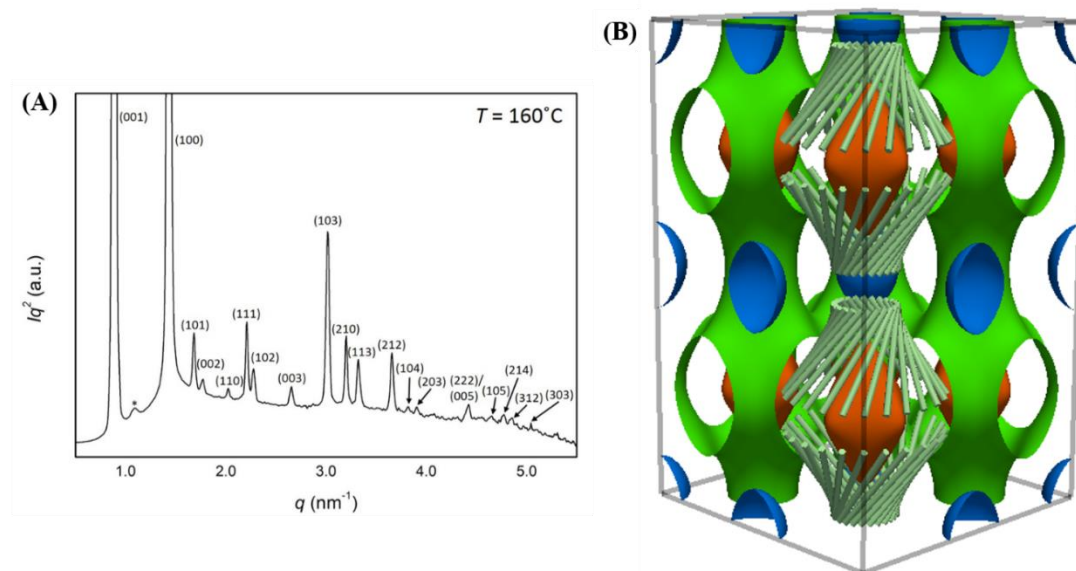


Figure 4.7 (A) Small-angle powder diffractogram of the $P4/mmm$ phase of compound **2** recorded at 160 °C; (B) Reconstructed electron density map of the $P4/mmm$ phase; the middle-density green moiety (aromatic rods) forms a cage-like “double wigwam” structure with the low-density red moiety (alkyls) inside and the high-density blue moiety (fluorocarbon chains) outside the cage; model of the aromatic rods are added in two of the “wigwams”.

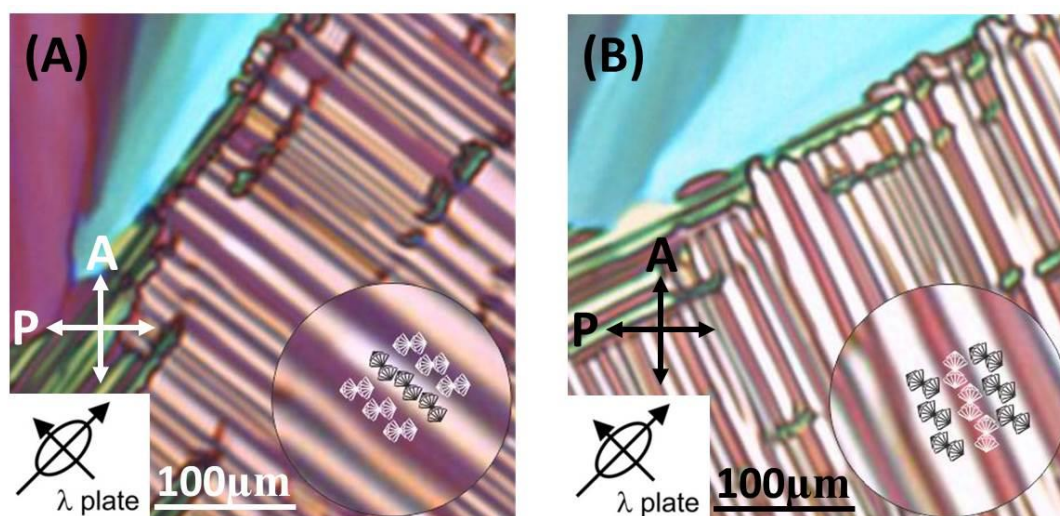
The diffraction pattern at 160 °C can be indexed on a 3D tetragonal phase, with lattice parameter $a = 4.40$ nm and $c = 7.09$ nm. There is a very small peak which cannot be indexed. According to its d -spacing, this might be the still existing (01) peak of the $p2mm_{HT}$ phase. We believe it can be ignored since it disappears at lower temperature

as we predicted. Considering that the (hkl) of the peaks cannot satisfy any reflection conditions in a tetragonal lattice, the possible space group with highest symmetry is $P4/mmm$. The reconstructed electron density map is carried out using the intensity and phase angle of the six strongest peaks. It shows that the middle-density green moiety (aromatic rods) forms a cage-like “double wigwam” structure with the low-density red moiety (alkyls) inside and the high-density blue moiety (semiperfluorinated chains) outside the cage (Figure 4.7B). This interesting structure is the first example of a 3D liquid crystal honeycomb.

Table 4.4 Experimental and calculated d -spacings of the observed SAXS reflections of the rectangular phase $P4/mmm$ in compound **2** at 160 °C. All intensities values are Lorentz and multiplicity corrected.

(hkl)	$d_{\text{obs.}}$ -spacing (nm)	$d_{\text{cal.}}$ -spacing (nm)	<i>intensity</i>	<i>phase</i>
(001)	7.08	7.09	77.7	0
cannot be indexed	5.76	/	/	/
(100)	4.39	4.40	100	0
(101)	3.74	3.74	1.74	0
(002)	3.55	3.55	0.461	/
(110)	3.11	3.11	0.268	/
(111)	2.85	2.85	2.29	π
(102)	2.77	2.76	0.885	/
(003)	2.37	2.36	0.781	/
(103)	2.08	2.08	7.31	/
(210)	1.96	1.97	2.06	/
(113)	1.89	1.88	1.61	/
(212)	1.72	1.72	2.14	/
(104)	1.64	1.64	0.164	/
(203)	1.61	1.61	0.226	/
(222)/(005)	1.42	1.42/1.42	0.719	/

(105)	1.35	1.35	0.317	/
(214)	1.32	1.32	0.358	/
(312)	1.29	1.30	0.438	/
(303)	1.25	1.25	0.0779	/
(006)	1.18	1.18	0.0619	/
$a = 4.40 \text{ nm}, c = 7.09 \text{ nm}$				



$T = 150 \text{ }^\circ\text{C}, P4/mmm \text{ phase}$

Figure 4.8 Texture of the $P4/mmm$ phase between crossed polarizers (with λ retarder plate); A and B are the texture with different rotation angles; the arrangement of the molecules in the stripes are shown in the inset.

Under a polarized optical microscope, broader stripes are observed when cooling from the $p2mm_{HT}$ phase to the $P4/mmm$ phase. In two neighbour stripes, molecules have different orientations. With the help of the λ retarder plate, we can know that when the stripe is red, the molecules are parallel or perpendicular to the analyser (the view screen). When the stripe is blueish, the slow axis of the sample, which is also the direction of the aromatic rods, is in the northeast-southwest direction. Otherwise, when the stripe is yellowish, the molecules lie along the northwest-southeast direction. As the birefringence depends to the angle between the polarizer and the optical axis of the sample, the color of the stripes would change along with the rotation of the

sample. In this way, we can determine the direction of the molecules within each stripe. The angle between the molecules in neighbour stripes that we measured based on the textures is 64 degrees, while the angle we calculated from the lattice parameter is 63 degree. They match very well. The model of the molecules is shown in the magnified circle in Figure 4.8.

4.2.5 Re-entrant $p2mm$ Phase

The $p2mm$ phase occurs again after the $P4/mmm$ phase, from 125 to 100 °C. The diffraction pattern of compound **2** at 100 °C is shown in Figure 4.9A.

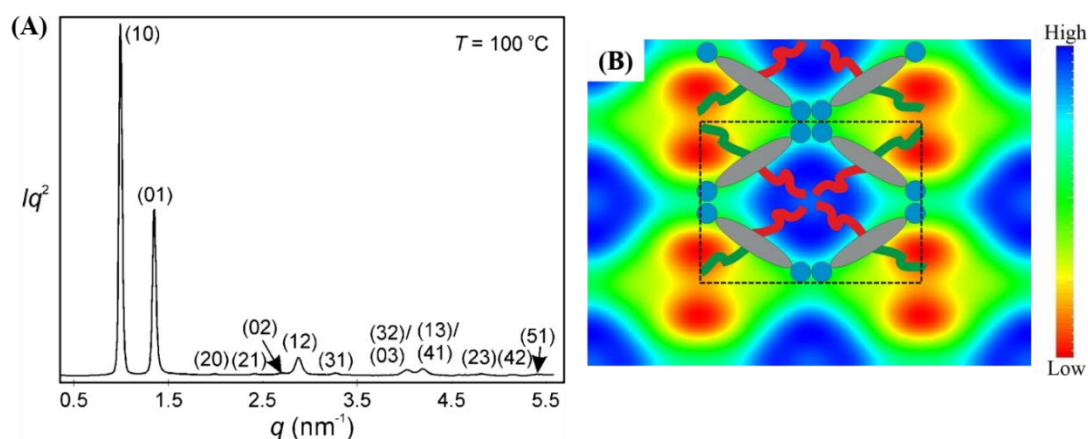


Figure 4.9 (A) Small-angle powder diffractogram of the $p2mm_{LT}$ phase of compound **2** recorded at 100 °C; (B) Reconstructed electron density map of the $p2mm_{LT}$ phase; in the molecule model, the green moiety stands for the alkyl chain and the red stands for the semiperfluorinated chain.

According to the peak indexing, the liquid crystalline phase at lower temperature is again 2D rectangular $p2mm$ (Table 4.5). The unit cell parameter $a = 6.33$ nm and $b = 4.65$ nm. Compare with the $p2mm_{HT}$ phase, the $p2mm_{LT}$ phase has an obviously more contracted structure. The reconstructed electron density map shows that complete alkyl-fluoroalkyl micro-phase separation takes place in this phase. Pure alkyl chains fill the low-density red cells, pure semiperfluorinated chains fill the high-density blue cells and the rigid aromatic rods build middle-density green walls among the cells. This remarkable re-entrance might be caused by the shrinking side chains which can

no longer fill the space of the “cage” in the Wigwam phase. Consequently, the $p2mm$ phase is formed again.

Table 4.5 Experimental and calculated d -spacings of the observed SAXS reflections of the rectangular phase $Col_{rec}/p2mm$ in compound **2** at 100 °C. All intensities values are Lorentz and multiplicity corrected.

(hk)	$d_{obs.}$ –spacing (nm)	$d_{cal.}$ –spacing (nm)	<i>intensity</i>	<i>phase</i>
(10)	6.33	6.33	100.0	0
(01)	4.65	4.65	51.1	0
(20)	3.16	3.16	0.3	π
(21)	2.60	2.61	0.2	π
(02)	2.33	2.33	0.4	0
(12)	2.18	2.18	4.3	π
(31)	1.92	1.92	0.4	π
(32)	1.56	1.56	2.3	/
(03)		1.55	1.2	/
(13)	1.50	1.51	1.1	/
(41)		1.50	1.1	/
(23)	1.38	1.39	0.1	/
(42)	1.31	1.31	0.6	/
(51)	1.22	1.22	0.4	/
$a = 6.33$ nm, $b = 4.65$ nm				

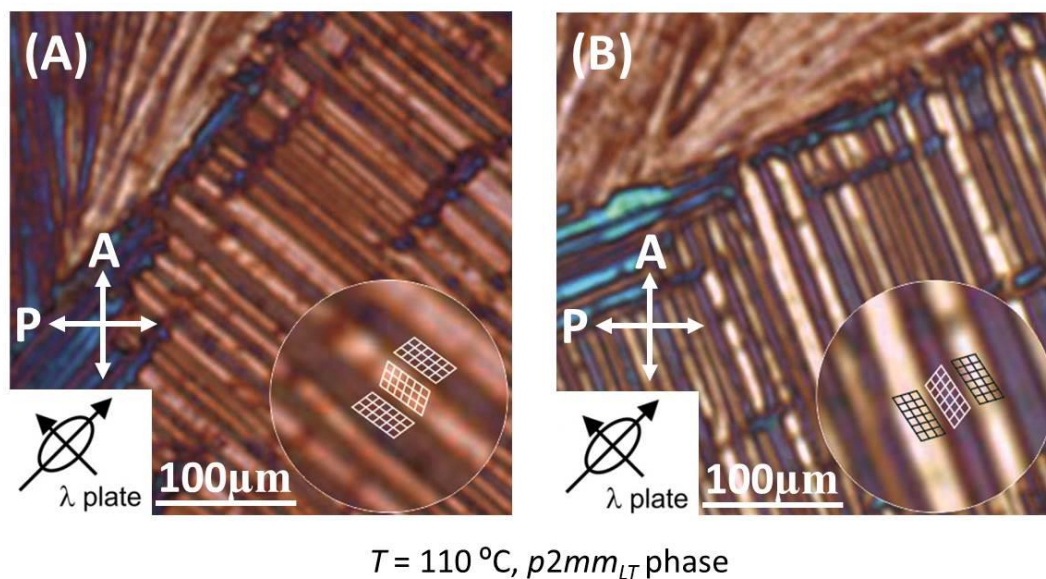


Figure 4.10 Texture of the $p2mm_{LT}$ phase between crossed polarizers (with λ retarder plate). A and B are the texture with different rotation angles; the arrangement of the molecules in the stripes are shown in the inset.

The texture becomes weakly birefringent when changing from the $P4/mmm$ phase to the $p2mm_{LT}$ phase. The orientation of the molecules can be determined by adding a λ retarder plate and rotating the sample. Since it's also a rhombic honeycomb, the packing of the molecules is similar to that of the $p2mm_{HT}$ phase. The model of the molecules is shown in the magnified circle in Figure 4.10.

4.3 Conclusion

At high temperatures the X-shaped polyphile **2** forms a “single colour” and a “two colour” (chessboard) square honeycombs ($p4mm$). On cooling, the “chessboard” contracts into a rhombic chessboard ($p2mm$). After that, a 2D-3D transition takes place, resulting in a “double-wigwam” cage-like tetragonal phase ($P4/mmm$). At low temperatures the $p2mm$ rectangular honeycomb re-enters, now fully phase-separated. The reappearance of the $p2mm$ is a consequence of the competition between tendencies for de-mixing and space filling. A schematic presenting the package of molecules in the five phases is shown below.

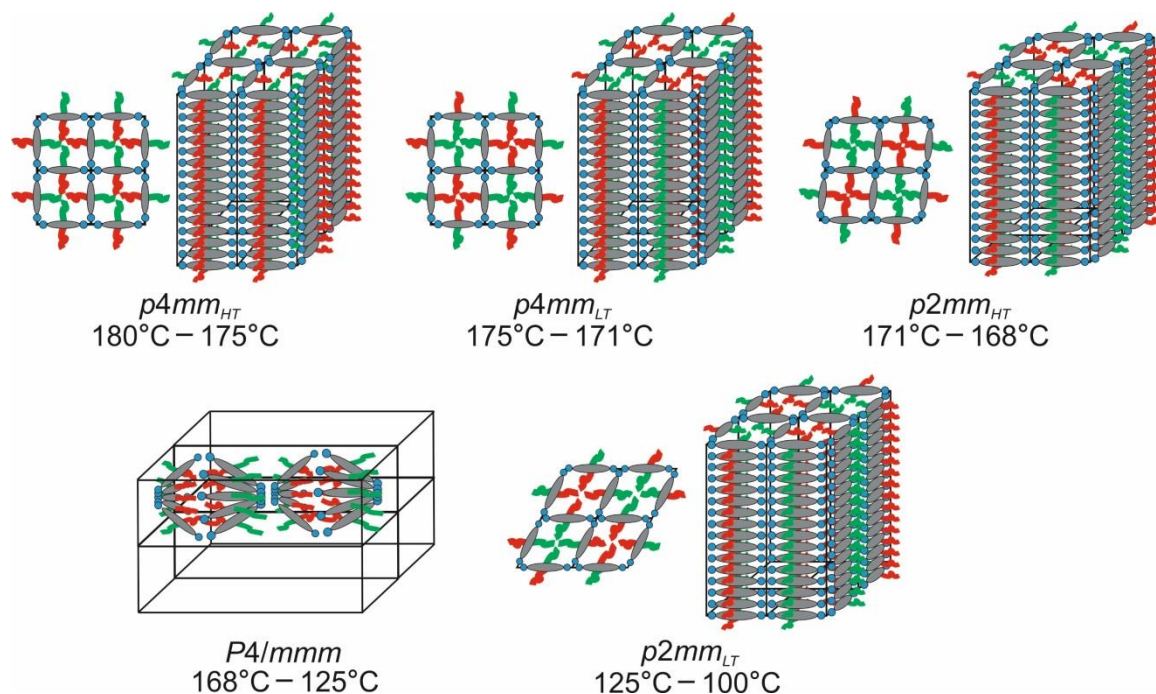


Figure 4.11 Schematic showing the five phases on cooling

Reference

1 G. Ungar, C. Tschierske, V. Abetz, R. Holyst, M. A. Bates, F. Liu, M. Prehm, R. Kieffer, X. B. Zeng, M. Walker, B. Glettner, A. Zywockinski, *Adv. Funct. Mater.* (2011), **21**, 1296.

2 B. Glettner, F. Liu, X. B. Zeng, M. Prehm, U. Baumeister, M. Walker, M. A. Bates, P. Boesecke, G. Ungar, C. Tschierske, *Angew. Chem. Int. Ed.* (2008), **47**, 9063.

[3] B. Chen, U. Baumeister, S. Diele, M.K. Das, X.B. Zeng, G. Ungar, C. Tschierske, *J. Am. Chem. Soc.* (2004), **126**, 8608.

Chapter 5

Spontaneous Mirror Symmetry Breaking in Polycatenar Molecules by CD Spectroscopy

5.1 Introduction

Polycatenar liquid crystals (LC) were first reported in 1985 by Malthete *et al.* [1] These materials have the characteristics of both calamitic and discotic liquid crystals and exhibit numerous complex liquid crystal phases. Polycatenar liquid crystalline molecules usually consist of a long rigid rod-like aromatic central core and a number of flexible side chains in terminal positions. In polycatenars, the highly conjugated aromatic cores of the neighboring molecules are attracted together due to van der Waals forces. This attraction leads to microphase separation and results in the formation of liquid crystal structures. A variety of mesogenic phases can be observed by changing the length or number of the terminal chains. Lamellar phases are usually formed when the volumes of the terminal chains are small. With the increasing size of the chains, the interface between the cores and tails must be curved to meet the requirement of effective spacing filling, which drives the formation of columnar phases, and more important for the current project, the bicontinuous cubic (Cub_{bi}) phases.

The Cub_{bi} phases have cubic symmetry and the 3D space is divided into two kinds of *continuous* subspaces, each of which is occupied by one of the two moieties of the molecules. For polycatenar molecules these would be the rigid aromatic core and the flexible aliphatic end chains, respectively. Such phases have attracted much attention owing to their unique structures. So far, in polycatenar compounds there are two kinds of

confirmed Cub_{bi} phases. One is the double-network double gyroid $Ia\bar{3}d$ phase [2], the other is the triple-network $Im\bar{3}m$ phase [3]. In both phases the rigid aromatic cores self-assemble into columnar segments, which then join together to form 3D periodic networks, and the soft aliphatic chains occupy the space in between. While in the $Ia\bar{3}d$ phase, there are two such networks which are interpenetrating each other but never intersect, in the $Im\bar{3}m$ phase there are three such networks. In the columnar segments of the network, the rigid aromatic cores always lie perpendicular to the direction of the network segments.

More recently the triple network $Im\bar{3}m$ phase has been found always to be chiral, whether it is found in chiral or achiral compounds, in the latter case through dynamic mirror symmetry breaking [4]. The origin of such mirror symmetry breaking is attributed to the twist of molecular orientation along the columnar segment. Due to the fact that molecules share the same orientation at the junction point, in the branched out segments from the same junction joint the molecules must be twisting with the same handedness to avoid clashing. Consequently the same chiral handedness propagates in each network. $Ia\bar{3}d$ phase is achiral because the two networks have opposite handedness and the chirality cancels each other. However, in $Im\bar{3}m$ phase, the chirality of the three networks does not cancel, and its overall chirality is demonstrated by the formation of chiral domains.

In addition to the Cub_{bi} phases, dynamic mirror symmetry breaking phenomena have recently been reported as well in the isotropic liquid formed by achiral polycatenar liquid crystalline compounds [5]. This breaking of symmetry is a consequence of chiral self-sorting, which leads to the formation of conglomerates with uniform chirality. In this chapter, we first summarize the phase sequences of a series of polycatenar compounds on the basis of our studies by SAXS and other methods, followed by the study of the chiral isotropic phase ($\text{iso}^{[*]1}$), as well as the transitions from chiral isotropic $\text{iso}^{[*]1}$ to achiral double network $Ia\bar{3}d$ cubic phase and chiral triple network cubic phase ($Im\bar{3}m$) by

¹ The isotropic phase formed by intrinsically chiral compounds is normally called Iso^* , to differentiate from it we use the abbreviation $\text{Iso}^{[*]}$ for the chiral isotropic phase formed by achiral molecules through dynamic mirror symmetry breaking.

Circular Dichroism Spectroscopy.

5.2 Compounds

A series of polycatenar molecules were designed and synthesized, by Prof. C. Tschierske's group at Martin Luther University, Halle-Wittenburg, to investigate their LC phase behaviors. Figure 5.1 shows the general molecular structure of the polycatenar compounds, in which R_n represents the terminal chains. Small angle X-ray diffraction (SAXS), differential scanning calorimetry (DSC), polarized optical microscopy (POM) and circular dichroism (CD) spectroscopy are used for the investigation. The self-assembled mesophases are summarized and listed in Table 5.1.

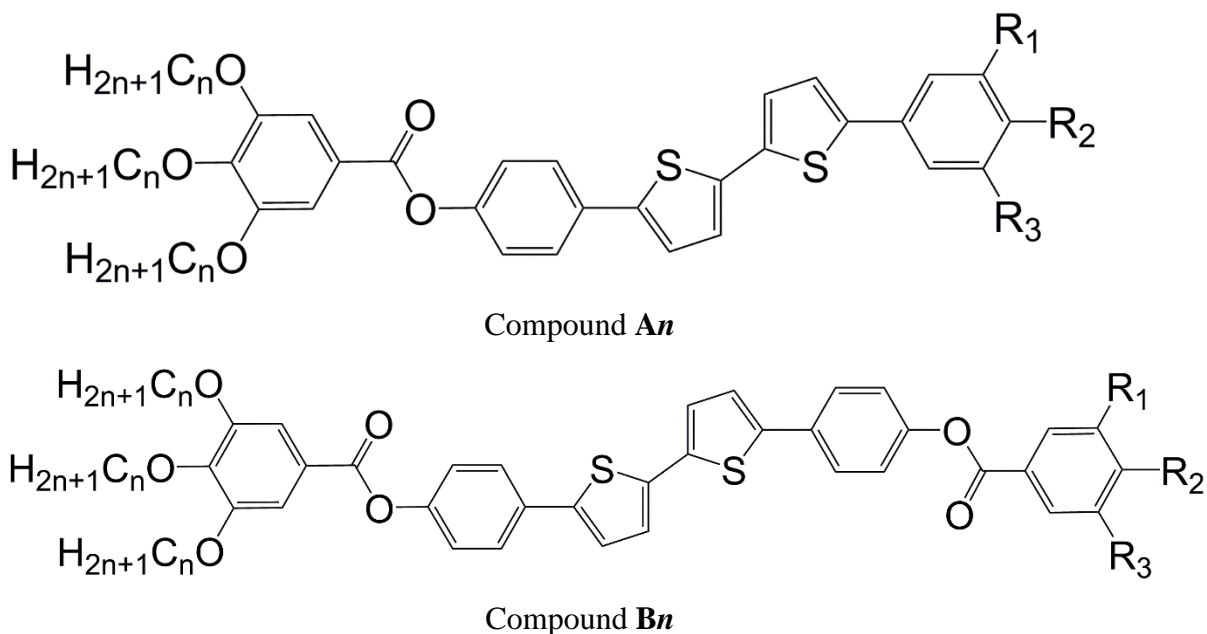


Figure 5.1 General molecular structure of polycatenar compounds.

In this chapter, five compounds (highlighted in bold and shaded in Table 5.1) that show the two Cub_{bi} phases, as well as the chiral isotropic ($\text{Iso}^{[*]}$) phase will be discussed.

Table 5.1 Liquid crystalline phases and other parameters of compounds **An** and **Bn**

Compound	n	R ₁	R ₂	R ₃	Phases
A1	10	H	OC ₄ H ₉	H	Iso → 132 °C → <i>Ia</i> $\bar{3}d$
A2	10	H	OCH ₂ CH(CH ₃)CH ₂ CH ₃	H	Cr → 91 °C → <i>Ia</i> $\bar{3}d$ + <i>Im</i> $\bar{3}m$ → 106 °C → <i>Im</i> $\bar{3}m$ → 131 °C → Iso
A3	10	H	OC ₁₆ H ₃₃	H	Heating: Cr → 87 °C → <i>Im</i> $\bar{3}m$ → 116 °C → Iso Fast cooling: Iso → 109 °C → <i>Im</i> $\bar{3}m$ → 73 °C → Cr Slow cooling: Iso → 109 °C → distorted <i>Ia</i> $\bar{3}d$ → 73 °C → Cr
A4	21	H	O(CH ₂) ₄ C ₆ F ₁₃	H	First heating: Crystal → 82 °C → <i>P2</i> ₁ <i>2</i> ₁ <i>2</i> ₁ → 99 °C → <i>Im</i> $\bar{3}m$ → 113 °C → distorted <i>Ia</i> $\bar{3}d$ → 120 °C → <i>Ia</i> $\bar{3}d$ → 128 °C → Iso Cooling: Iso → 117 °C → Iso ^[*] → 70 °C → Iso _{glass} Second heating: Iso _{glass} → 72 °C → Iso* → 119 °C → Iso
B1	6	H	OC ₆ H ₁₃	H	Fast heating: Crystal → 144 °C → <i>I4</i> ₁ <i>22</i> → 164 °C → <i>I4</i> ₁ <i>22</i> + <i>Ia</i> $\bar{3}d$ → 180 °C → <i>Ia</i> $\bar{3}d$ → 207 °C → Iso ^[*] → 213 °C → Iso Slow heating: Cr → 143 °C → orthorhombic + <i>I4</i> ₁ <i>22</i> → 171 °C → <i>Ia</i> $\bar{3}d$ → 207 °C → Iso ^[*] → 213 °C → Iso Fast cooling: Iso → 211 °C → Iso ^[*] → 180 °C → M phase

					Slow cooling: Iso \rightarrow 211 °C \rightarrow Iso ^[*] \rightarrow 178 °C \rightarrow <i>Ia</i> $\bar{3}d$ \rightarrow 70°C \rightarrow Cr
B2	6	H	OC ₁₂ H ₂₅	H	First heating: Cr \rightarrow 131 °C \rightarrow M phase \rightarrow 186 °C \rightarrow diffused <i>Ia</i> $\bar{3}d$ \rightarrow 194 °C \rightarrow <i>Ia</i> $\bar{3}d$ \rightarrow 197 °C \rightarrow Iso ^[*] \rightarrow 205 °C \rightarrow Iso Cooling: Iso \rightarrow 191 °C \rightarrow Iso ^[*] \rightarrow 176 °C \rightarrow M phase \rightarrow 89 °C \rightarrow Cr
B3	6	H	OC ₁₆ H ₃₃	H	Heating: Cr \rightarrow 128 °C \rightarrow <i>Im</i> $\bar{3}m$ \rightarrow 193 °C \rightarrow Iso Cooling: Iso \rightarrow 182 °C \rightarrow Iso ^[*] \rightarrow 180 °C \rightarrow <i>Im</i> $\bar{3}m$ \rightarrow 88 °C \rightarrow M phase \rightarrow 80 °C \rightarrow Cr
B4	10	F	H	F	Cr \rightarrow 118 °C \rightarrow <i>Im</i> $\bar{3}m$ \rightarrow 172 °C \rightarrow Iso
B5	10	H	H	F	Cr \rightarrow 114 °C \rightarrow <i>Ia</i> $\bar{3}d$ \rightarrow 175 °C \rightarrow Iso
B6	10	H	H	OEt	Cr \rightarrow 100 °C \rightarrow <i>Im</i> $\bar{3}m$ \rightarrow 130 °C \rightarrow Iso
B7	10	Br	H	Br	Cr \rightarrow 118 °C \rightarrow <i>Im</i> $\bar{3}m$ \rightarrow 156 °C \rightarrow Iso
B8	10	H	OCH ₃	H	Heating: Cr \rightarrow 122 °C \rightarrow <i>Ia</i> $\bar{3}d$ \rightarrow 193 °C \rightarrow Iso Cooling: Iso \rightarrow 191 °C \rightarrow Iso* \rightarrow 170 °C \rightarrow <i>I</i> 4 ₁ 22 + <i>Ia</i> $\bar{3}d$ \rightarrow 164 °C \rightarrow <i>Ia</i> $\bar{3}d$
B9	10	H	OC ₆ H ₁₃	H	Heating: Cr \rightarrow 120 °C \rightarrow orthorhombic + <i>Im</i> $\bar{3}m$ \rightarrow 160 °C \rightarrow <i>Im</i> $\bar{3}m$ \rightarrow 188 °C \rightarrow Iso ^[*] \rightarrow 191 °C

					→ Iso Cooling: Iso → 190 °C → Iso ^[*] → 174 °C → <i>Im</i> $\bar{3}m$
B10	10	H	OC ₁₆ H ₃₃	H	Heating: Cr → 114 °C → <i>Im</i> $\bar{3}m$ → 151 °C → <i>Im</i> $\bar{3}m$ + distorted <i>Ia</i> $\bar{3}d$ → 168 °C → <i>Ia</i> $\bar{3}d$ → 175 °C → Iso Cooling: Iso → 170 °C → <i>Ia</i> $\bar{3}d$ → 164 °C → distorted <i>Ia</i> $\bar{3}d$ → 101 °C → distorted <i>Im</i> $\bar{3}m$ → 80 °C → Cr
B11	10	H	OC ₁₈ H ₃₇	H	Heating: Cr → 111 °C → <i>Im</i> $\bar{3}m$ → 136 °C → distorted <i>Ia</i> $\bar{3}d$ → 165 °C → <i>Ia</i> $\bar{3}d$ → 179 °C → Iso Cooling: Iso → 168 °C → <i>Ia</i> $\bar{3}d$ → 160 °C → distorted <i>Ia</i> $\bar{3}d$ → 88 °C → Cr
B12	21	H	H	H	Cr → 114 °C → <i>Ia</i> $\bar{3}d$ → 162 °C → Iso
B13	21	H	CN	H	Heating: Cr → 104 °C → <i>Ia</i> $\bar{3}d$ → 224 °C → Iso Cooling: Iso → 237 °C → diffused <i>Ia</i> $\bar{3}d$ → 224 °C → <i>Ia</i> $\bar{3}d$ → 87 °C → Cr
B14	21	OCH ₃	H	H	Cr → 107 °C → <i>Im</i> $\bar{3}m$ + <i>Ia</i> $\bar{3}d$ → 144 °C → Iso
B15	21	OCH ₃	OCH ₃	OCH ₃	Heating: Cr → 109 °C → <i>Im</i> $\bar{3}m$ → 128 °C → Iso Cooling: Iso → 120 °C → M phase → 118 °C → <i>Im</i> $\bar{3}m$ → 66 °C → Cr

5.3 Results and Discussions

5.3.1 SAXS Results

In this section the SAXS results on the $Ia\bar{3}d$ and $Im\bar{3}m$ cubic phases, and the chiral isotropic (Iso[*]) phase will be presented using sample **A4** as an example.

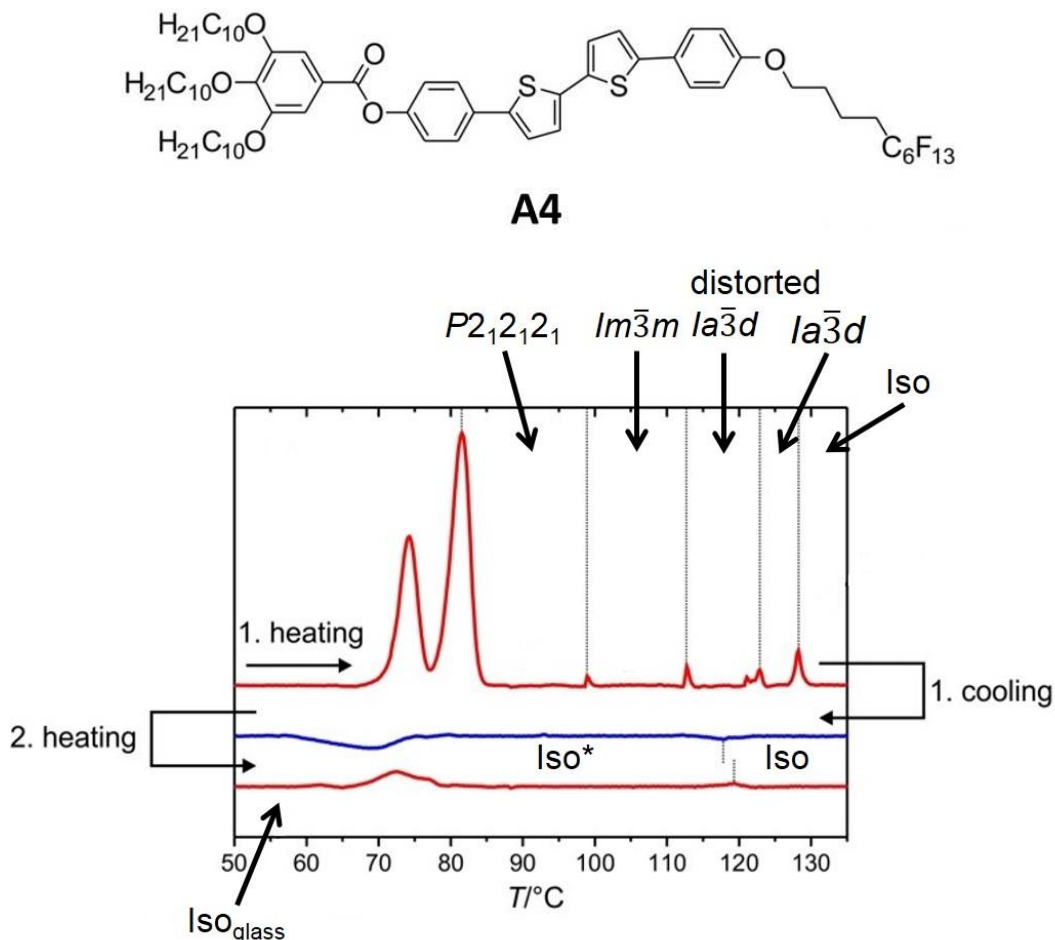


Figure 5.2 General molecular structure and DSC traces of compound **A4**. The heating and cooling rate of DSC is 10 degrees per minute. Four different LC phases are formed on first heating (of solution crystallized sample). While on cooling and second heating, only chiral isotropic phase and glass isotropic phase are formed.

Compound **A4** shows very complex phase transitions on first heating, from crystal to liquid crystal at around 82 °C, then four different LC phases are observed before isotropization at 128 °C. The phase transition temperatures between LC phases are 99, 113 and 123 °C, respectively. On cooling and second heating, only the transition between the normal isotropic phase and the chiral isotropic phase is observed at around 117 °C

(Figure 5.2).

The LC phases are examined by SAXS (Figure 5.3). The fresh powder sample was heated up from 60 to 150 °C. The diffractograms were recorded every 3 degrees. At 81 °C, the crystal peaks disappeared and a broad peak was formed. Between 84 and 90 °C, very complex peaks were observed, which can be indexed on the basis of an orthorhombic lattice with space group $P2_12_12_1$. After that, at 93 °C, the diffused ring appeared again and the $Im\bar{3}m$ phase started to form. From 111 to 114 °C, a distorted $Ia\bar{3}d$ phase is formed. At higher temperature, $Ia\bar{3}d$ phase is observed. Here we will discuss the $Ia\bar{3}d$ and $Im\bar{3}m$ phase. The complex $P2_12_12_1$ and distorted $Ia\bar{3}d$ phase will be studied in chapter 7.

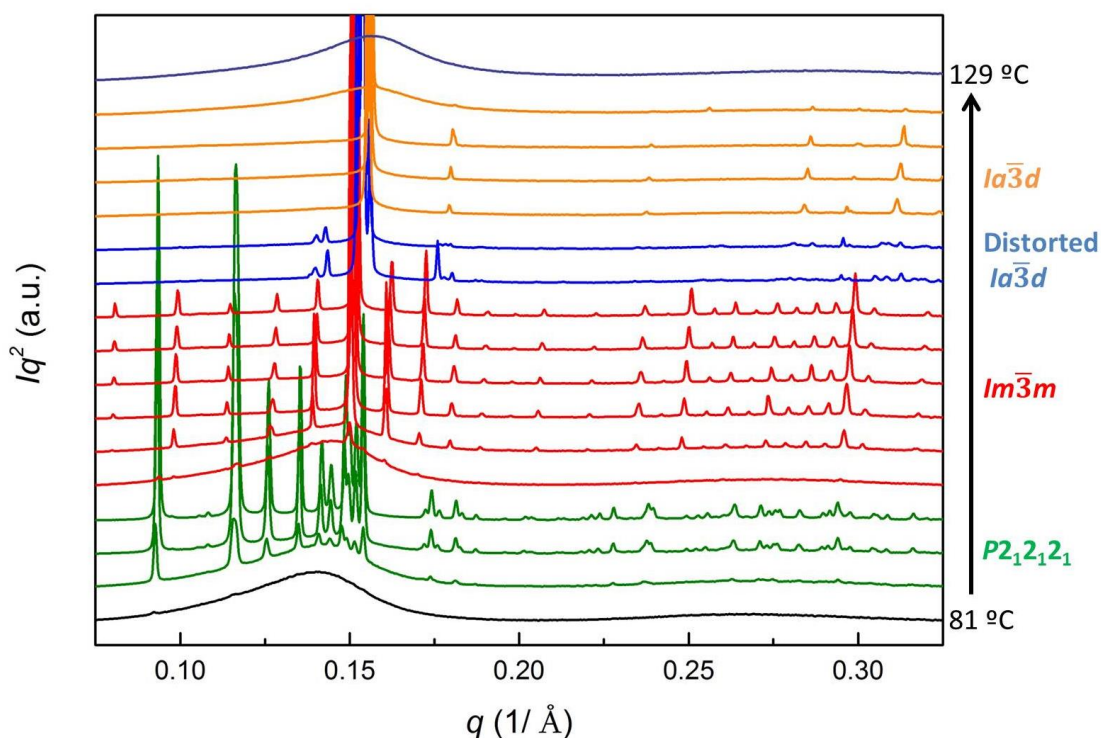


Figure 5.3 First heating run of compound **A4** from 81 to 129 °C, SAXS diffractograms were recorded every 3 °C; the horizontal axis is the magnitude of the scattering wave-vector q , which equals to $4\pi\sin(\theta)/\lambda$ where 2θ is the diffraction angle and λ the X-ray wavelength; the vertical axis is Lorentz-corrected intensity; four different LC phases, $P2_12_12_1$, $Im\bar{3}m$, distorted $Ia\bar{3}d$ and $Ia\bar{3}d$, are observed with increasing temperature.

5.3.1.1 $Ia\bar{3}d$ Phase

The small-angle diffraction pattern of compound **A4** in the $Ia\bar{3}d$ Phase, at 120 °C is shown in Figure 5.4. The relative q positions of the reflections are $\sqrt{6}$, $\sqrt{8}$, $\sqrt{14}$, $\sqrt{16}$, $\sqrt{22}$, $\sqrt{24}$ and $\sqrt{26}$, and they can be indexed as the (211), (220), (321), (420), (332), (422) and (431) reflections of the $Ia\bar{3}d$ cubic phase, with the lattice parameter $a = 98.7\text{Å}$.

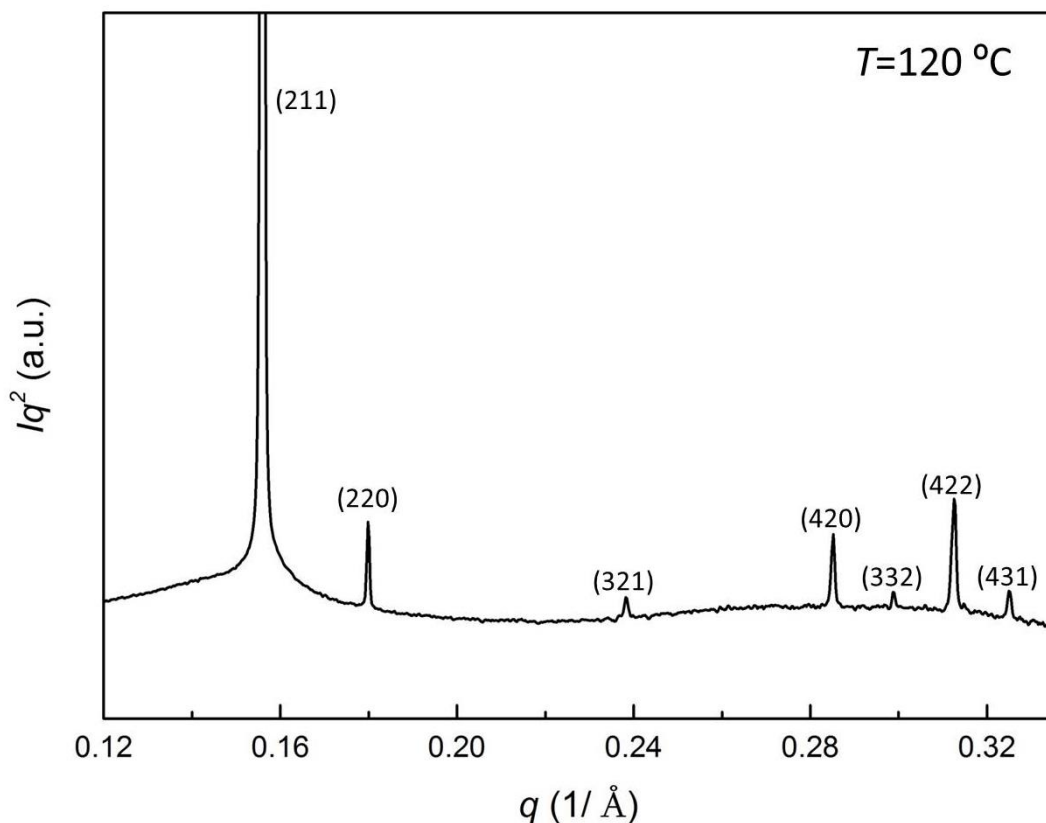


Figure 5.4 Small-angle powder diffractogram of the $Ia\bar{3}d$ phase of compound **A4** recorded at 120 °C. The (211) peak is much stronger than any other peaks (see Table 5.2) and the vertical axis is scaled so that to show the weaker peaks.

Table 5.2 Experimental and calculated d -spacings of the observed SAXS reflections of the $Ia\bar{3}d$ phase in compound **A4** at 120 °C.

(hkl)	$d_{\text{obs.}} - \text{spacing (Å)}$	$d_{\text{cal.}} - \text{spacing (Å)}$	<i>intensity</i>	<i>Phase</i>
(211)	40.3	40.3	100.0	π
(220)	34.9	34.9	1.4	π
(321)	26.4	26.4	0.7	0
(420)	22.0	22.1	1.8	0
(332)	21.0	21.0	0.4	0
(422)	20.1	20.1	2.8	π

(431)	19.3	19.4	0.6	π
$a = 98.7 \text{ \AA}$				

The reconstructed electron density map of the $Ia\bar{3}d$ phase of compound **A4** was obtained using the diffraction intensities and structure factor phase angles (0 or π) listed in Table 5.2 (Figure 5.5A). As shown in the electron density map, the high-density blue isoelectron surfaces enclose the aromatic cores, and the low-density green regions are filled by the end chains (mixture of alkyl and the fluorinated chains). Here the alky chains and the fluorinated chains are not expected to separate as the relative volume of the fluorinated chains is really small, their relative surface area would become too large to reduce the system free energy. The two interpenetrating networks, which are formed by the aromatic cores, are schematically shown in Figure 5.5B. The volume ratio of the high-density aromatic cores and the low-density terminal chains is 0.36: 0.64. The electron density histogram corresponding to the electron density map and the boundary of the high and low electron density regions calculated from the volume ratio are shown in Figure 5.5C.

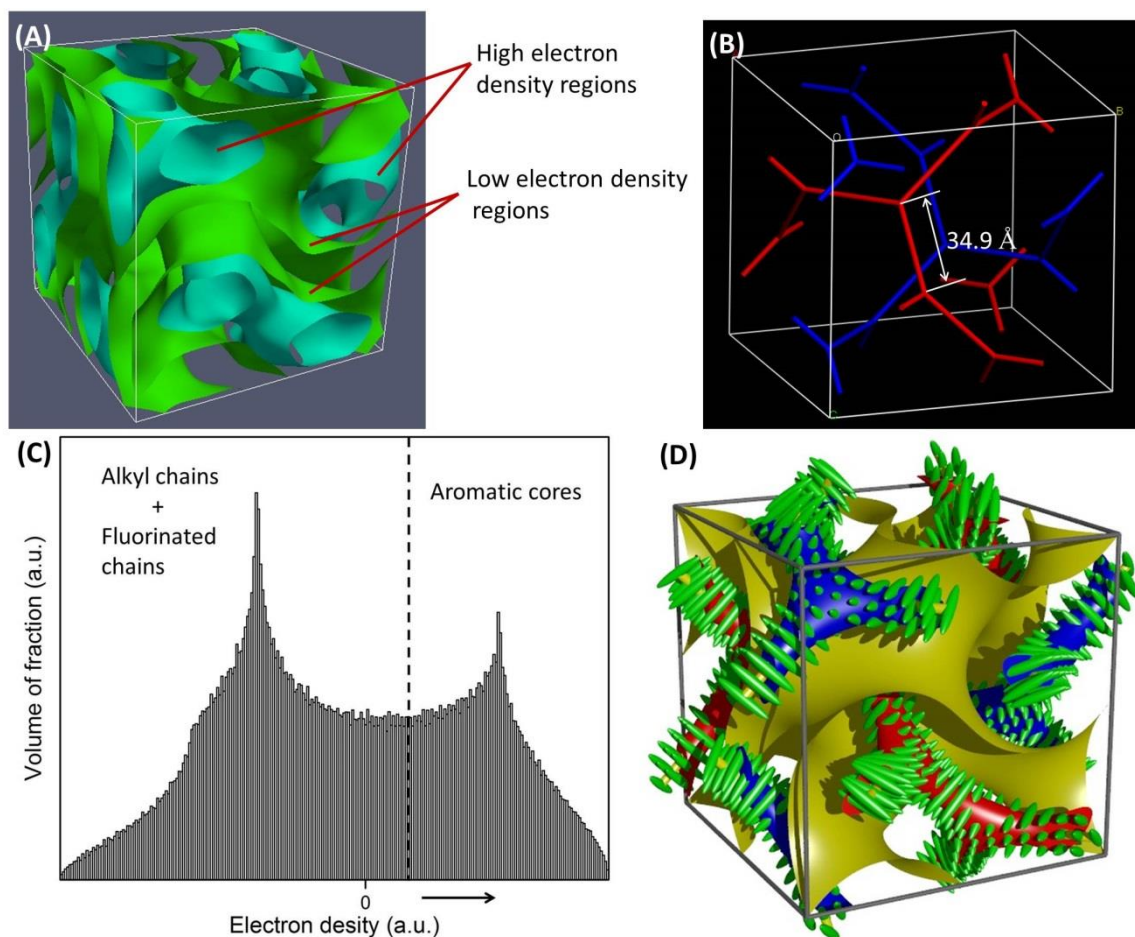


Figure 5.5 The $Ia\bar{3}d$ phase of compound **A4**: (A) reconstructed electron density map, the high-density blue isoelectron surfaces enclose the aromatic cores, and the low-density green regions are filled by the mixture of the alkyl the fluorinated terminal chains; (B) scheme of the two interpenetrating networks formed by the aromatic cores; (C) electron density histogram corresponding to the map in (A); (D) The two networks (red and blue) of the $Ia\bar{3}d$ phase decorated with schematic mesogens (rod-like molecular cores, green) showing the molecular twist along the network segments [4]. The gyroid minimum surface is also shown (yellow).

As suggested by the electron density map, the two interpenetrating networks of the $Ia\bar{3}d$ phase are made up of the aromatic rods, and the surroundings are filled by the aliphatic and the fluorinated terminal chains. Considering the shape of the molecules, the high conjugated aromatic rods lie perpendicular to the network segments, with their directions twisting gradually along the segment. Moreover, to satisfy the packing conditions at the junction points, the handedness of the twists are the same in the same network (blue: right-handed; red: left-handed). The schematic picture showing the twisted molecules

(rod-like molecular cores, green) along the network segments (red and blue) and the gyroid minimum surface (yellow) is presented in Figure 5.5D.

Based on the lattice parameter, the length of the network segment is 34.9 Å and the number of the molecules in one unit cell is around 446 (assuming the density of the phase is 1.0 g cm⁻³). As in the $Ia\bar{3}d$ unit cell there are 24 segments, each segment contains ~18 molecules. The distance between the molecules is around 4.5 Å (typical π - π interaction distance), it can be estimated that in one segment there are ~8 pairs of molecules (34.9 Å/8 \approx 4.4 Å). The twist in molecular direction between neighboring $Ia\bar{3}d$ junctions (at each junction the molecular direction is perpendicular to the plane formed by the three joining segments) is 70.5°, consequently it can be calculated that there is an average rotation/twist of 8.8° in molecular orientation between neighboring molecular pairs. This twisting angle is consistent with previously reported in other compounds [4]. As the two networks in the $Ia\bar{3}d$ phase have opposite chirality, although there is long-range helical order in each of the two interpenetrating infinite networks, there is no net chirality.

5.3.1.2 $Im\bar{3}m$ Phase

The small-angle diffraction pattern of compound **A4** in the $Im\bar{3}m$ Phase, at 102 °C is shown in Figure 5.6. The relative q positions of the reflections are $\sqrt{4}$, $\sqrt{6}$, $\sqrt{8}$, $\sqrt{10}$, $\sqrt{12}$, $\sqrt{14}$, $\sqrt{16}$, $\sqrt{18}$, $\sqrt{20}$, $\sqrt{22}$ and so on, in line with the $Im\bar{3}m$ space group symmetry. The indexing of diffractions are shown in Figure 5.6 and listed in Table 5.3. The best-fit lattice parameter $a = 155.7$ Å. Similar to previously found triple network $Im\bar{3}m$ phase, (321) is the strongest peak while other peaks are much weaker.

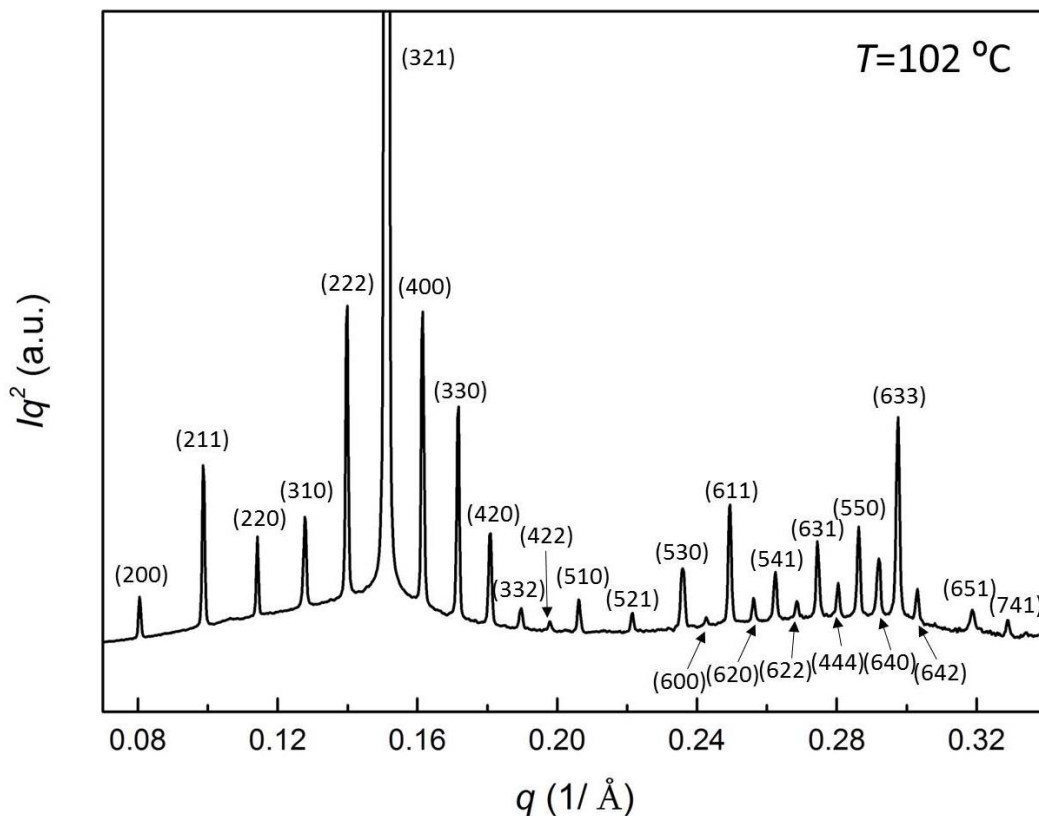


Figure 5.6 Small-angle powder diffractogram of the $Im\bar{3}m$ phase of compound **A4** recorded at $102\text{ }^{\circ}\text{C}$. Vertical axis is scaled that (321) is out of range, to show the weaker diffraction peak.

Table 5.3 Experimental and calculated d -spacings of the observed SAXS reflections of the $Im\bar{3}m$ phase in compound **A4** at $102\text{ }^{\circ}\text{C}$

(hkl)	$d_{\text{obs.}}$ -spacing (\AA)	$d_{\text{cal.}}$ -spacing (\AA)	intensity	Phase
(200)	78.0	77.9	0.4	
(211)	63.7	63.6	2.5	0
(220)	55.1	55.0	0.7	
(310)	49.1	49.2	1.4	1
(222)	44.9	44.9	5.1	0
(321)	41.6	41.6	100.0	1
(400)	38.8	38.9	5.5	0
(330)	36.7	36.7	3.6	0
(411)				
(420)	34.7	34.8	1.6	0
(332)	33.1	33.2	0.2	
(422)	31.7	31.8	0.1	

(510) (431)	30.5	30.5	0.3	
(521)	28.4	28.4	0.2	
(530) (433)	26.6	26.7	0.6	
(600) (442)	25.9	26.0		
(611) (532)	25.2	25.3	2.0	
(620)	24.5	24.6	0.2	
(541)	24.0	24.0	0.4	
(622)	23.4	23.5	0.2	
(631)	22.9	23.0	0.7	
(444)	22.4	22.5	0.3	
(550) (543) (710)	22.0	22.0	0.9	
(640)	21.5	21.6	0.5	
(633) (552) (712)	21.1	21.2	4.1	
(642)	20.7	20.8	0.3	
(651) (732)	19.7	19.8	0.2	
(741) (554)	19.1	19.2	0.1	
$a = 155.7 \text{ \AA}$				

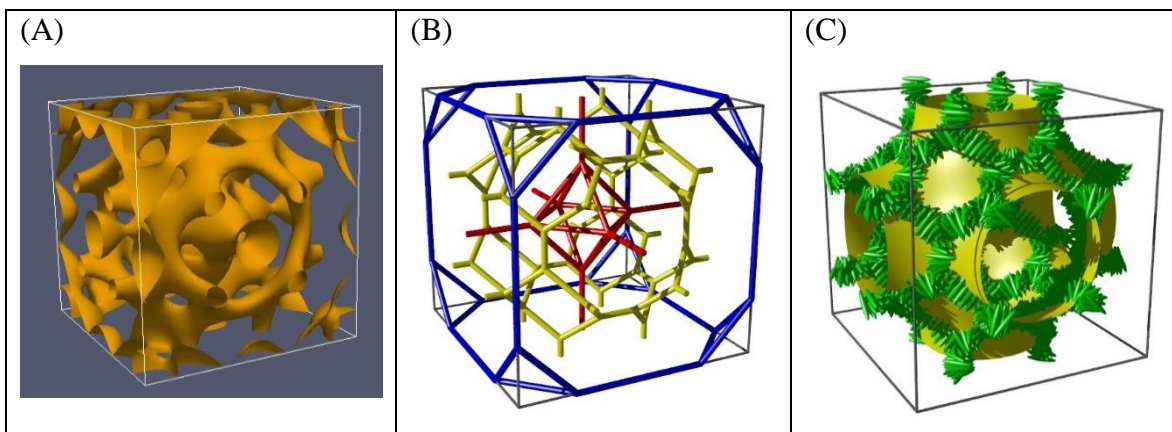


Figure 5.7 (A) Electron density map of the triple network $Im\bar{3}m$ phase. (B) Network representation of the triple network $Im\bar{3}m$ phase. (C) Schematic molecular model of the triple network $Im\bar{3}m$ phase. (B) and (C) are taken from [4].

5.3.1.3 The chiral isotropic liquid phase

The formation of chiral isotropic liquids is a consequence of chiral self-sorting in isotropic liquids. Compound A4 shows very complex phase transitions on first heating. However, on cooling and second heating, only the transition between the normal isotropic phase and the chiral isotropic phase takes place at 117 °C, which becomes glassy below 70 °C. According to SAXS results as shown in Figure 5.8, only a diffuse scattering ring can be seen in both of the isotropic states, and very little difference can be seen above and below the phase transition on the SAXS diffractograms at all.

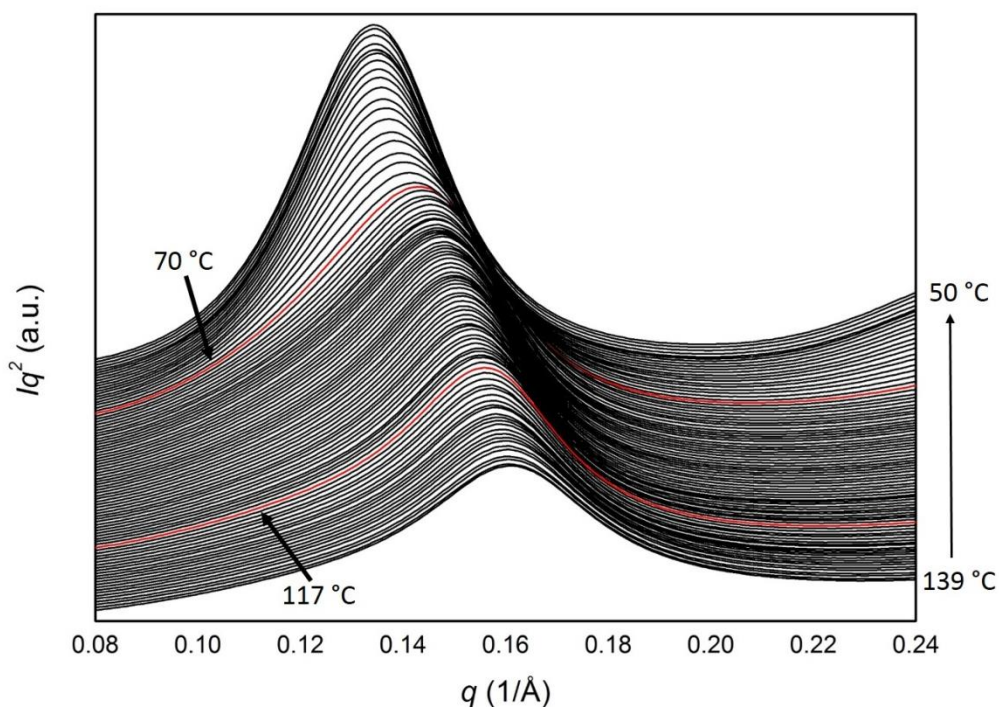


Figure 5.8 SAXS diffraction pattern of **A4** on cooling. The Iso – Iso^[*] transition at 117 °C is barely visible, while the glass transition at 70 °C is more evident.

5.3.2 Chirality changes during phase transitions by CD spectroscopy

In order to better examine the Iso^[*] phase and its transformation to and from Iso and Cub_{bi} phases, circular dichroism (CD) spectroscopy experiments have been carried out to

investigate quantitatively how the chirality changes/develops in the chiral isotropic phase and during its transition to other phases.

The CD spectroscopy experiments have been carried out at station B23, Diamond Light Source. A vertical beam setup is used so that the thin film sample ($\sim 4\text{-}5\ \mu\text{m}$), sandwiched between two quartz plates, can be placed on top of a Linkam microscope stage for temperature control, without losing sample volume due to sample flow particularly in the liquid phases. The two quartz plates were glued together to minimize change of sample thickness during heating and cooling, and the cell was infiltrated with the sample in the isotropic phase by capillary force. The size of the beam is only $\sim 1.0\ \text{mm}$ in diameter, allowing us to pick up smaller homo-chiral domains than on a conventional lab machine.

A typical UV-Vis spectrum of the polycatenar compounds studied in this project is shown in Figure 5.9. The strongest absorption peak is centred around 380 nm, from 320 to 430 nm. Maximum CD effect is thus expected at the edge of the absorption peak at $\sim 430\ \text{nm}$ in such samples.

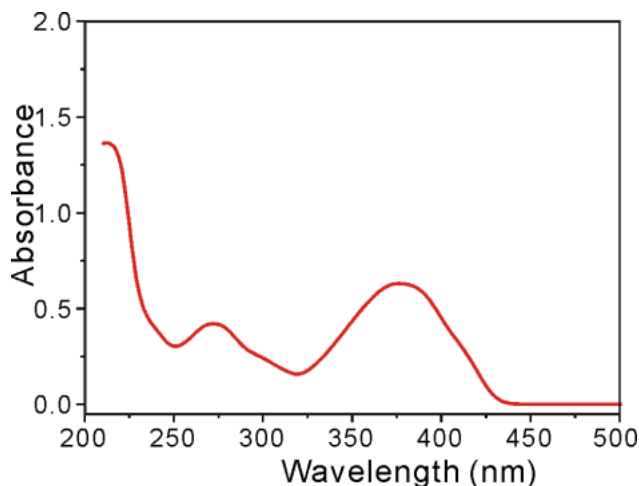


Figure 5.9 UV-Vis spectrum of compound **B15**, 0.4 mg/4ml solution in THF with sample thickness of 2 mm.

5.3.2.1 Iso – Iso^[*] transition in compound **A4**

The fact that the thin film sample can only be prepared from the isotropic phase means that the first heating cannot be observed for sample **A4**, but on both subsequent heating and cooling, a clear first order transition is observed in the CD spectra (Figure 5.10) between the achiral isotropic phase (Iso) and the chiral isotropic phase (Iso^{*}).

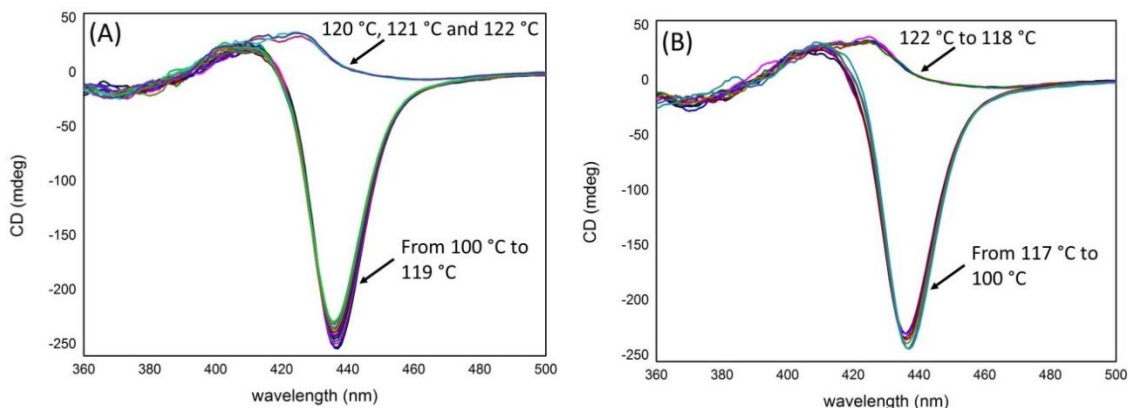


Figure 5.10 CD spectra of compound **A4** on heating (A) and cooling (B).

The CD signal in the Iso^[*] phase is almost constant in the temperature range examined, it decreases only slightly with increasing temperature, possibly due to more thermal fluctuation at higher temperatures. The transition to and from the isotropic phase is highly reversible, with a hysteresis of 2 °C.

5.3.2.2 Iso – Iso^[*] - $Ia\bar{3}d$ phase transitions in compound **B8**

On cooling from the achiral isotropic (Iso) phase, compound **B8** first transforms to the chiral isotropic phase (Iso^[*]), before it transforms into the achiral $Ia\bar{3}d$ phase. The Iso^[*] phase is in fact monotropic, as the $Ia\bar{3}d$ phase transforms directly to the achiral isotropic phase on subsequent cooling. There is in fact another short-lived (less than 30 s) transient phase observed on fast cooling, which will be discussed in detail in the next chapter. However, as the current CD experiments were carried out stepwise, with data collection time at each temperature more than five minutes, this transient phase does not concern us

here.

The CD spectra (Figure 5.11) show, as expected, no CD signal in the achiral Iso and $Ia\bar{3}d$ phases. CD signals are observed in the Iso^[*] phase but shows a strong dependence on the temperature. Such temperature dependence is in fact reversible on heating (from Iso^[*] phase before it converts to the $Ia\bar{3}d$ phase), with very little hysteresis between heating and cooling at all. To show that reversibility more clearly, the height of the CD peak is plotted as a function of temperature and shown in Figure 5.12. It is evident that the two curves overlap almost exactly.

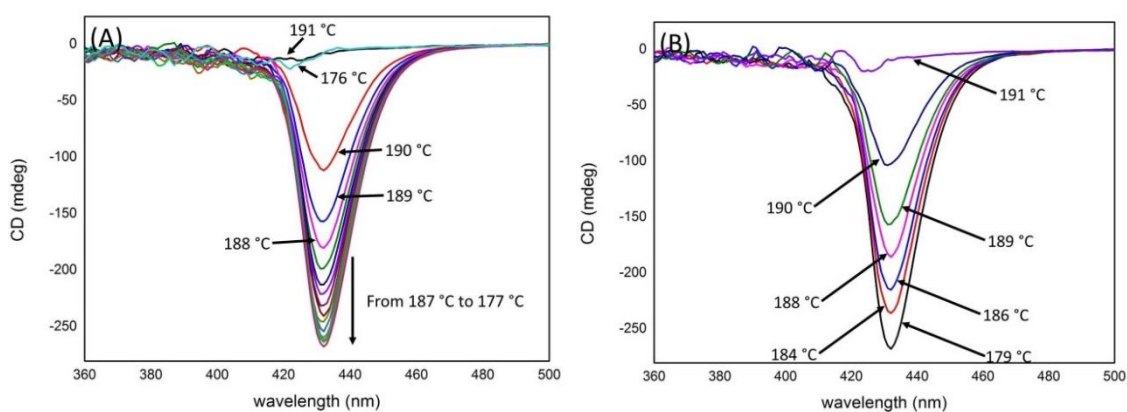


Figure 5.11 CD spectra of compound B8. (A) On cooling from Iso (191 °C), to Iso^[*] and to $Ia\bar{3}d$ phase (176 °C). (B) On heating from Iso^[*] to Iso (191 °C).

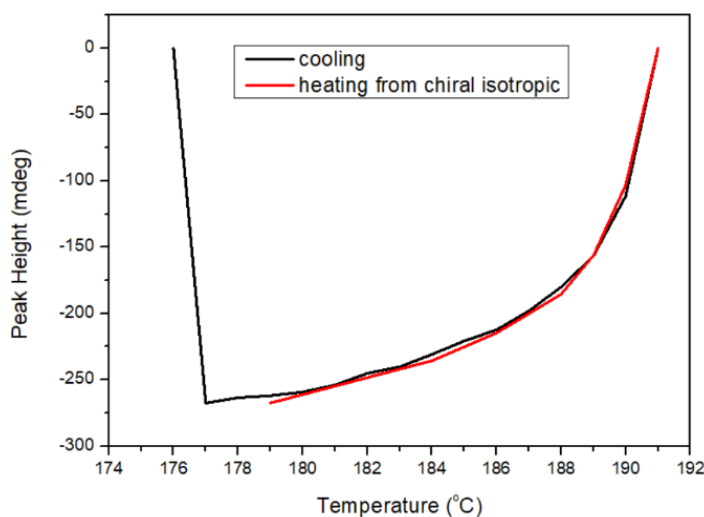


Figure 5.12 CD peak height as a function of temperature in the Iso^[*] phase. Above 191 °C the phase transforms to achiral isotropic phase, and below 176 °C to $Ia\bar{3}d$ phase.

The increase in the magnitude of the CD signal with decreasing temperature in compound **B8** has all the features of a second order transition, and reminds one of the spontaneous magnetization in a magnetic system below the Curie point. In fact, a power law relationship can be established between CD signal and $(T_c - T)$ where T_c is the critical temperature of the transition. Fitting of the experimental data as shown in Figure 5.13 gives that

$$CD = 1.5 \times 10^2 \times (T_c - T)^{0.24}$$

where $T_c = 190.3 \text{ } ^\circ\text{C}$.

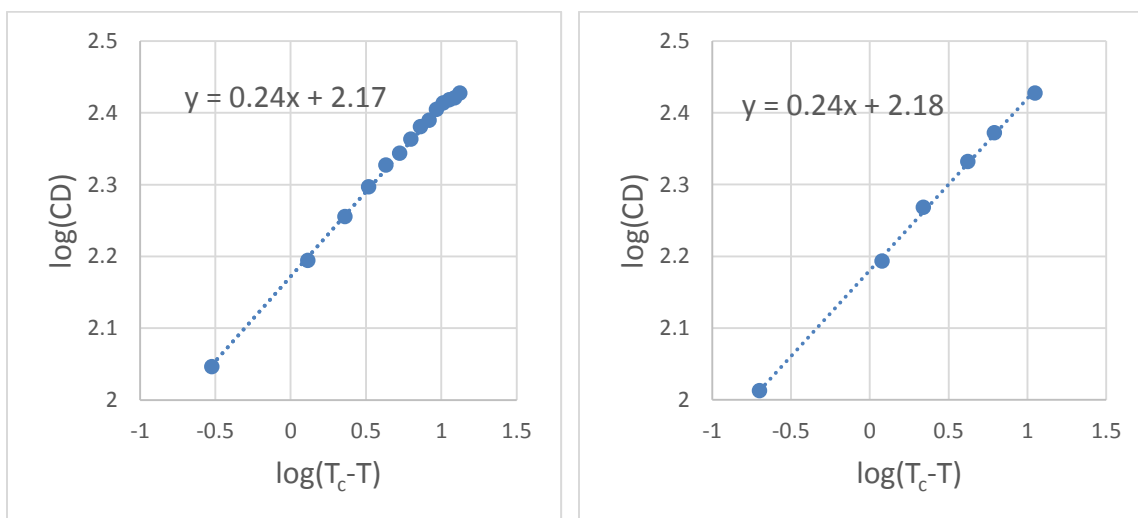


Figure 5.13 Fitting of the $\log(CD)$ as a function of $\log(T_c - T)$. left: cooling; right: heating.

The critical transition between Iso and Iso^[*] phase, is analogous to the magnetization of a spin system. The local fluctuation of the chirality (formation of local chiral domains), becomes more and more correlated with decreasing temperature, in a similar fashion as spin-spin interaction leading to net magnetization in an Ising system. In fact the critical exponent of 0.24, retrieved from the above mentioned data fitting, is in between those of a 2D Ising model (1/8) and a 3D Ising model (0.33).

5.3.2.3 Iso – Iso^[*] - $Im\bar{3}m$ phase transitions in compound **B9**

Compound **B9** on cooling from the isotropic phase transforms to the chiral isotropic

phase at ~ 190 °C, which on further cooling transforms to the triple network $Im\bar{3}m$ phase. The transition to $Im\bar{3}m$ phase has high hysteresis, that on heating it only transforms back to the Iso^[*] phase above 185 °C. However, in the stepwise (in change of temperature) CD experiment, it is expected that the system is closer to equilibrium.

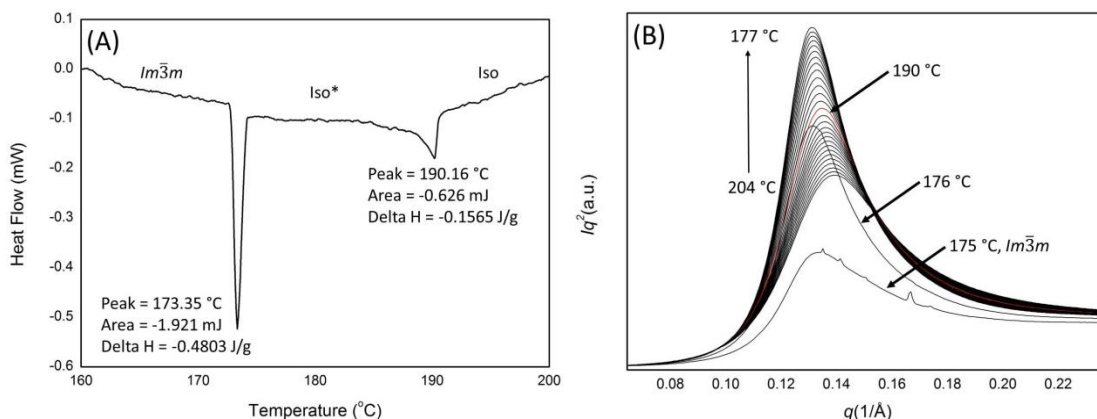


Figure 5.14 (A) DSC trace at 5 °C/min cooling rate and (B) diffraction pattern of compound **B9** at 10 °C/min cooling rate.

The CD spectra collected for compound **B9** on cooling from achiral isotropic phase indeed show strong CD signal both in the Iso^[*] and the $Im\bar{3}m$ phases (Figure 5.15). In the Iso^[*] phase there is a steeper increase of the CD signal with decreasing temperature, compared to the 2nd order transition observed for compound **B8**. However, this transition is not as sharp as observed in compound **A4**. This is more clearly shown in Figure 5.16, where the CD peak value is plotted against temperature. The fact the system is in equilibrium is clearly shown by the reversibility of the observed CD signals on cooling and subsequent heating. In the $Im\bar{3}m$ phase the CD signal increases with decreasing temperature but the slope is much smaller than in the Iso^[*] phase. However, in terms of CD signal, the transition between the Iso^[*] and the $Im\bar{3}m$ phases is smooth, i.e. there is no evident change in the value of the CD signal at the transition. This seems to suggest that all three networks in the $Im\bar{3}m$ phase should possess the same chirality, otherwise a reduction of the net chirality is expected if two of them have opposite chirality to that of the other.

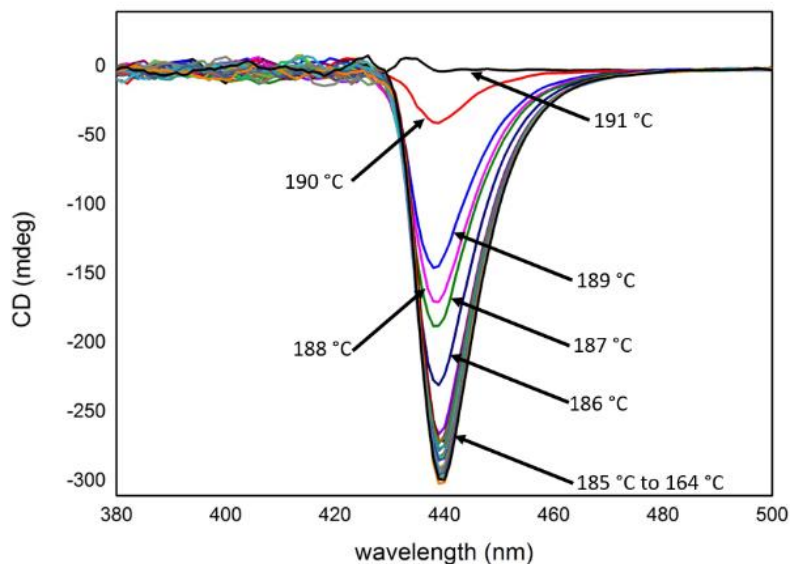


Figure 5.15 CD spectra of compound **B9** on cooling.

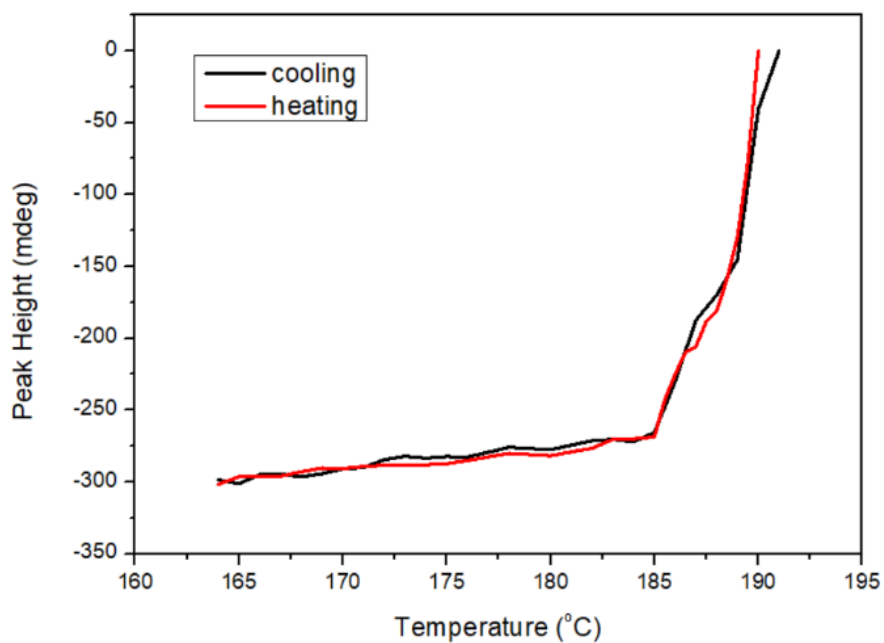


Figure 5.16 CD peak height as a function of temperature for compound **B9**.

5.4. Conclusions

We have observed the formation of chiral isotropic liquids, double network $Ia\bar{3}d$ phase, and triple network $Im\bar{3}m$ phase by a number of achiral polycatenar rod-like molecules, using small angle X-ray scattering and CD spectroscopy. The formation of the chiral

isotropic liquids is caused by the spontaneous mirror-symmetry breaking in isotropic liquids, and the transition can be either first order or second order, or somewhere in between. At the molecular level, our results suggest it is a consequence of the spontaneous segregation of chiral molecular conformers.

References

1. J. Malthete, A. M. Levelut, N. H. Tinh, Phasmids – a new class of liquid-crystals. *J. Phys. Lett.* **46**, 875-880 (1985).
2. M. Impéror-Clerc, Thermotropic cubic mesophases. *Curr. Opin. Colloid Interface Sci.* **9** (6), 370-376 (2005).
3. X. B. Zeng, G. Ungar, M. Impéror-Clerc, A triple-network tricontinuous cubic liquid crystal. *Nat. Mater.* **4**, 562-567 (2005).
4. C. Dressel, F. Liu, M. Prehm, X. B. Zeng, G. Ungar, C. Tschierske, Dynamic Mirror-Symmetry Breaking in Bicontinuous Cubic Phases. *Angew. Chem.* **26**, 13331 – 13336 (2014).
5. C. Dressel, T. Reppe, M. Prehm, M. Brautzsch, C. Tschierske, Chiral self-sorting and amplification in isotropic liquids of achiral molecules. *Nature Chemistry* **6**, 971-977 (2014).

Chapter 6

Smectic-Q Phase – the First Non-cubic Bicontinuous Phase with Orthogonal Twisted Columns¹

6.1 Introduction

Thermotropic liquid crystals encompass a wide range of phases, from the simplest nematic, used in most LC displays, to those with structures of extraordinary complexity on the micro- or nanoscale. Such complex structures are of considerable interest for nanotechnology in their own right, but they also have parallels in other soft matter, in many cases first having been found and understood in thermotropics, then replicated in block copolymers or lyotropic LC. Determining their structure can involve intricate detective work. Nevertheless, in most cases a solution is found relatively soon after the phase is discovered. One notable exception is the so-called Smectic-Q (SmQ) phase, which has puzzled researchers ever since its discovery in 1983. In this chapter we report what we believe to be the solution: a unique bicontinuous phase that is non-cubic, made up of orthogonal twisted columns, and showing chirality even in achiral compounds.

Since its initial discovery, SmQ phase has been reported and discussed several times in chiral compounds. In most cases such molecules consisted of an aromatic rod-like core with two identical chiral end-chains attached, one at each end (1,2). SmQ is very sensitive to enantiomeric purity, and has so far only been observed in nearly pure enantiomers. The phase is normally observed immediately below the isotropic liquid (Iso) phase, and on further cooling is found to transform to the antiferroelectric smectic-C phase (SmC*_A). The unit cell height is also similar to the two-layer period in SmC*_A. On this basis, SmQ has been considered as a complex organization of small layer-like SmC*_A grains (2), as a result of the conflict between the tendencies for the chiral molecules to twist and, at the same time, form flat smectic layers.

¹ Manuscript to be submitted.

With the help of single domain X-ray diffraction, the space group of the SmQ phase has been determined unequivocally as $I4_122$ (3). Using diffraction intensities, the validity of certain geometric models have also been analysed more quantitatively (3). In a recent attempt (4) the model suggested in (3) was further modified based on electron density maps. However, the proposed models still fail to rationalize adequately the existence of the SmQ phase, its structural chirality, and how its existence is linked to the intrinsic chirality of the molecules.

While SmQ is observed in enantiopure compounds, the $Ia\bar{3}d$ (Gyroid) bicontinuous cubic (Cub_{bi}) phase is often observed in their racemic mixtures (2), or in compounds with the two end chains having opposite chiralities (4). It has been pointed out (5) that by making chiral the Cub_{bi} structures, the resulting lattices distort to tetragonal with different symmetries, including that of SmQ ($I4_122$). Tetragonal distortion of the $Ia\bar{3}d$ cubic, albeit to a $I4_1/acd$ symmetry, has been reported for a racemic mixture, adding support to such a connection between $Ia\bar{3}d$ and SmQ structures (6). Another commonly observed phase in such compounds is the triple-network cubic phase (7), which has recently found to be chiral and can form from both chiral and achiral compounds, in the latter through dynamic mirror symmetry breaking (8). Its space group is formerly assigned as $Im\bar{3}m$ in achiral compounds, and recently sometimes also referred to as $I432$, because of its chirality; the question of its true space group symmetry is still open. It has been reported that, starting from the triple-network cubic phase in a racemate, by increasing enantiomeric excess a phase transition to SmQ is observed (9).

In the current work we report the observation of the chiral SmQ phase in *achiral* rod-like compounds, and present a new structural model showing SmQ to be a non-cubic bicontinuous phase formed by interwoven orthogonal helices, first of its kind.

6.2 Results and Discussions

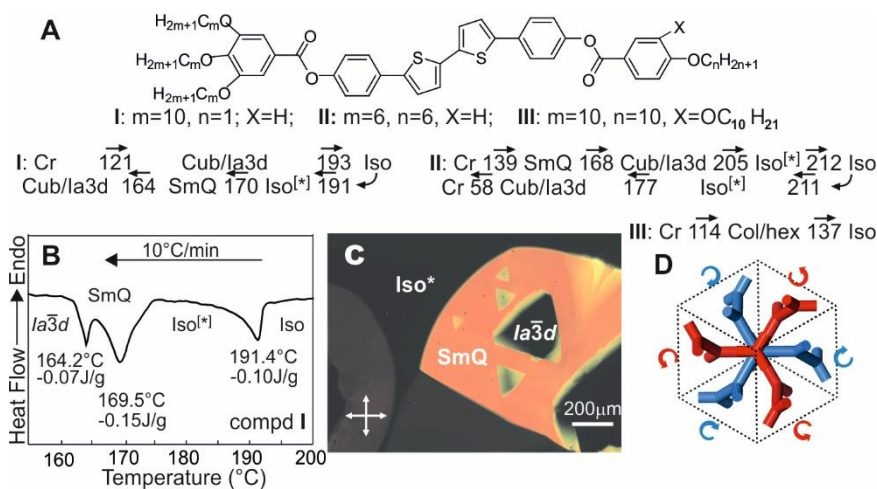


Figure 6.1 (A) Structure and phase transition temperatures (in °C) of compounds **I** – **III** (Cr = crystal, Iso^[*] and Iso = chiral and achiral isotropic liquid). (B) DSC curve of **I** on cooling at 10 K/min. (C) Polarized optical micrograph of **I** in a 0.1 mm flat capillary at 164 °C after cooling from 200 °C at 10 °C/min. The birefringent SmQ forms from Iso^[*] and then transforms to cubic $Ia\bar{3}d$ within ~30 s. (D) Unit cell of Cub/ $Ia\bar{3}d$ phase viewed along [111], to help explain triangular shape of SmQ domains growing within it; the two enantiomeric networks are shown in red and blue.

Compounds **I** - **III** and their mesophase sequence are shown in Fig. 6.1A (**I** and **II** are B8 and B1 respectively as tabulated in Chapter 5). They belong to the series of achiral mesogens reported recently to form the achiral double-network $Ia\bar{3}d$ phase (Fig. 6.1D); through dynamic mirror symmetry breaking, they also form the chiral triple-network cubic phase, as well as the recently discovered chiral isotropic liquid (Iso^[*]) phase (10).

The SmQ phase is found in **I** below ~169 °C on cooling at rates ≥ 10 K/min from the Iso^[*] which forms at ~191 °C (Fig. 6.1B). The chiral nature of Iso^[*] is confirmed by circular dichroism (CD) spectroscopy. However, SmQ is metastable and quickly transforms to Cub/ $Ia\bar{3}d$. This is illustrated in Fig. 6.1C, where SmQ domains (birefringent, yellow) emerging from the Iso^[*] phase, are being replaced by Cub/ $Ia\bar{3}d$ domains growing inside them. Crucially, the Cub/ $Ia\bar{3}d$ domains have a triangular shape, with a 3-fold instead of 6-fold rotational symmetry expected from an achiral cubic phase viewed along [111] (Fig. 6.1D). This confirms the chirality of SmQ, as it acts as chiral environment breaking the degeneracy of growth rates of Cub/ $Ia\bar{3}d$ domains along the six directions normal to its [111]. Due to the opposite hands of the two Cub/ $Ia\bar{3}d$ networks, the chiral environment favours the growth of three of the six facets, the observed facets being the slow-growing ones. While examples of

triangular chiral crystals exist (II), we are not aware of examples of triangular non-chiral crystals or LCs.

In contrast to compound I, in II the SmQ forms on heating from solution-grown crystals, and is stable between 140 and ~ 168 °C (Fig. 6.1A). On cooling, a 30 K hysteresis is observed for the Iso^[*]- $Ia\bar{3}d$ transition, the origin of which will be discussed further below.

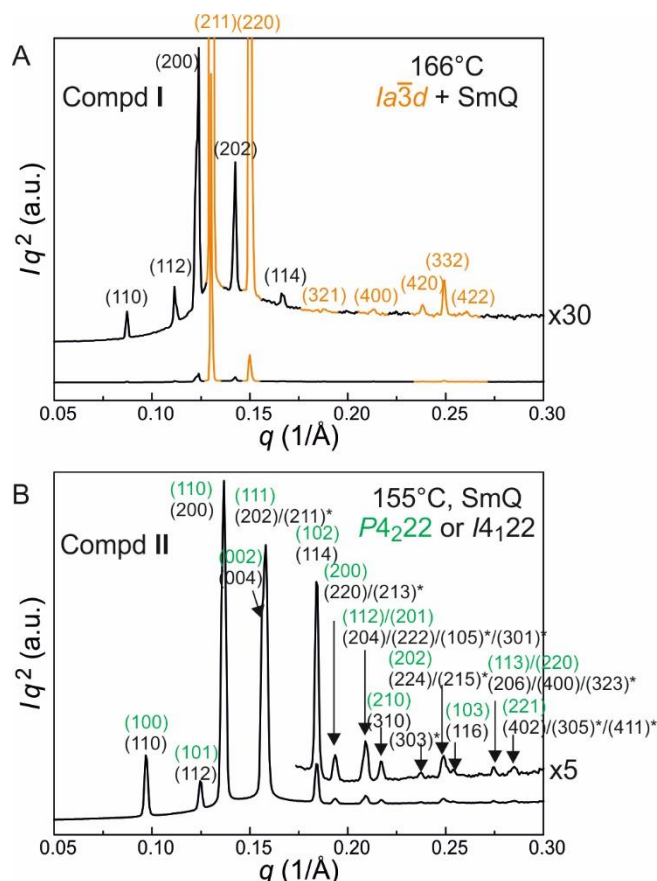


Figure 6.2 X-ray diffractograms of SmQ phase. (A) Mixture of Cub/ $Ia\bar{3}d$ and SmQ in I at 166 °C after 50 K/min cooling from Iso. Indexed peaks of Cub/ $Ia\bar{3}d$ and SmQ are orange and black, respectively. (B) Pure SmQ in compound II, recorded at 155 °C on heating. Indices on the smaller $P4_222$ and the full-size $I4_122$ unit cell are shown in green and black, respectively. Lattice parameters ($I4_122$): $a=b=91.7\text{Å}$, $c=159.8\text{Å}$. [*] marks hkl of peaks belonging to $I4_122$ only, and cannot be alternatively indexed on the $P4_222$ cell. Note the isolated (303)^[*].

While at wider angles (4-5 Å) X-ray diffraction is only diffuse, at small angles a series of sharp Bragg peaks are seen for the SmQ in compounds I and II (Fig. 6.2). In both cases they can be indexed on a tetragonal lattice with $a=b=101.7\text{Å}$, $c=178.8\text{Å}$ in I and $a=b=91.7\text{Å}$, $c=159.8\text{Å}$ in II. The d-spacings and indices are listed in Tables 6.1 and 6.2. The extinction rule observed agrees with $I4_122$ symmetry, as previously determined. Note that most peaks have indices (in black) with both $h+k$ and l even. If only such peaks were present, the dif-

fraction pattern could be indexed to a smaller, also tetragonal unit cell, with $a'=b'=a/\sqrt{2}$, and $c'=c/2$, with symmetry $P4_222$ (green). In our powder pattern there is one peak that can only be indexed as (303) of the $I4_122$ lattice. Other non- $P4_222$ peaks may also be present, but most of them coincide with some $P4_222$ peaks (Fig. 6.2b). Previously it was only by single crystal diffraction that the SmQ space group was determined as $I4_122$ (3). The weakness of the non- $P4_222$ peaks suggests, however, that the $I4_122$ structure of SmQ is probably a slightly modified/distorted $P4_222$, a starting point for our next step in determining the SmQ structure.

Table 6.1 Experimental and calculated d -spacings of the observed SAXS reflections of the $I4_122$ phase in compound **I** at 166 °C on cooling

(hkl)	$d_{\text{obs.}} - \text{spacing } (\text{Å})$	$d_{\text{cal.}} - \text{spacing } (\text{Å})$	<i>intensity</i>
(110)	72.1	71.9	7.51
(112)	56.1	56.0	11.0
(200)	50.7	50.9	100
(202)	44.2	44.2	44.3
(114)	37.6	38.0	6.19
$a = 101.7 \text{ Å}, c = 178.8 \text{ Å}$			

Table 6.2 Experimental and calculated d -spacings of the observed SAXS reflections of the $I4_122$ phase in compound **II** at 155 °C on fast heating

(hkl)	$d_{\text{obs.}} - \text{spacing } (\text{Å})$	$d_{\text{cal.}} - \text{spacing } (\text{Å})$
(110)	64.7	64.8
(112)	50.3	50.3
(103)/(200)	46.0	46.1/45.9
(004)/(202)/(211)	39.9	40.0/39.8/39.7
(114)	34.1	34.0
(213)/(220)	32.5	32.5/32.4
(105)/(204)/(222)/(301)	30.0	30.2/30.1/30.0/30.0
(310)	28.9	29.0
(303)	26.5	26.5
(224)/(115)	25.3	25.2/25.2
(116)	24.7	24.6
(206)/(323)/(400)	22.9	23.0/23.0/22.9
(305)/(402)/(411)	22.0	22.1/22.0/22.0
$a = 91.7 \text{ Å}, c = 159.8 \text{ Å}$		

Using the intensities of the six strongest diffraction peaks of compound **II**, and the $P4_222$ space group symmetry, we are able to reconstruct candidate electron density (ρ) maps of the SmQ phase, with different combinations of phase angles. Among the six strongest peaks, two can have alternative (hkl) indexing, i.e. (200) or (103) and (202) or (211). We took the

assumption that $P4_222$ peaks are much stronger than non- $P4_222$ ones, and attributed the intensity of the two peaks to (200) and (202), respectively. As a consequence the reconstructed ρ maps, even though using an $I4_122$ lattice, in fact consist of four unit cells of $P4_222$ space group (Fig. 6.3A). For five of the six diffraction peaks, (110), (112), (200), (004) and (114), the corresponding structure factors F_{hkl} are always real, hence their phase angles can only be 0 or π . At the same time, F_{202} is always imaginary, hence its phase angle is either $\pi/2$ or $-\pi/2$. The total number of phase combinations is 64, while the number of distinct maps is much smaller, as some differ merely in a shift of origin or being mirror images. The best map is chosen on its physical merits.

Some typical electron density maps are shown in Figure 6.3 below. In all the maps the phase of the (202) peak is $\pi/2$, and the phase combination of the other five peaks are shown on top of each map. Two iso-electron surfaces were shown for each map: the red surface encloses the high density regions and the blue low density regions. The maps in Fig. 6.3a,c can be easily eliminated as they do not show uniform distribution of high and low density regions expected. The map shown in Fig. 6.3b is better in terms of uniformity of the electron density distribution. However, the low density regions are observed along lines ($x=1/4, y=1/4, z$) and ($x=3/4, y=3/4, z$), but not along ($x=1/4, y=3/4, z$) and ($x=3/4, y=1/4, z$). This is hard to explain as the high density aromatic core surrounds the four lines symmetrically, and their electron densities are thus expected to be similar if not exactly equal. Map in Fig. 6.3d is the best as it shows uniform distribution of both high and low electron densities. The position of the low densities are furthest away from the high density aromatic cores. As described in detail in the main text, our simulation and molecular models are thus built on the basis of the map in Fig. 6.3d.

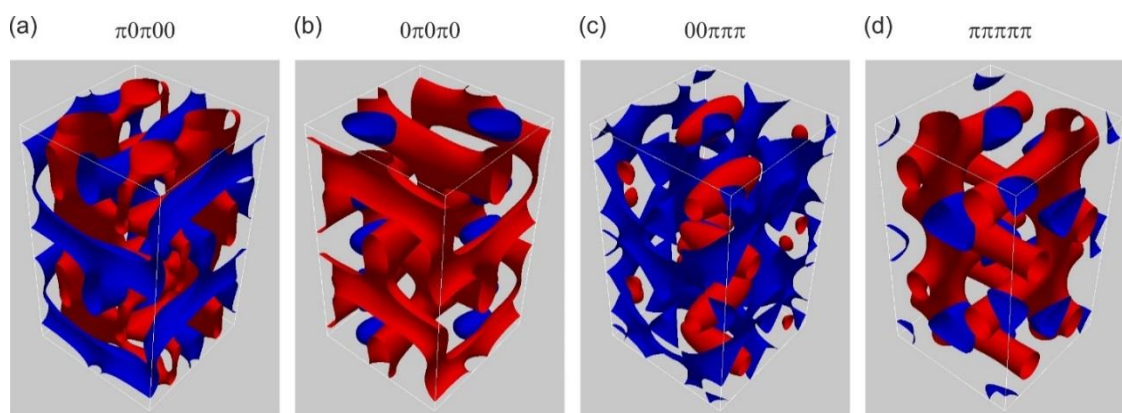


Figure 6.3 Reconstructed candidate electron density maps of SmQ phase with different phase combinations. The phase combination used is shown on top of each map.

The selected 3D ρ map (Fig. 6.4A) shows the high- ρ regions of the unit cell (55% of the total volume) occupied by the aromatic cores. It is evident from the map that the structure consists of columns. In the full cell there are four of them along x , four along y and two along z . Molecular assembly into columns is in line with the fact that in the phase diagram SmQ is close to $\text{Cub}/Ia\bar{3}d$, which itself consists of columnar segments. The arrangement of horizontal columns bears strong resemblance to that proposed by Pansu et al. (3), even though in their model smectic blocks were assumed instead of columns.

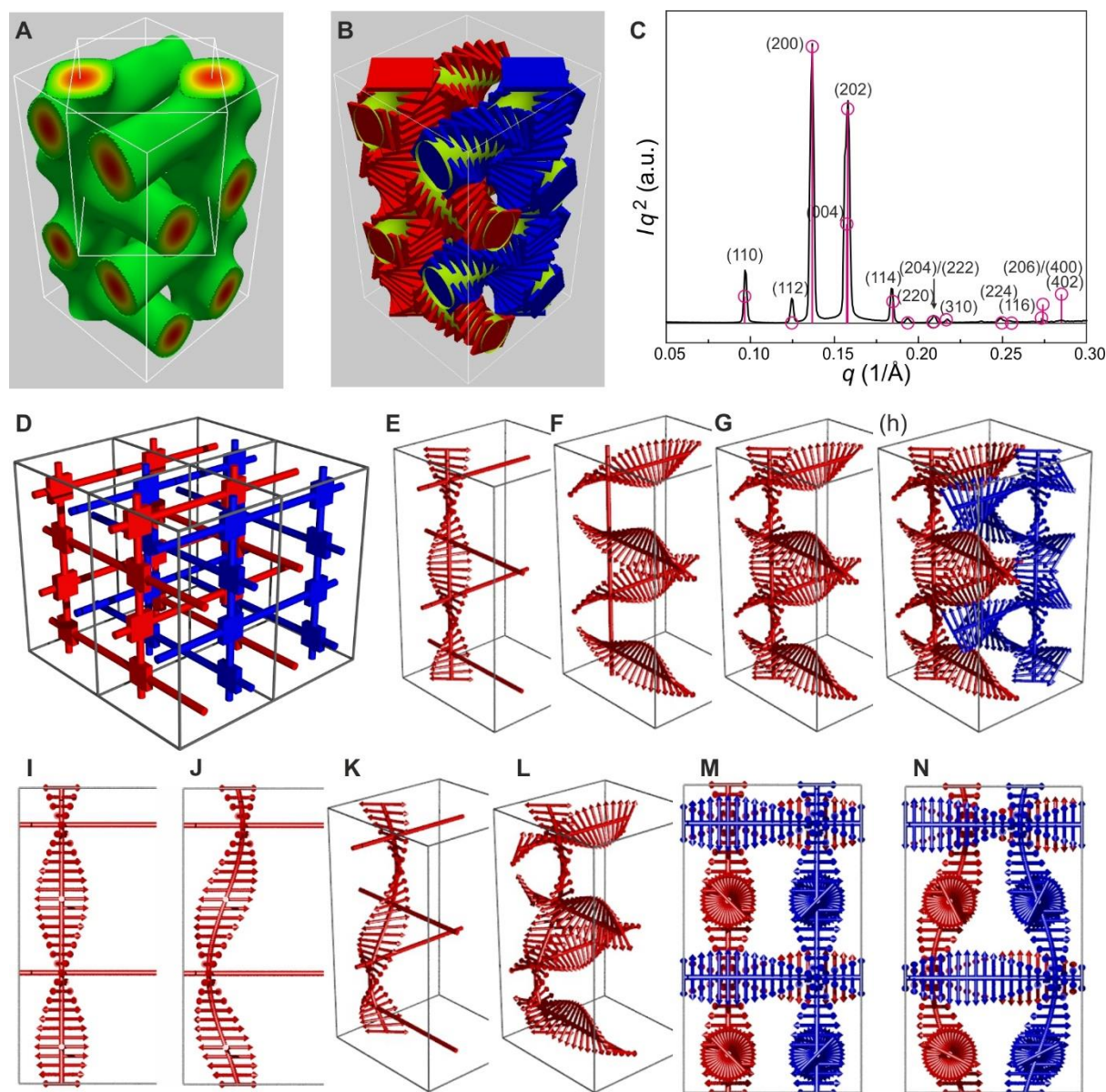


Figure 6.4 Results of X-ray analysis and structure of the SmQ. (A) Electron density (ρ) map (compound **II**, 155 °C), showing the high-to-medium ρ regions in the unit cell (red = high, green = medium, none = low). The large (true) cell corresponds to $I4_122$, while the small approximant cell has $P4_222$ symmetry, and contains $1/4$ of the full cell volume. (B) Geometric model, superimposed on the map in (A), used to

simulate the diffraction pattern, where helical columns consist of stacked solid plates representing the strata consisting of ~ 4 molecular cores lying side-by-side normal to column axis (*cf.* Fig. 6.5B). (C) Comparison of experimental X-ray diffractogram and that simulated from the model in (B) (red vertical lines topped by circles). (D) Double network representation of the SmQ structure, with planar four-way junctions (2×2 unit cells). (E-H) The helicity of the columns is generated by rotation of the molecular strata, each represented by a double arrow, about the column axis. Within a cell, a stratum rotates by 360° along a vertical column (E), and by 180° along a horizontal column (F). The two networks have the same helical sense (G-H). Distortion of the vertical column from a 4_2 (I) to a 4_1 helix (J-L). (M) View along [100] on the complete structure with $P4_222$ symmetry (2 cells) and (N) $I4_122$ symmetry (1 cell).

According to the 3D ρ map, in the SmQ structure there are layers of horizontal columns aligned, alternatively, along x and y. There are also two vertical columns in a unit cell, each intersecting with four horizontal columns. The resulting periodic structure consists of two infinite interpenetrating networks of columns with planar 4-way junctions (Fig. 6.4D). The two networks are related by a shift of $(1/2, 1/2, 1/2)$. Each junction joins four segments, two horizontal and two vertical. For compound **II**, the length of the horizontal segments between junctions is $a=91.7\text{\AA}$, and between vertical segment $c/4=40.0\text{\AA}$. The distance between columns matches well with the extended molecular length of 46\AA . The four segments at a junction are always within a vertical plane, and we expect the molecules near the junction to orient mainly perpendicular to that plane. At successive junctions along a horizontal column, the molecular orientation is the same, while along a vertical segment it is rotated by 90° .

As has been hypothesised before for bicontinuous $Ia\bar{3}d$ and triple-network cubic phases formed by rod-like molecules (9,12), the columnar segments consist of stacked layers (strata) of several molecules lying side-by-side. The columns are helical (9) because successive strata rotate about the column axis to avoid steric clash between pendant chains. We postulate similar twisted columns in the SmQ phase. The twist is shown in Fig. 6.4 and is described in the caption. It is estimated that the total number of molecules in a unit cell of **II** is 935, from which we calculate that the strata contain 4 molecules each, are separated by 4.5\AA , and are rotated by 8.9° and 10.2° relative to their neighbours in the horizontal and vertical columns, respectively. For comparison in the $\text{Cub}/Ia\bar{3}d$ in compound **II**, the rotation angle is 8.4° , as calculated from the distance and rotation of successive 3-way junctions. Had the twist between strata been the same in horizontal and vertical segments, the length of the former would have been twice that of the latter, and the c/a ratio would have been 2 instead of the observed 1.74. The fact that horizontal segments are slightly longer than half the vertical segments can be explained by the planar junctions, all of them vertical, having finite thick-

ness. Close to the junction, the twist of the strata in all four adjoining branches would cause a clash, which can be resolved by some spreading of the junction area in a horizontal direction.

As already proposed for the bicontinuous $Ia\bar{3}d$ and triple-network cubic phases (9), to minimize the clash between columns at a junction and allow their smooth merger, all converging columns should possess the same chirality. This then allows long-range propagation of homochirality throughout the network. Furthermore, the body-centred symmetry $I4_122$ mandates that the two networks in the SmQ be exactly the same apart from a shift by $(1/2, 1/2, 1/2)$. Accordingly, both networks are chiral and of the same handedness, which results in net chirality of the phase, and explains why it had previously been found only in enantiopure chiral compounds: molecules of wrong intrinsic chirality will destabilize the phase.

Based on the above, we are able to construct a geometrical model of the SmQ phase and to simulate its diffraction pattern. The geometric model is shown in Fig. 6.3B, where the high- ρ core of each molecular stratum is represented by a platelet, whose length should be that of the molecular core, and width depends on the number of molecules in the stratum. The total rotation angle in the horizontal and vertical segments is 180° and 90° , respectively. Using the length l and width w of the plates as the fitting parameters, a very good fit between simulated and experimental patterns is achieved as shown in Fig. 6.3C. The best-fit parameters are $l=31.4\text{\AA}$ and $w=29.0\text{\AA}$, agreeing reasonably well with estimation (30\AA and 25\AA) on the basis of molecular size, cell dimensions and density estimation. It should be noted that the model in fact has a $P4_222$ instead of $I4_122$ symmetry, and the quality of fit achieved supports our earlier assumption that the structure is very close to that of $P4_222$.

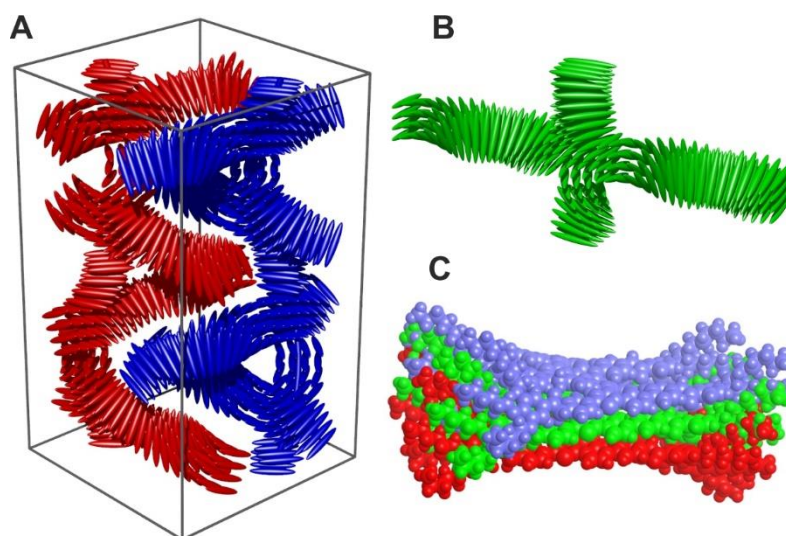


Figure 6.5 Twisted networks and molecules. (A) Perspective view of an $I4_122$ SmQ unit cell. (B) Converging columns at junctions possess the same chirality to avoid clashes. (C) Model of three successive strata, each containing four molecules of **I**, with interstrata spacing of 4.5 Å and a 8° twist. Each stratum is represented by four rigid rods in (A, B).

However, the true space group of the structure is $I4_122$, as established by single crystal X-ray study before (3), and supported by the observation of non- $P4_222$ reflections in our powder diffractograms. The reduction in symmetry from $P4_222$ to $I4_122$ can be explained as follows. The helical symmetry of the vertical columns will be reduced from 4_2 to 4_1 if the centres of the molecular strata are shifted off-axis. They then follow a helical path (Fig. 6.4I,J). The junction points and the horizontal columns are similarly shifted in different directions at different heights (Fig. 6.4K,L,N), resulting in $I4_122$ lattice symmetry. This sideways shift is small though, since our diffraction pattern simulation suggests that for large distortions many unobserved $I4_122$ peaks, such as (101), would become visible. A perspective view of the full $I4_122$ unit cell (with an exaggerated distortion) is shown in Fig. 6.5A.

The current model of the SmQ phase is also able to explain its extremely low birefringence. Taking the birefringence Δn of a perfectly ordered nematic phase to be Δn_0 , Δn of the SmQ phase is equal to $S\Delta n_0$, where $S = (3\langle \cos^2\theta \rangle - 1)/2$ is the orientational order parameter, with θ the inclination of the molecular axis to the optic axis, i.e. z-axis. For molecules in the vertical columns, θ is always 90°, hence $\cos^2\theta = 0$ with corresponding $S = -0.5$; in contrast, molecules in the horizontal columns have their angles evenly distributed in the range 0° to 90°, hence $\langle \cos^2\theta \rangle = 1/2$ with $S = 0.25$. Considering that a unit cell contains 8 horizontal and 2 vertical columns of lengths a and c , respectively, and assuming that the number of molecules is proportional to column length, the SmQ order parameter comes to $S = (2a - c)/(8a + 2c) = 0.022$. Optical measurement of the hexagonal columnar phase ($S_{\text{hex}} = -0.5$) formed by compound **III** with the same aromatic core as **I** and **II**, suggest that $\Delta n_0 = \sim 0.2$ (see next paragraph), hence that Δn of SmQ is expected to be ~ 0.004 .

In order to measure the birefringence of LC samples, polarized optical microscopy was carried out on an Olympus BX50 microscope equipped with a Mettler FP85 hot stage. To study the low-birefringent SmQ phase molten sample was introduced by capillary action into a 100 µm thick rectangular capillary. For highly birefringent phases, such as the columnar phase in compound **III**, the sample was melted between a glass slide and a cover slip and the film thickness was controlled to 4 µm by fragments of Mylar film as spacers. Birefringence of the hexagonal columnar phase, Δn_0 , of the reference compound **III** was determined by a Berek

compensator in areas of maximum brightness of developable domains (“spherulites”) where the columns were lying parallel to the glass surface at 45° to the crossed polarizers. Birefringence was determined to be $\Delta n = -0.09$. Assuming perfect orientation of columns within the developable domains with order parameter -0.5 , the reference birefringence of a hypothetical perfectly ordered nematic phase of compounds **I** – **III** would be $\Delta n_0 = 0.18 \approx 0.2$.

Domains of SmQ phase large enough to allow measurement of birefringence were only observed in compound **I**. However, due to the short life of SmQ in that sample, a quicker method for measuring birefringence was required. Thus a color photo was recorded first, then a full-wave (λ) plate was inserted and photos were taken in quick succession at different rotation angles of the sample. The colors were then compared with the Michel-Levy color chart. From the colors the retardation $\Gamma = 530 \text{ nm} \pm \Delta\Gamma$ was determined, where Γ is the retardation of a given domain and $\Delta\Gamma$ its deviation at a given domain orientation. Birefringence Δn was obtained from the maximum $\Delta\Gamma$, $\Delta\Gamma_{\text{max}}$, by dividing it with the sample thickness ($100 \mu\text{m}$). $\Delta\Gamma_{\text{max}}$ is found to be $\sim 400 \text{ nm}$ and thus Δn of the SmQ phase is ~ 0.004 . This is in very good agreement with the previously reported Δn value of < 0.005 (3) and our prediction from SmQ structural model.

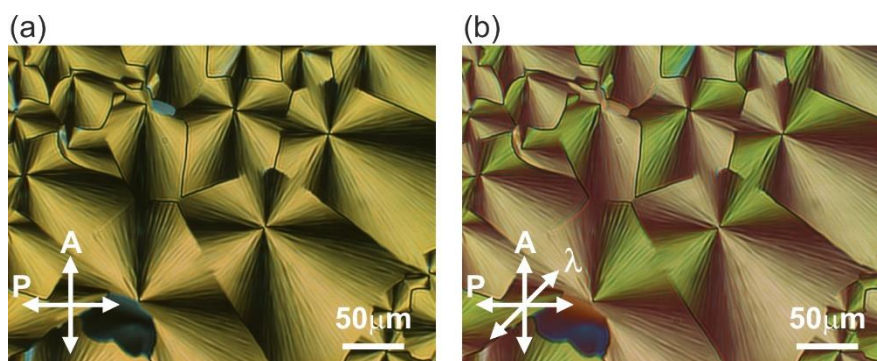


Figure 6.6 Optical micrographs of the columnar phase in compound **III** at 135°C between crossed polarizers; (a) without and (b) with λ plate. Slow axis of the retarder is indicated, together with orientation of the polarizers.

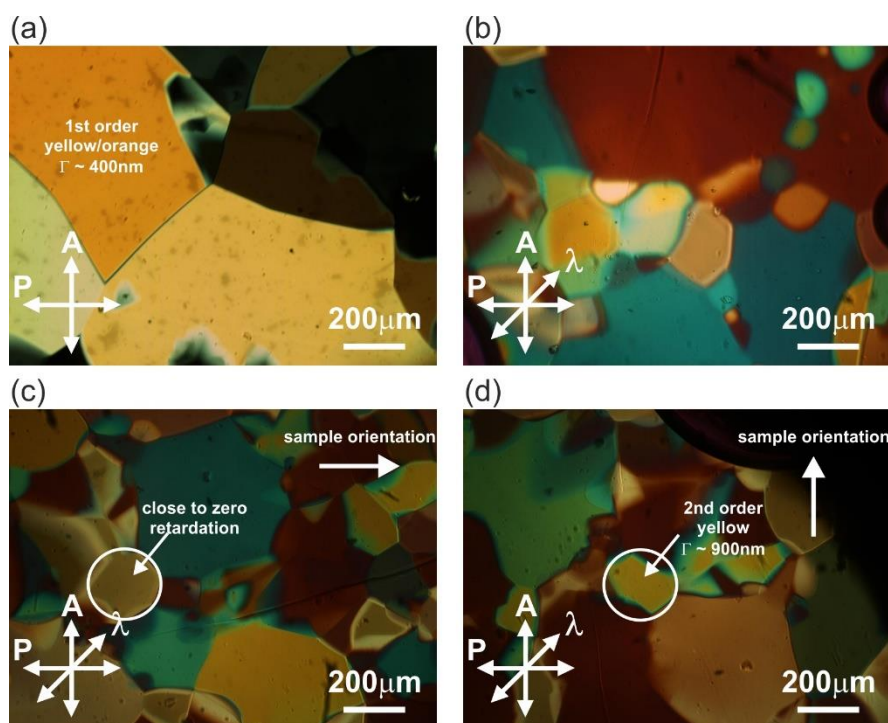


Figure 6.7 POM micrographs of DRE222 in the SmQ phase (180 °C) between cross polarizers. (a) without λ -plate, (b-d) with λ -plate. (c) and (d) are the same region but with rotation of the sample by 90°. A domain, indicated by a white circle, shows different colours when its optical axis is aligned parallel or perpendicular to the slow axis of the retarder plate.

As mentioned, we propose that the molecular twist is caused by steric clash between pendant chains on successive strata. But also, the aromatic cores are non-planar, as shown in the molecular model of three overlaying strata in Fig. 6.4B. The strata are separated by 4.1 Å and twisted by 8°, each containing 4 antiparallel molecules with their end-groups twisted in the same direction. The likely propeller-like chiral conformation of an individual molecule is due to the non-planarity of the ester groups, with a racemization barrier of $E^* = 2.6$ KJ/mol (10). The twist angle between the successive strata is a compromise between the steric avoidance of the bulky aliphatic chains and the tendency for maximum overlap of the aromatic cores. In accordance with the general principle of chirality synchronization by dense self-assembly (13-16), the close packing requires a coordinated flip of many (n) molecules to change chirality, which raises the effective re-twisting barrier to a prohibitive value of nE^* .

In compound **I** SmQ is only metastable, its formation from the chiral Iso^[*] being kinetically favoured over that of Cub/ $Ia\bar{3}d$. In **II**, it may be stable, but possibly it is again only kinetically favoured due to potential chirality of the crystalline phase from which it forms. However, what the observed phase behaviour demonstrates clearly is that any phase transition

that involves helix inversion is highly suppressed. This explains the suppression of the Iso^[*] – Cub/ $Ia\bar{3}d$ transition, which either proceeds via SmQ (in **I**) or shows a large, nearly 30 K, hysteresis (in **II**). Since Cub/ $Ia\bar{3}d$ consists of two networks of opposite chirality, to grow one of them from a dense homochiral environment requires helix inversion. Similar suppression of helix-inversion is responsible for the triangular shape of Cub/ $Ia\bar{3}d$ domains growing from the homochiral SmQ (Fig. 6.1C,D). Interestingly, it was also observed that when Cub/ $Ia\bar{3}d$ grows from the Iso^[*] liquid, its domains nucleate exclusively at boundaries between enantiomeric Iso^[*] domains (9) where both helical hands are available; this indicates that re-twisting presents a particularly high barrier in the nucleation process. The strong suppression of nucleation and growth of Cub/ $Ia\bar{3}d$ domains from Iso^[*] also suggests that Iso^[*] liquid may also consist of densely packed homochiral helical segments, albeit with only short-range positional order.

There is a certain analogy between the structure of SmQ and those of “blue phases” BPI and BPII (17), a variant of chiral nematic with an ordered array of double-twist defect lines observed in highly chiral LC. Although BP structures are on micro- and SmQ on nano-scale, both types involve orthogonal packing of helices. We also note that long-range chirality synchronization in SmQ, as well as in Iso^[*] liquid and the triple network cubic phase, all occurring in achiral compounds, may also provide new insight into how homochirality could have propagated at the beginning of life on Earth (18).

References

1. A. M. Levelut, C. Germain, P. Keller, L. Liebert, J. Billard, Two New Mesophases in a Chiral Compound. *J. Physique*, **44**, 623-629 (1983).
2. A. M. Levelut, E. Hallouin, D. Bennemann, G. Heppke, D. Loetzsch, The Smectic Q Phase, A Crystal of Twist Grain Boundaries with Smectic Order. *J. Physique II France* **7**, 981-1000 (1997).
3. B. Pansu, Y. Nastishin, M. Imperor-Clerc, M. Veber, H. T. Nguyen, New Investigation on the Tetragonal Liquid-Crystalline Phase or SmQ. *Eur. Phys. J. E* **15**, 225-230 (2004).
4. M. Vogrin, N. Vaupotic, M. M. Wojcik, J. Mieczkowski, K. Madrak, D. Pocięcha, E. Gorecka Thermotropic Cubic and Tetragonal Phases Made of Rod-Like Molecules. *Phys. Chem. Chem. Phys.* **16**, 16067-16074 (2014).
5. M. Yoneya, Toward Rational Design of Complex Nanostructured Liquid Crystals. *Chem. Rec.* **11**, 66-76 (2011).

6. A. M. Levelut, M. Clerc, Structural Investigations on 'Smectic D' and Related Mesophases. *Liq. Cryst.* **24**, 105–115 (1998).
7. X. B. Zeng, G. Ungar, M. Imperor-Clerc, A triple-network tricontinuous cubic liquid crystal. *Nat. Mater.* **4**, 562-567 (2005).
8. C. Dressel, F. Liu, M. Prehm, X. B. Zeng, G. Ungar, C. Tschierske, Dynamic Mirror-Symmetry Breaking in Bicontinuous Cubic Phases. *Angew. Chem. Int. Ed.* **126**, 13331-13336 (2014).
9. T. Yamamoto, I. Nishiyama, M. Yoneya, H. Yokoyama, Novel Chiral Effect that Produces the Anisotropy in 3D Structured Soft Material: Chirality-Driven Cubic-Tetragonal Liquid Crystal Phase Transition. *J. Phys. Chem. B* **113**, 11564–11567 (2009).
10. C. Dressel, T. Reppe, M. Prehm, M. Brautzsch, C. Tschierske, Chiral Self-Sorting and Amplification in Isotropic Liquids of Achiral Molecules. *Nat. Chem.* **6**, 971-977 (2014).
11. T. Okihara, L. Cartier, G.O.R. Alberda van Ekenstein, B. Lotz, Frustration and Single Crystal Morphology of Isotactic Poly(2-Vinylpyridine). *Polymer* (1998) **40**, 1-11.
12. M. Gharbia, A. Gharbi, H. T. Nguyen, J. Malthete, Polycatenar Liquid Crystals with Long Rigid Aromatic Cores: A Review of Recent Works. *Curr. Opin. Colloid Interface Sci.*, **7**, 312-325 (2002).
13. M. M. Green, J. W. Park, T. Sato, A. Teramoto, S. Lifson, R. L. B. Selinger, J. V. Selinger. The Macromolecular Route to Chiral Amplification. *Angew. Chem. Int. Ed.*, **38**, 3138-3154 (1999).
14. J. Malthete, A. Collet, Inversion of the Cyclotribenzylene Cone in a Columnar Mesophase: A Potential Way to Ferroelectric Materials. *J. Am. Chem. Soc.* **109**, 7544-7545.
15. C. Tschierske, G. Ungar. Mirror-Symmetry Breaking by Chirality Synchronization in Liquids and Liquid Crystals of Achiral Molecules. *ChemPhysChem*, **17**, 9-26 (2016).
16. E. Yashima, N. Ousaka, D. Taura, K. Shimomura, T. Ikai, K. Maeda, Supramolecular Helical Systems: Helical Assemblies of Small Molecules, Foldamers, and Polymers with Chiral Amplification and Their Functions. *Chem. Rev.* **116**, 13752–13990 (2016).
17. D. C. Wright, N. D. Mermin, Crystalline liquids—the blue phases. *Rev. Mod. Phys.* **61**, 385–432 (1989).
18. M. M. Green, V. Jain, Homochirality in Life: Two Equal Runners, One Tripped. *Origin Life Evol. Biosph.*, **40**, 111-118 (2010).

Chapter 7

Distorted Cubic and Other 3D Phases in Polycatenar Compounds

7.1 Introduction

Apart from the two bicontinuous cubic phases (chapter 5), and the SmQ phase (chapter 6), a number of other 3D phases have been observed in the series of polycatenar compounds studied in this project. These include a distorted $Ia\bar{3}d$ phase, a distorted $Im\bar{3}m$ phases, a diffused phase, and an orthorhombic phase with $P2_12_12_1$ symmetry. The experimental results on these phases, mostly by small angle x-ray scattering (SAXS) will be presented.

7.2 Results and Discussions

7.2.1 The distorted $Ia\bar{3}d$ phase

In polycatenar compounds **A3**, **A4**, **B10** and **B11**, a slightly distorted $Ia\bar{3}d$ cubic phase, normally observed immediately below the $Ia\bar{3}d$ cubic phase, is observed. The distortion results in an orthorhombic instead of a cubic unit cell, with three different but very similar lattice parameters a , b and c . Due to the distortion, under POM the phase is very weakly birefringent. The distortion is also bigger with decreasing temperature.

Take compound **B10** as an example, the SAXS results shows that it forms the $Ia\bar{3}d$ phase at high temperatures directly below the isotropic phase. On cooling, the $Ia\bar{3}d$ phase forms from the isotropic phase at 170 °C. It starts to deform at 164 °C, and then transforms to distorted $Im\bar{3}m$ phase (which will be discussed at the next section) at 101 °C. The diffractogram of the distorted $Ia\bar{3}d$ phase at 140 °C is shown in Figure 7.2, where the diffraction peaks are labelled with their corresponding Miller indices (hkl). As shown clearly in the diffraction pattern, the strongest two peaks of the $Ia\bar{3}d$ phase, (211) and (220), have each split into three different peaks after the distortion. Peaks which are forbidden by the $Ia\bar{3}d$ symmetry, such as (200)s and (210)s, even though weak, have now become visible due to the reduction of unit cell symmetry. The experimental and calculated d-spacings of diffraction peaks are compared in Table 7.1, and the best-fit lattice parameters are $a = 121.3 \text{ \AA}$, $b = 115.4 \text{ \AA}$, $c = 110.3 \text{ \AA}$.

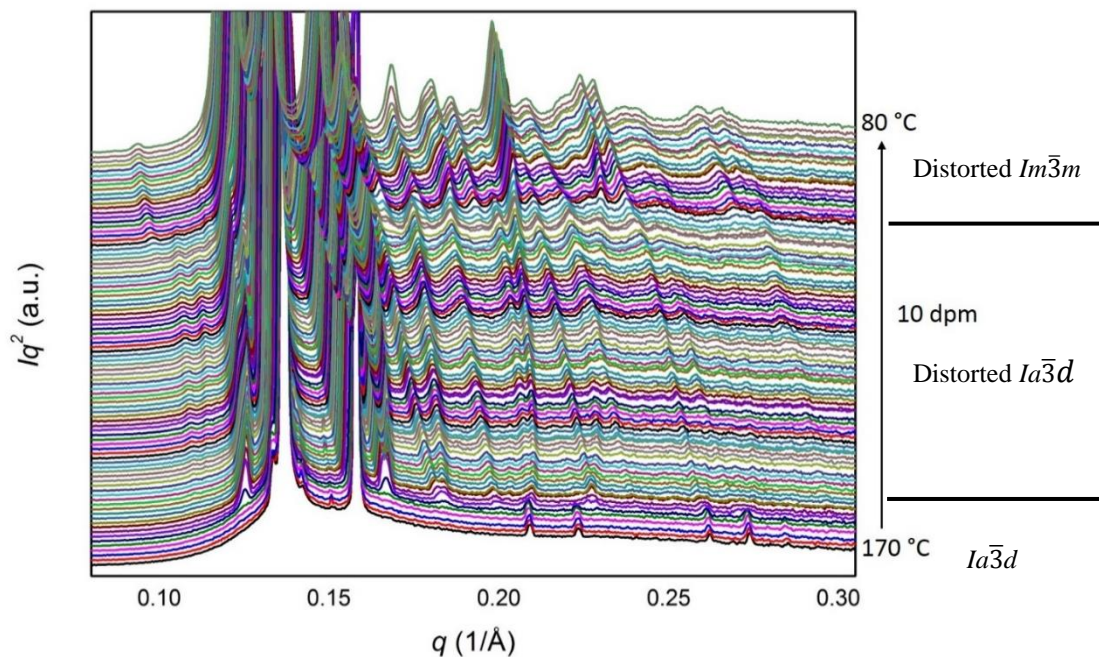


Figure 7.1 Diffraction pattern of **B10** on cooling from 170 °C to 80 °C

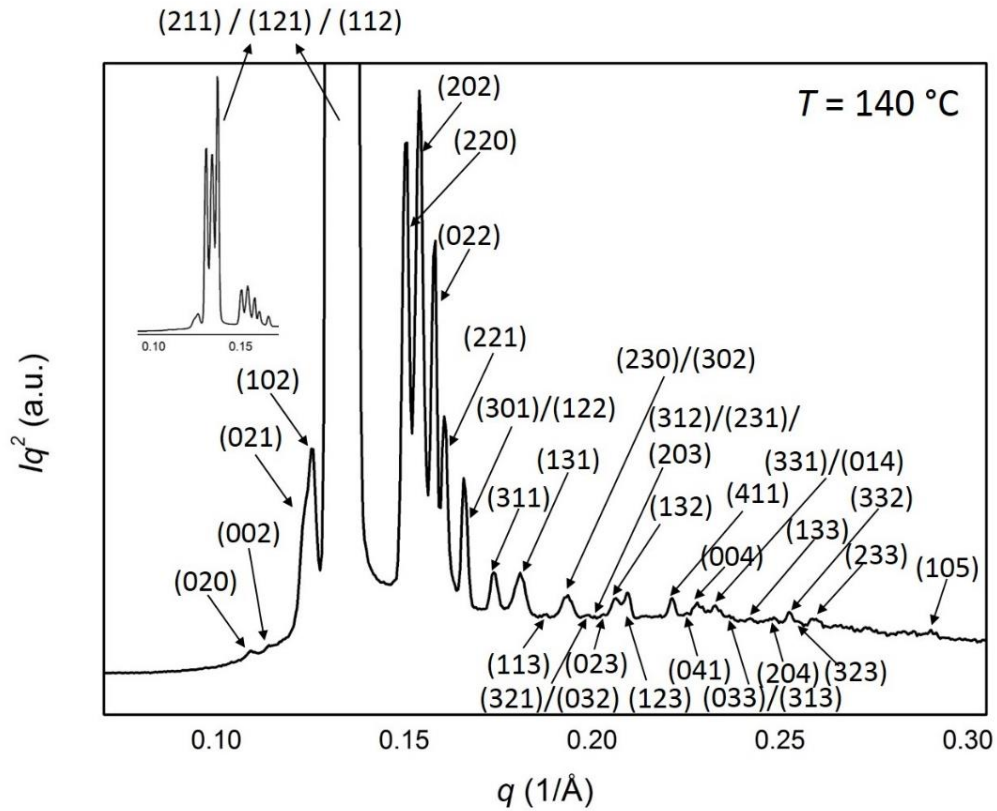


Figure 7.2 Diffraction pattern of **B10** in the distorted $Ia\bar{3}d$ phase at 140 °C.

Table 7.1 Experimental and calculated d -spacings of the observed SAXS reflections of the distorted $Ia\bar{3}d$ phase in **B10** at 140 °C. The best-fit lattice is orthorhombic with lattice parameters $a = 121.3$ Å, $b = 115.4$ Å, $c = 110.3$ Å.

(hkl)	$d_{\text{obs.}}$ -spacing (Å)	$d_{\text{cal.}}$ -spacing (Å)
(020)	57.5	57.7
(002)	55.2	55.2
(021)	51.2	51.1
(102)	50.2	50.2
(211)	48.4	48.3
(121)	47.1	47.1
(112)	46.0	46.0
(220)	41.8	41.8
(202)	40.8	40.8
(022)	39.8	39.9
(221)	39.1	39.1

(301)/(122)	37.9	38.0
(311)	36.1	36.1
(131)	34.8	34.8
(113)	33.5	33.7
(230)/(302)	32.5	32.5
(321)/(032)	31.6	31.7
(312)/(231)/(203)	31.3	31.4
(023)	31.0	31.0
(132)	30.5	30.5
(123)	30.0	30.0
(411)	28.4	28.3
(041)/(140)/(330)	27.9	27.9
(004)	27.6	27.6
(331)/(303)/(104)	27.0	27.0
(014)/(420)	26.8	26.8
(033)/(402)	26.6	26.6
(313)	26.5	26.5
(133)/(240)	26.0	26.0
(204)	25.3	25.1
(332)/(024)	24.9	24.9
(323)	24.6	24.6
(233)	24.3	24.3
(105)	21.7	21.7
$a = 121.3 \text{ \AA}, b = 115.4 \text{ \AA}, c = 110.3 \text{ \AA}$		

Distorted $Ia\bar{3}d$ phase has also been found in Compound **A3**, here the phase forms directly from the isotropic phase on cooling at 1 °C/min, from 127 to 102.5 °C. A single domain sample resulted, and enabled us to examine the X-ray diffraction patterns of the distorted $Ia\bar{3}d$ phase on rotation, in an angular range of over 90 degrees. By careful examination of these diffraction patterns, we are able to index all observed diffraction peaks at different rotation angles of the single domain. This makes it possible to observe weaker diffraction peaks, and to resolve diffraction peaks which would be overlapping on a powder diffraction

pattern. Consequently we are able to work out the exact extinction rules in the diffraction pattern, and to determine the space group symmetry of the structure, as will be explained later.

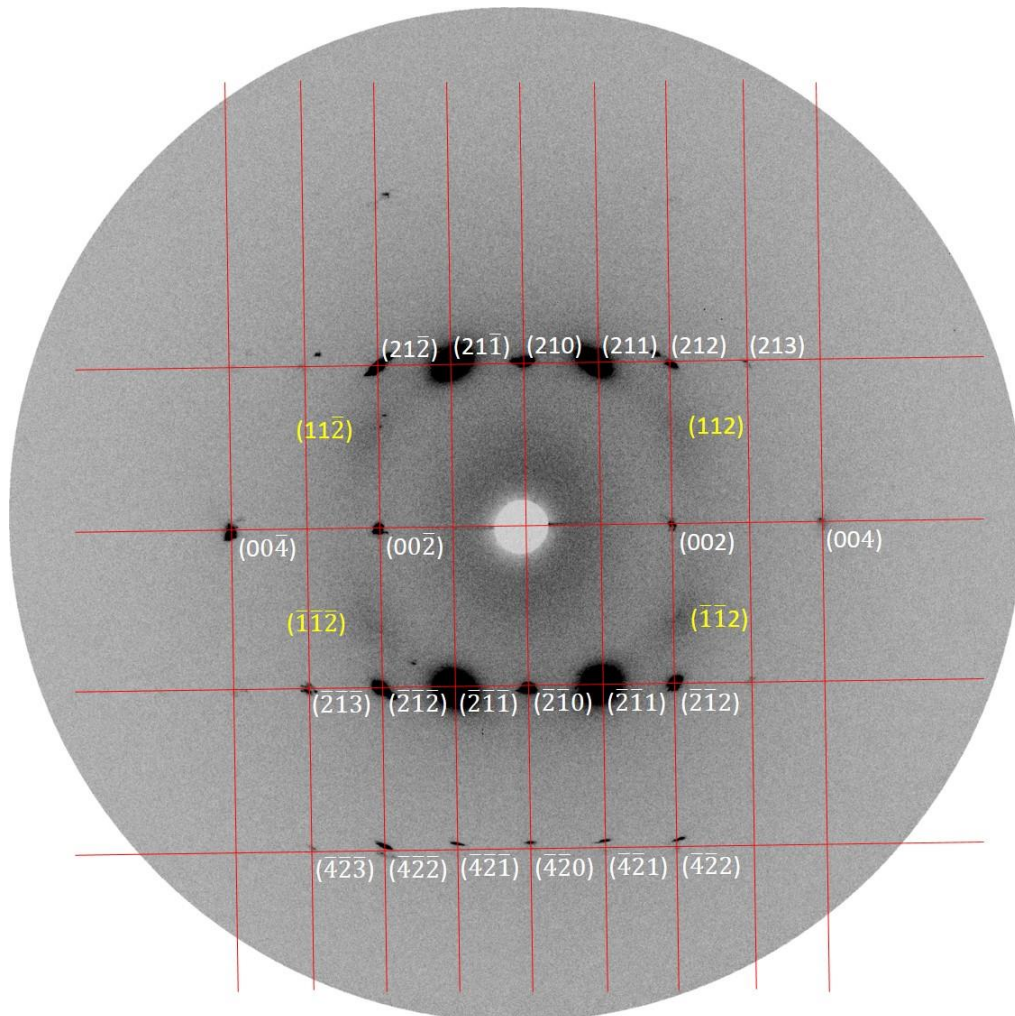


Figure 7.3 Single crystal diffraction pattern of the distorted $Ia\bar{3}d$ phase, taken with the beam along the $(1\bar{2}0)$ direction. The axis of rotation is vertical and along the (210) direction of the crystal.

A single crystal diffraction pattern of the distorted $Ia\bar{3}d$ phase is shown in Figure 7.3, with all the diffraction peaks indexed. The diffraction pattern has been identified as a cut of the Ewald sphere through the $[1\bar{2}0]$ plane of the reciprocal lattice. (211) and $(21\bar{1})$ peaks are the strongest peaks observed, but (112) and $(11\bar{2})$ peaks are much weaker in intensity as they are off the perfect diffraction conditions. The observed diffraction peaks in Figure 7.3 can be indexed on an orthorhombic lattice, and the measured and calculated d-spacings are compared in Table 7.2.

Table 7.2 Indices, measured and calculated d-spacings of diffraction peaks in the single crystal diffraction pattern of the distorted $Ia\bar{3}d$ phase, with beam along the $(1\bar{2}0)$ direction as shown in Figure 7.3.

(hkl)	$d_{\text{obs.}} - \text{spacing } (\text{\AA})$	$d_{\text{cal.}} - \text{spacing } (\text{\AA})$
(002)	51.1	51.1
(210)	46.5	46.6
(211)	42.2	42.4
(212)	34.6	34.4
(213)	27.7	27.5
(004)	25.7	25.6
(420)	23.8	23.3
(421)	23.2	22.7
(422)	21.6	21.2
$a = 108.7 \text{ \AA}, b = 90.5 \text{ \AA}, c = 102.2 \text{ \AA}$		

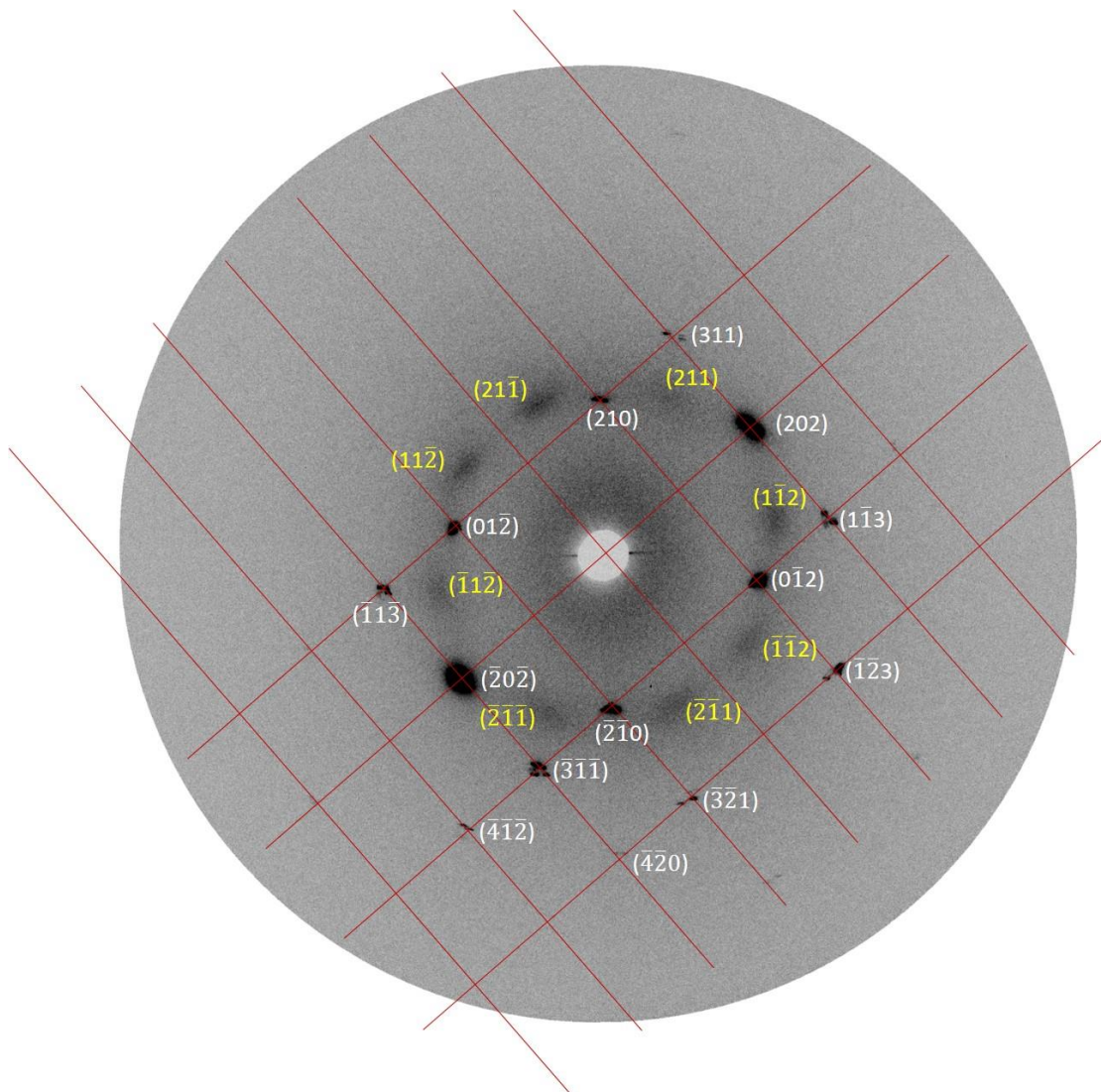


Figure 7.4 Single crystal diffraction pattern of the distorted $Ia\bar{3}d$ phase, taken with the beam along the $(1\bar{2}1)$ direction.

When the sample was rotated by 23° , another single crystal diffraction pattern of the distorted $Ia\bar{3}d$ phase is shown in Figure 7.4, again with all the diffraction peaks indexed. This time the diffraction pattern has been identified as a cut of the Ewald sphere through the $[1\bar{2}1]$ plane of the reciprocal lattice. This time (202) peak is the strongest observed. The indexing of diffraction peaks in Figure 7.4, and a comparison of the measured and calculated d-spacings are shown in Table 7.3.

Table 7.3 Indices, measured and calculated d-spacings of diffraction peaks in the single crystal diffraction pattern of the distorted $Ia\bar{3}d$ phase, with beam along the $(1\bar{2}1)$ direction as shown in Figure 7.4.

(hkl)	$d_{\text{obs.}}$ -spacing (\AA)	$d_{\text{cal.}}$ -spacing (\AA)
(210)	46.5	46.6
(202)	37.1	37.2
(311)	31.6	32.0
(321)	27.5	27.3
(420)	23.8	23.3
(412)	23.2	23.2
$a = 108.7 \text{ \AA}, b = 90.5 \text{ \AA}, c = 102.2 \text{ \AA}$		

The two single crystal diffractions shown above are only examples of the over 90 single crystal diffractograms we have analysed. In general, all diffraction peaks observed can be explained by an orthorhombic lattice with lattice parameters $a = 108.7 \text{ \AA}$, $b = 90.5 \text{ \AA}$, $c = 102.2 \text{ \AA}$. We are able to confirm that all (210) peaks, (210), (201), (120), (102), (021) and (012) are observed. At the same time no $(h00)$ peaks with odd h , $(0k0)$ with odd k and $(00l)$ with odd l are observed. This suggests that the distorted has a space group symmetry $P2_12_12_1$, the only one that satisfies the observed extinction rules.

With the space group determined, we will be able to reconstruct the electron density maps of the distorted $Ia\bar{3}d$ phase, using the observed diffraction intensities. It is expected that the structure is very similar to that of the $Ia\bar{3}d$ phase, with two interpenetrating networks. The network segments joining at a junction point, will be slightly different in length though. It should be noted that $P2_12_12_1$ is non-centrosymmetric and in fact chiral. It could be one of the reasons behind the distortion of the $Ia\bar{3}d$ structure, that the overall balance between the left-handed and the right-handed networks is broken. Alternatively, the biaxiality of the aromatic backbone could lead to the breaking of perfect 3-fold symmetry at the junction point. All these will be explored in the future. It should also be mentioned the distorted $Ia\bar{3}d$ phase has

been observed before in other polycatenar compounds, but due to the experimental resolution limit, it was assigned to a tetragonal lattice instead [1].

7.2.2 The distorted $Im\bar{3}m$ phase

As mentioned above already, on further cooling of the distorted $Ia\bar{3}d$ phase in compound **B10**, it transforms into a distorted $Im\bar{3}m$ phase. The diffraction pattern is shown in Figure 7.5 and the indexing of the diffraction peaks is shown in detail in Table 7.4. The best-fit lattice parameters are $a = 217.0 \text{ \AA}$, $b = 190.0 \text{ \AA}$, $c = 183.5 \text{ \AA}$. All the diffraction peaks (hkl) observed has $h+k+l$ even, suggesting a centred lattice. Apart from that, we have not yet been able to determine the space group of the structure, but it is expected to be only a slightly distorted version of the cubic $Im\bar{3}m$ phase.

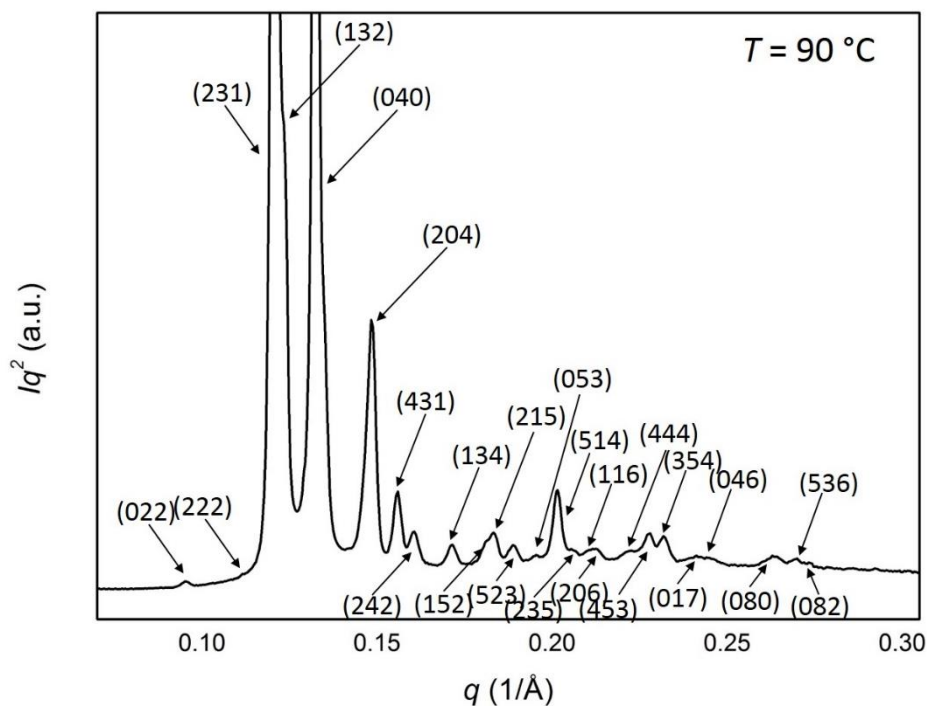


Figure 7.5 Diffraction pattern of **B10** at 90 °C.

Table 7.4 Experimental and calculated d -spacings of the observed SAXS reflections of the distorted $Im\bar{3}m$ phase in **B10** at 90 °C. The lattice is centred orthorhombic with lattice parameters $a = 217.0 \text{ \AA}$, $b = 190.0 \text{ \AA}$, $c = 183.5 \text{ \AA}$.

(hkl)	$d_{\text{obs.}}$ -spacing (\AA)	$d_{\text{cal.}}$ -spacing (\AA)
(022)	66.0	66.0
(222)	56.4	56.4
(231)	52.1	52.4

(132)	50.8	50.7
(040)/(330)	47.5	47.5
(204)/(332)/(510)	42.4	42.3
(431)	40.3	40.2
(242)	39.1	39.3
(134)	36.7	36.6
(152)	34.7	34.7
(215)/(433)	34.3	34.2
(523)/(334)/(044)/(442)/(343)	33.2	33.2
(053)	32.2	32.3
(514)	31.2	31.1
(235)/(006)/(260)	30.5	30.5
(116)/(062)	29.8	29.9
(206)	29.6	29.4
(444)	28.3	28.2
(453)	27.6	27.7
(354)	27.1	27.1
(017)	26.0	26.0
(046)	25.7	25.7
(080)	23.8	23.8
(536)	23.3	23.3
(082)	22.9	23.0
$a = 217.0 \text{ \AA}, b = 190.0 \text{ \AA}, c = 183.5 \text{ \AA}$		

7.2.3 The diffused $Ia\bar{3}d$ phase

Compound **B2** and **B13** form the $Ia\bar{3}d$ phase which seems to be normal with powder X-ray diffraction. However, when the compounds were cooled from the isotropic phase and big domains form, interesting diffusion stripes were observed in the diffraction patterns, as shown in Figure 7.6. The stripes pass through intensity maxima that are at the same positions as observed for the normal $Ia\bar{3}d$ phase, as indicated in Figure 7.6 of the (211) and (220) peaks. The main stripes that we observe, go along the (110) direction, either between neighbouring (220) and (211) peaks, or between two neighbouring (211) peaks. This is suggesting the existence of phononic fluctuations, along (110) directions, in such $Ia\bar{3}d$ phases.

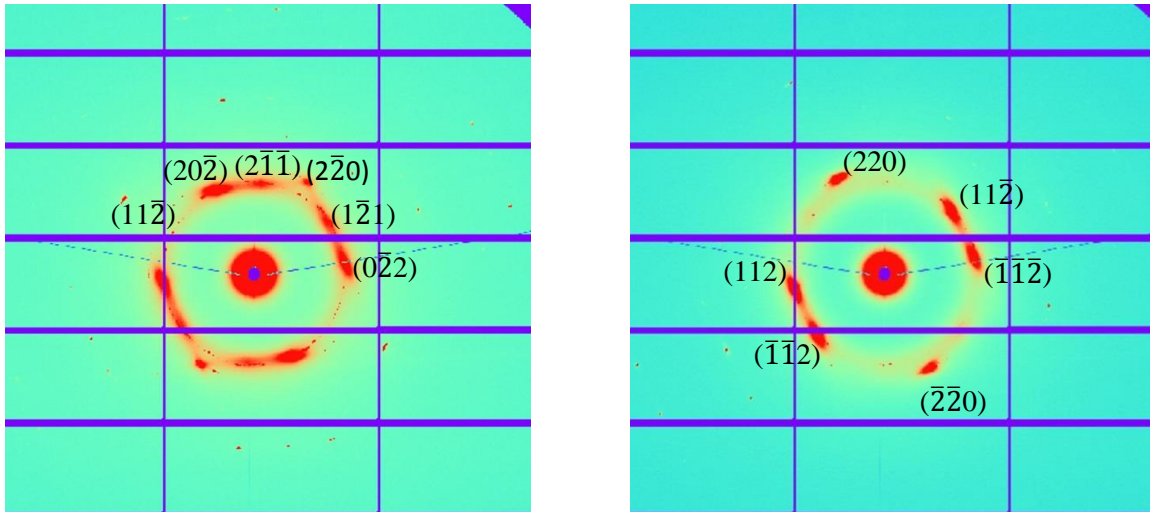


Figure 7.6 Diffraction patterns of **B13** in the diffused $Ia\bar{3}d$ phase at 232 °C, at two different positions.

7.2.4 The orthorhombic $P2_12_12_1$ phase

Compound **A4** shows complex phase transitions on first heating. The crystal melts at around 82 °C. Then four different LC phases are formed before isotropization at 128 °C. Apart from $Im\bar{3}m$, distorted $Ia\bar{3}d$ and $Ia\bar{3}d$ phases discussed before, the first LC phase upon melting of the sample was found to be orthorhombic with a $P2_12_12_1$ space group symmetry.

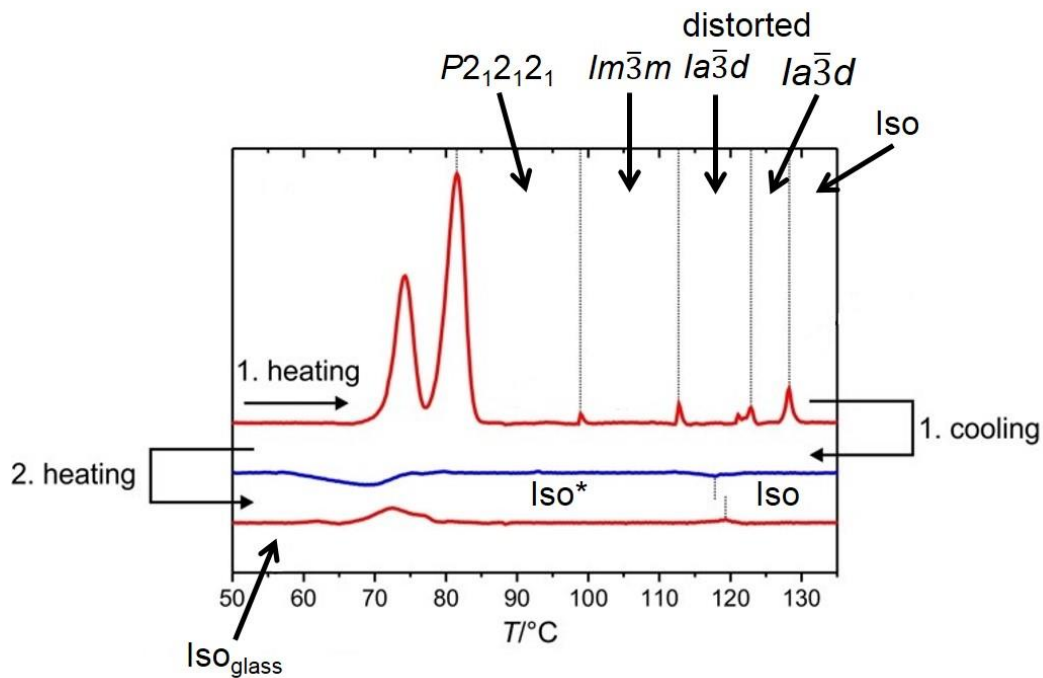


Figure 7.7 DSC traces of compound **A4**.

Determination of the lattice and space group symmetry is based on the high resolution powder diffraction pattern taken of the phase at 93 °C (Figures 7.8 and 7.9). The best-fit lattice is orthorhombic with lattice parameters $a = 134.4 \text{ \AA}$, $b = 128.9 \text{ \AA}$, $c = 59.0 \text{ \AA}$ (Table 7.5). The extinction rules found of the diffraction pattern is that only $(h00)$, $(0k0)$ and $(00l)$ peaks with odd h , k or l are extinct, and the only space group satisfy such conditions is $P2_12_12_1$.

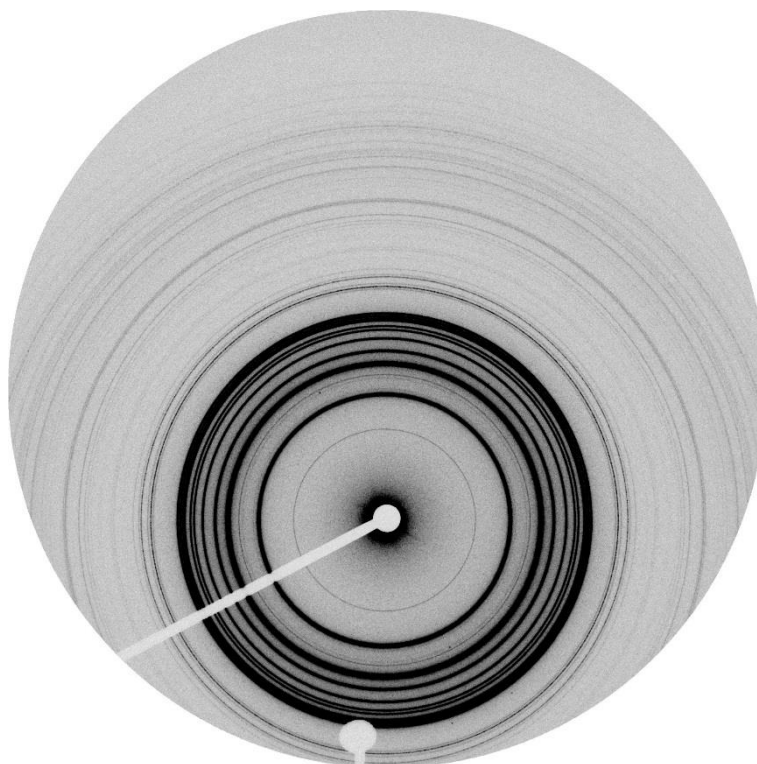


Figure 7.8 2D pattern diffraction pattern of compound **A4** at 93 °C.

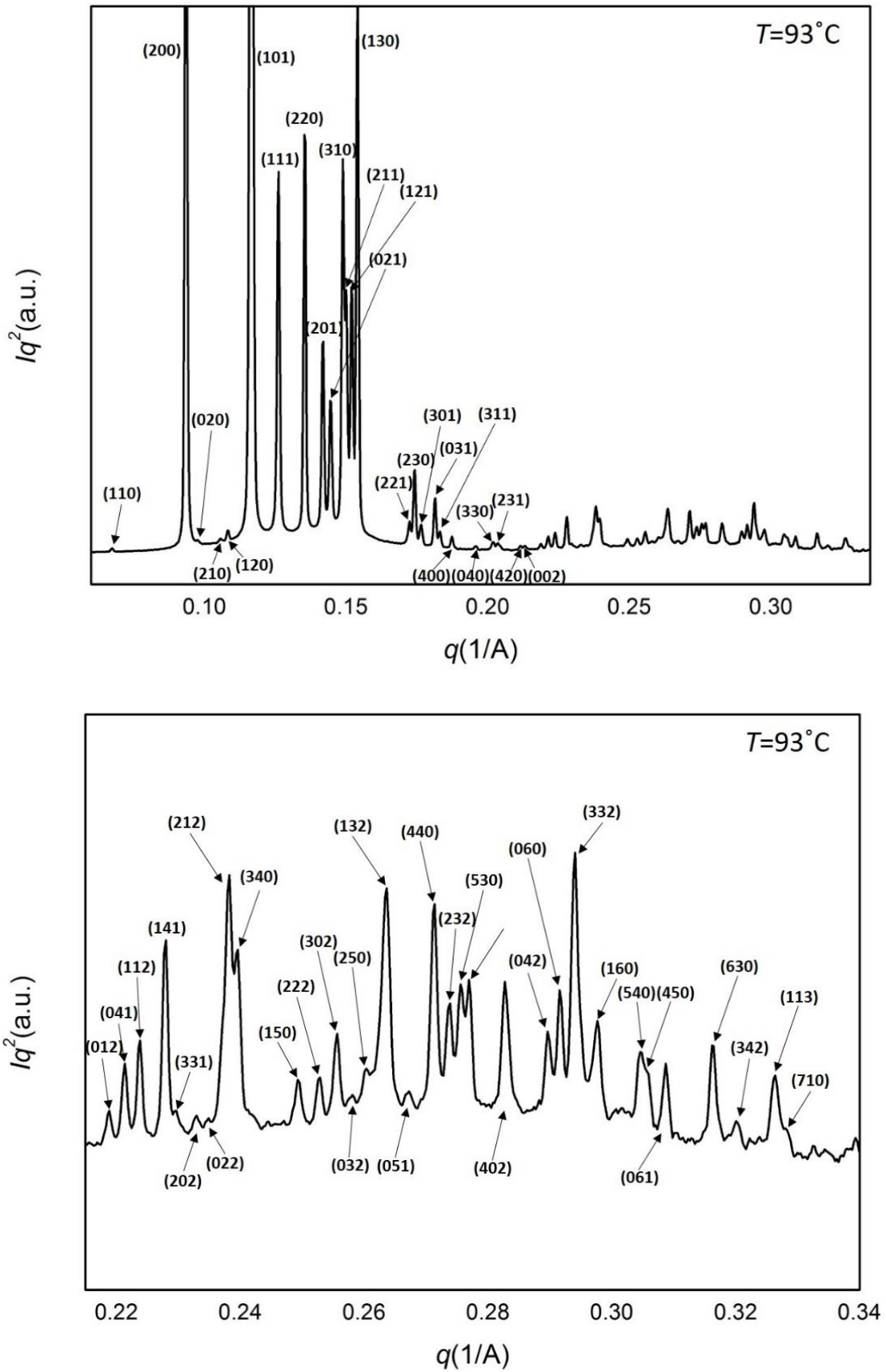


Figure 7.9 Reduced 1D diffraction pattern of compound A4 at 93°C . Peaks are marked with their corresponding indices.

Table 7.5 Indices, experimental and calculated d-spacings, and intensities of diffraction peaks of compound A4 at 93 °C. The best-fit lattice is orthorhombic with lattice parameters $a = 134.4 \text{ \AA}$, $b = 128.9 \text{ \AA}$, $c = 59.0 \text{ \AA}$.

<i>(hkl)</i>	$d_{\text{obs.}} \text{ -spacing (\AA)}$	$d_{\text{cal.}} \text{ -spacing (\AA)}$	<i>intensity</i>
(110)	93.2	93.0	0.423
(200)	67.2	67.2	62.4
(020)	64.5	64.5	0.713
(210)	59.5	59.6	0.308
(120)	58.1	58.1	0.793
(101)	54.0	54.0	100
(111)	49.9	49.8	26.3
(220)	46.4	46.5	25.8
(201)	44.3	44.3	12.3
(021)	43.5	43.5	8.79
(310)	42.2	42.3	24.5
(211)	41.9	41.9	16.2
(121)	41.3	41.4	16.8
(130)	40.8	40.9	33.1
(221)	36.5	36.5	
(230)	36.1	36.2	
(301)	35.6	35.7	
(031)	34.6	34.7	
(311)	34.3	34.4	
(400)	33.5	33.6	
(040)	32.1	32.2	
(330)	31.1	31.0	
(231)	30.9	30.9	
(420)	29.7	29.8	
(002)	29.5	29.5	
(012)	28.7	28.8	
(041)	28.4	28.3	
(112)	28.1	28.1	
(141)	27.6	27.7	
(331)	27.4	27.4	
(202)	27.0	27.0	
(022)	26.8	26.8	
(212)	26.4	26.4	
(340)	26.2	26.2	
(150)	25.2	25.3	
(222)	24.9	24.9	
(302)	24.6	24.6	
(032)	24.3	24.3	
(250)	24.1	24.1	
(132)	23.8	23.9	

(051)	23.5	23.6	
(440)	23.2	23.3	
(232)	22.9	22.9	
(530)	22.8	22.8	
(332)	22.7		
(402)	22.2	22.2	
(042)	21.7	21.8	
(060)	21.5	21.5	
(332)	21.4	21.4	
(160)	21.1	21.2	
(540)	20.6	20.6	
(450)	20.5	20.5	
(061)	20.3	20.2	
(630)	19.9	19.9	
(342)	19.6	19.6	
(113)	19.2	19.2	
(710)	19.1	19.0	
$a = 134.4 \text{ \AA}, b = 128.9 \text{ \AA}, c = 59.0 \text{ \AA}$			

Using the intensities of the four strongest peaks: (200), (101), (111) and (220), we have tentatively reconstructed the electron density map of this orthorhombic $P2_12_12_1$ phase (Figure 7.10). The map suggests a complex single network formed by rigid aromatic cores, with 3 and 4 ways junctions. However, further detailed studies of the electron density maps are needed in order to construct a realistic molecular model of the phase and to understand its relationship to other phases observed.

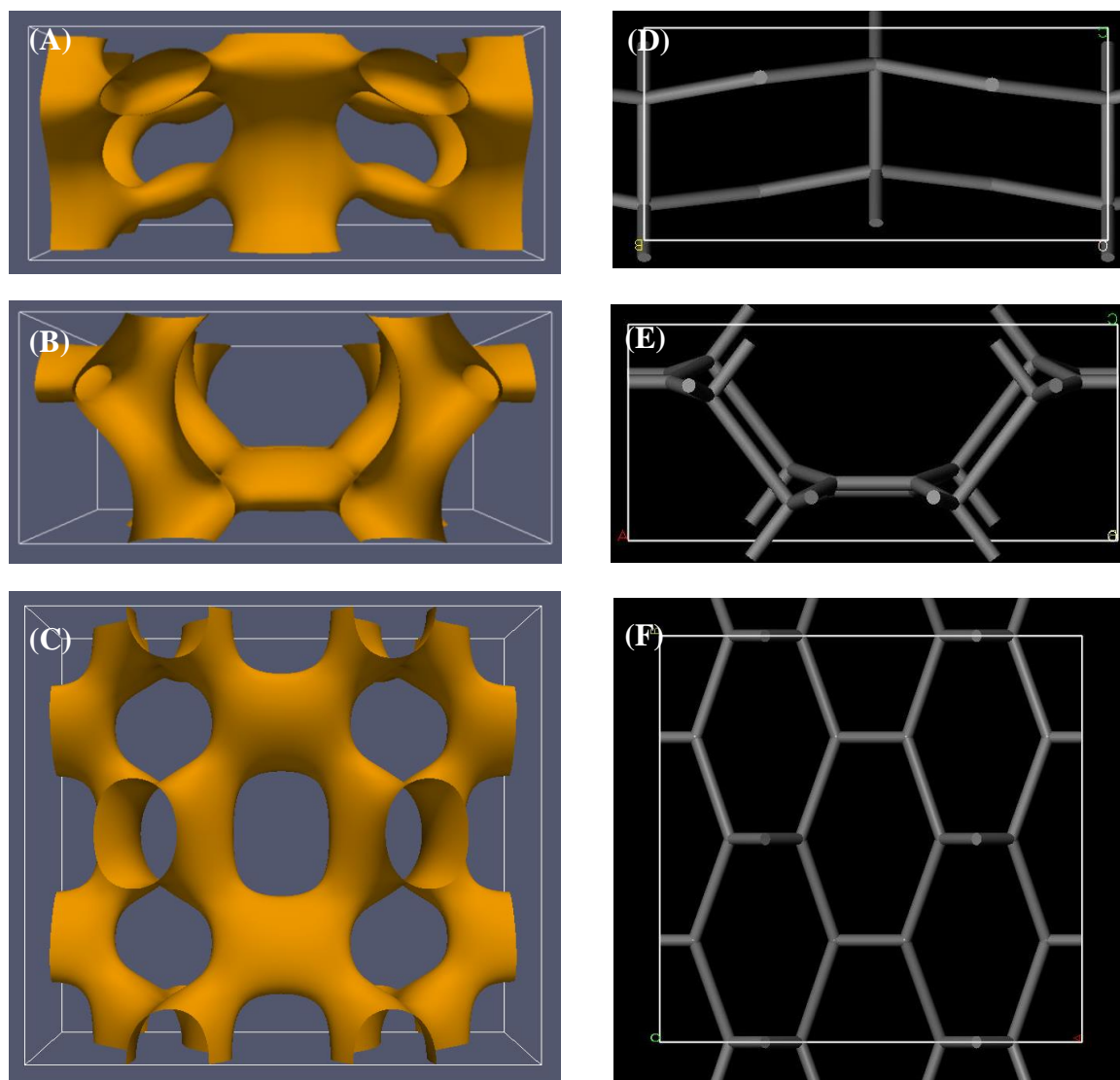


Figure 7.10 Electron density map (A-C) and corresponding network model (D-F) of the orthorhombic $P2_12_12_1$ phase of compound **A4**. The electron density map is represented by yellow isoelectron surface which encloses the high electron density (aromatic) regions in the unit cell. (A)(D), view along x -axis; (B)(E), view along y -axis; (C)(F), view along z -axis.

7.3 Conclusions

A number of previously unidentified 3D phases have been observed and characterized by SAXS in polycatenar compounds. We have been able to index the diffraction patterns and retrieve their lattice parameters, and for most of them have determined their space groups as well. For some phases we have a good idea of their molecular level structures, but for the rest there is still a lot of work to be done before their structures can be fully elucidated.

References

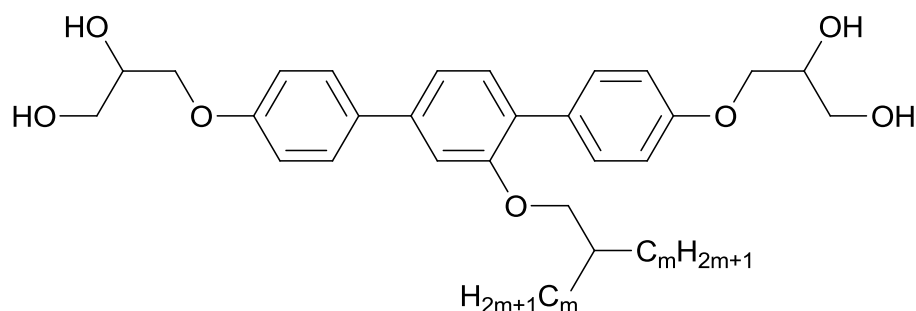
-
1. A. M. Levelut, M. Clerc, Structural investigations on 'smectic D' and related mesophases, *Liquid Crystals* **24**, 105-115 (1998).

Chapter 8

Double Gyroid and Single Diamond Network Cubic Phases Formed from Bundled Bolaamphiphiles with a Terphenyl Core and a Swallow-Tailed Side Group

8.1 Introduction

In this chapter we examine the cubic phases formed by a series of bolaamphiphiles, each with a terphenyl core, two glycerol end groups, and a swallow-tailed side group (Figure 8.1). With changing length of the side group, two different bicontinuous cubic phases were observed. With shortest side group length, a double gyroid ($Ia\bar{3}d$) cubic phase is formed; with longer side group lengths, a single diamond network cubic phase ($Fd\bar{3}m$) is found. In both cubic phases, the segments of the network is formed from the rigid aromatic cores of molecules. However, unlike that observed in polycatenar molecules, the rigid aromatic cores are parallel, instead of perpendicular to the direction of the network segment. Each network segment is in fact a bundle of rigid aromatic cores of molecules, and it connects to other network segments through hydrogen bondings between the glycerol end-groups of the molecules, while the rest of the space in the unit cell is taken by the side groups.



C16: $m = 16$; **C18:** $m = 18$; **C20:** $m = 20$; **C22:** $m = 22$

Figure 8.1 General molecular structure of bolaamphiphiles with swallow-tailed side group.

Two cubic phases, with space groups Fd3m and Ia3d are observed. The Fd3m phase has a single diamond network structure, and is found in SP135 (C22) and SP118 (C18) and a sample (SP130, C20) previously sent. In SP105 (C16) an Ia3d (double gyroid) phase is found. In all cases $a \sim 65 \text{ \AA}$, and the length of each segment is $\sim 28 \text{ \AA}$ for the Fd3m phase, and $\sim 27 \text{ \AA}$ for the Ia3d phase. This is suggesting that in both cases each segment consists of a single bundle of aromatic cores. The length of segment for Fd3m phase is longer, probably due to more segment at each junction point (4 in Fd3m and 3 in Ia3d) in the Fd3m phase.

The other low temperature LC phase found in SP118 and SP105 is the correlated layers phase ($p2mm$), with $a \sim 30 \text{ \AA}$ and $b \sim 20 \text{ \AA}$. As expected b is similar to the length of the aromatic backbone of the molecule.

8.2 Results and Discussions

The diffraction patterns were taken on first heating (on cooling generally large domains form so not suitable for accurate measurement of d-spacings and intensities) from as received samples, using a lab SAXS machine featuring a microfocus beam with Xenocs focusing mirrors, and a Bruker Vantec-2000 multiwire detector. The samples were held in 1mm glass capillaries and the sample temperature was changed stepwise during heating. The 2D diffraction patterns were reduced to 1D plots by radial integration, using FibreFix, with necessary calibration and corrections applied.

8.2.1 Compound C16

As shown in Figure 8.2, two liquid crystal phases were observed with distinct diffraction patterns in compound C16.

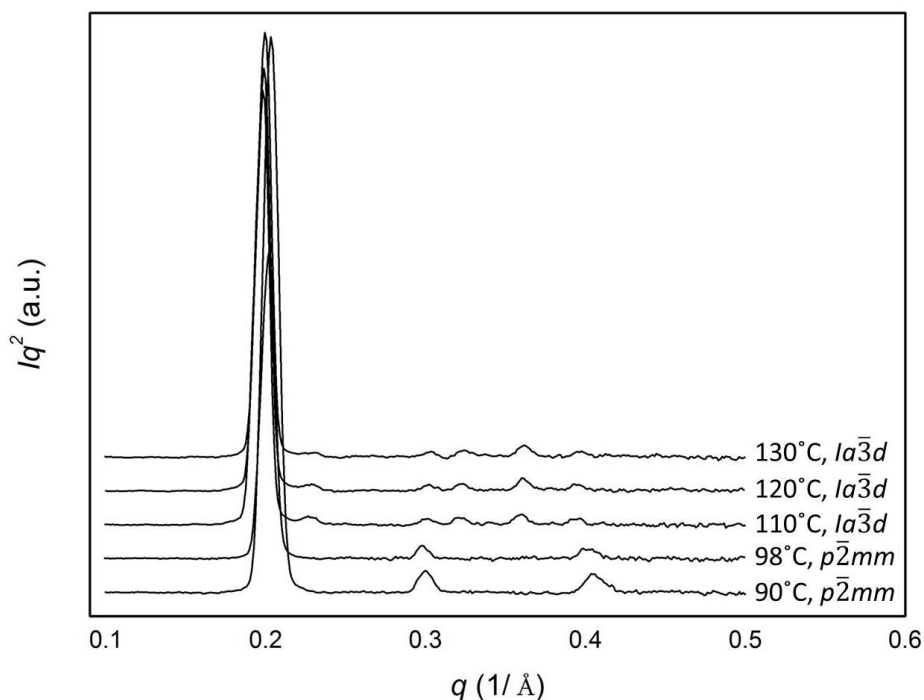


Figure 8.2 SAXS diffractograms of compound C16 from 90 °C to 130 °C during the first stepwise heating.

Only three diffraction peaks are observed for the lower temperature phase below 100 °C, and they can be assigned to the (10), (01) and (20) peaks of a 2D rectangular lattice, with lattice parameters $a = 30.9$ Å and $b = 20.9$ Å at 90 °C. (Figure 8.3 and Table 8.1). Previous studies

on bolaamphiphiles with similar size ratio between side group and the aromatic core suggest this to be the so called “lamellar smectic” phase, with $p2mm$ plane group symmetry. In the “lamellar smectic” phase, the rigid cores and the flexible side groups of the molecules separate into neighbouring layers (the lamellar structure). In the layers of rigid cores, the direction of the cores are parallel to the layer surface instead of perpendicular to it. Moreover, there is phase separation between the aromatic core and the end groups, which forms a Smectic order inside the layers of rigid cores. The lamellar thickness of 30.9 Å and the smectic layer thickness 20.9 Å match the size of the molecule. With the measured intensities and assignment plane group, the 2D electron density map was reconstructed and shown in Figure 8.4, with the schematic molecular organization overlaid on top.

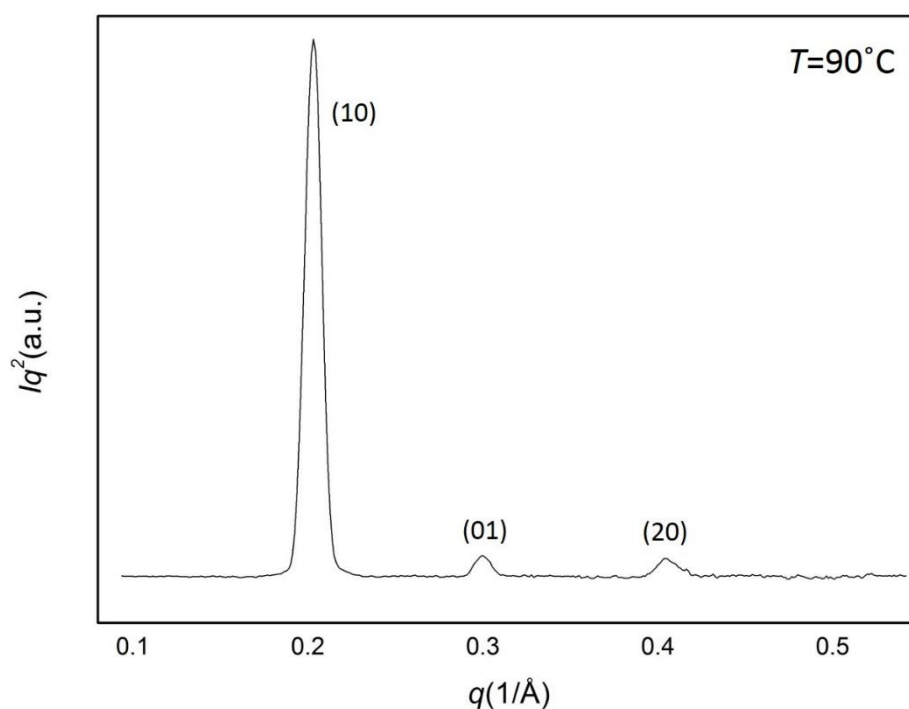


Figure 8.3 Powder diffraction pattern of compound **C16** at 90 °C.

Table 8.1 Experimental and calculated d -spacings of compound **C16** at 90 °C

(hk)	$d_{\text{obs.}}$ -spacing (Å)	$d_{\text{cal.}}$ -spacing (Å)	<i>intensity</i>	<i>phase</i>
(10)	30.9	30.9	100	π
(01)	20.9	20.9	3.43	0
(20)	15.5	15.5	3.60	0
$a = 30.9 \text{ \AA}, b = 20.9 \text{ \AA}$				

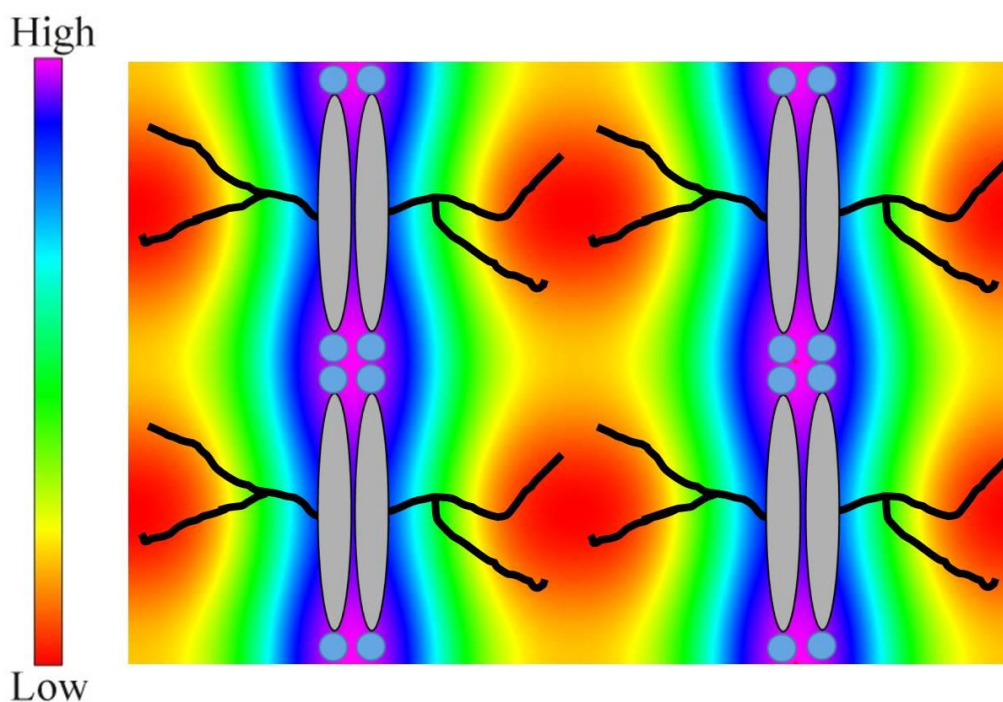


Figure 8.4 Reconstructed electron density map of the $p2mm$ phase, with schematic molecular arrangement in the structure overlaid on top.

As shown in Figure 8.5 and Table 8.2, seven diffraction peaks were observed for the high temperature phase of **C16**. The diffraction conditions observed, that $(h00)$ must have $h = 4n$, $(hk0)$ must have both h and k even, (hhl) must have $2h+l = 4n$, and (hkl) must have $h + k + l = 2n$, point to the $Ia\bar{3}d$ space group symmetry. Similar to the bicontinuous cubic phase found in polycatenar compounds, (211) is much stronger than any other diffraction peaks observed. The reconstructed electron density map is also similar, with two interpenetration gyroid networks as the high electron density regions occupied by the rigid cores of the molecules, surrounded by a continuum of low electron density of aliphatic side groups (Figure 8.6).

Even though the electron density map looks similar to that found in polycatenar compounds, the rigid cores of the molecules in this case should not be perpendicular to the network segment as this would cause a serious clash between the side groups of the molecules. Instead, the rigid cores of the molecules should lie parallel to the network segment and form a bundle, with side group fanning out laterally and occupying the space between the two networks (see schematics in Figure 8.6). The segment length is proportional to the lattice parameter a by a factor of $\sqrt{2}/4$, and can be calculated to be 27.5 \AA . This agrees extremely well with the length of the molecular backbone, which is estimated to be 28 \AA by molecular modelling.

Assuming a density of 1 g cm^{-3} of the compound, it can be calculated that there are 313 molecules in the cubic unit cell. As there are 24 network segments in the unit cell, in each segment bundle, there are on average 13 molecules.

Skeletal $Ia\bar{3}d$ cubic phase [1], and a double diamond $Pn\bar{3}m$ phase [2], have previously been found in bolaamphiphiles, with a biphenyl core and also a swallow tailed side group. There each network segment consists of two bundles connected end-to-end, instead of one bundle as observed here. The number of molecules per bundle in the previous two phases is ~ 12 , very close to what has been observed here in **C16**.

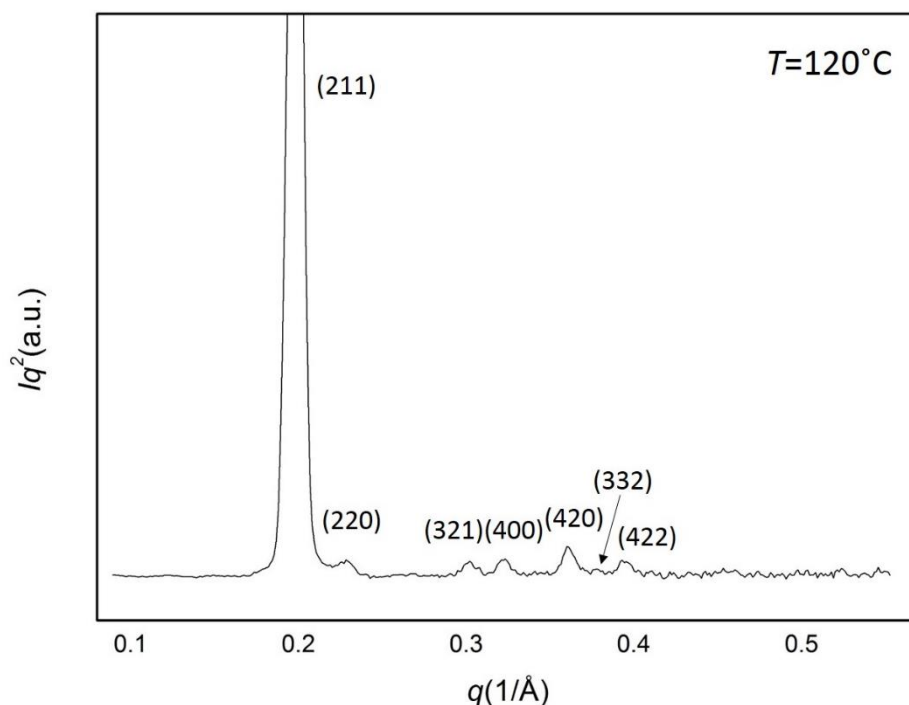


Figure 8.5 Powder diffraction pattern of compound **C16** at 120 °C can be indexed to a cubic lattice with $Ia\bar{3}d$ space group symmetry.

Table 8.2 Experimental and calculated d -spacings of compound **C16** at 120 °C ($Ia\bar{3}d$)

(hkl)	$d_{\text{obs.}} - \text{spacing } (\text{Å})$	$d_{\text{cal.}} - \text{spacing } (\text{Å})$	<i>Intensity</i>	<i>phase</i>
(211)	31.7	31.7	100	π
(220)	27.4	27.5	1.50	π
(321)	20.8	20.8	0.85	0
(400)	19.5	19.4	1.21	π
(420)	17.4	17.4	2.14	π
(332)	16.6	16.6	0.31	$0/\pi$
(422)	15.9	15.9	1.05	0
$a = 77.7 \text{ Å}$				

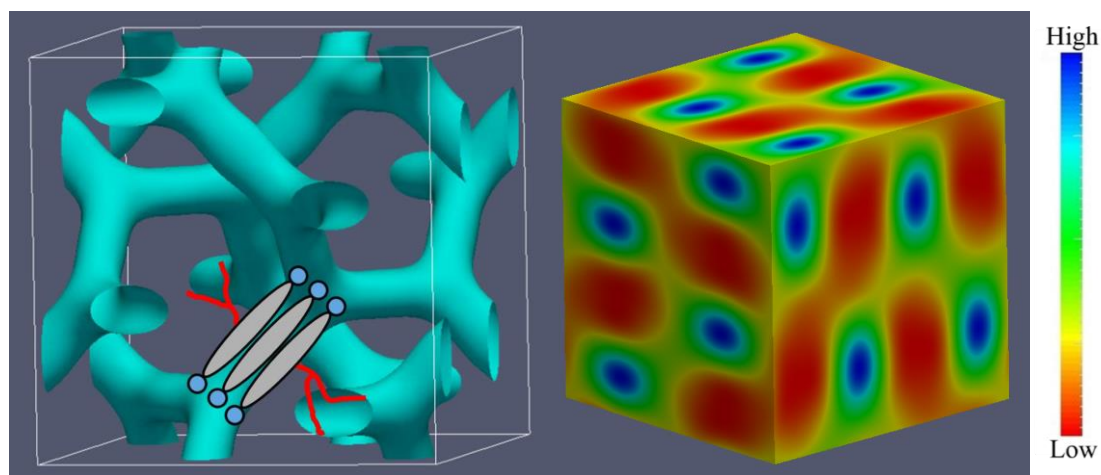


Figure 8.6 Reconstructed electron density map of the $Ia\bar{3}d$ phase of compound **C16**.

8.2.2 Compound **C18**

The SAXS diffractograms of Compound **C18** on first heating from 75 °C to 125 °C is shown in Figure 8.7. Two distinct LC phases were observed: the $p2mm$ phase at temperatures below 100 °C as observed also in **C16**, and another cubic phase at higher temperatures, with an $Fd\bar{3}m$ symmetry.

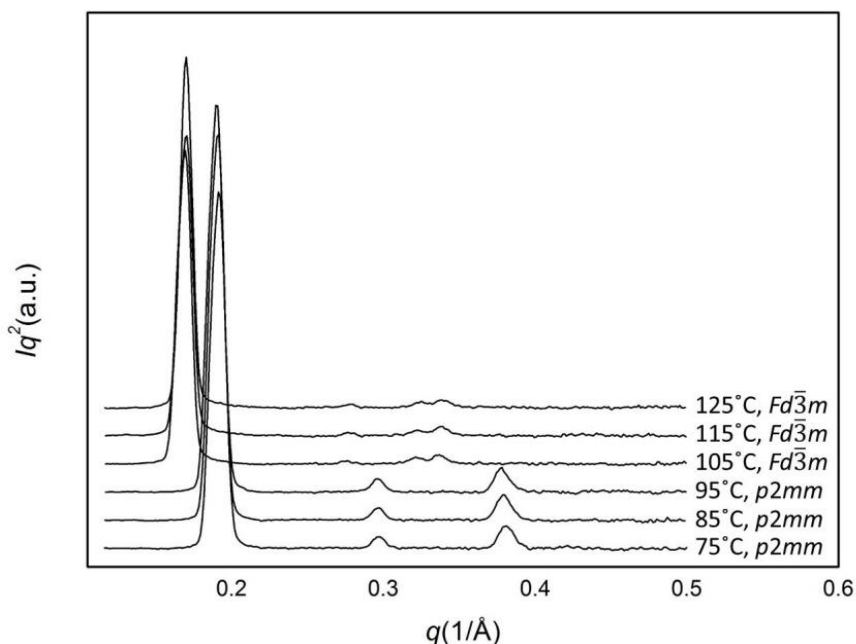


Figure 8.7 First heating run of compound **C18** from 75 °C to 125 °C.

The lower temperature $p2mm$ phase of **C18** has essentially the same structure of that observed in **C16**. The lamellar thickness a , corresponding to the separation between aliphatic

side groups and the rigid cores, increased from 30.9 Å to 33.1 Å with the increasing length of the side group; and the smectic layer thickness, corresponding to the length of the rigid cores, stayed virtually the same (20.9 Å and 21.1 Å) as expected.

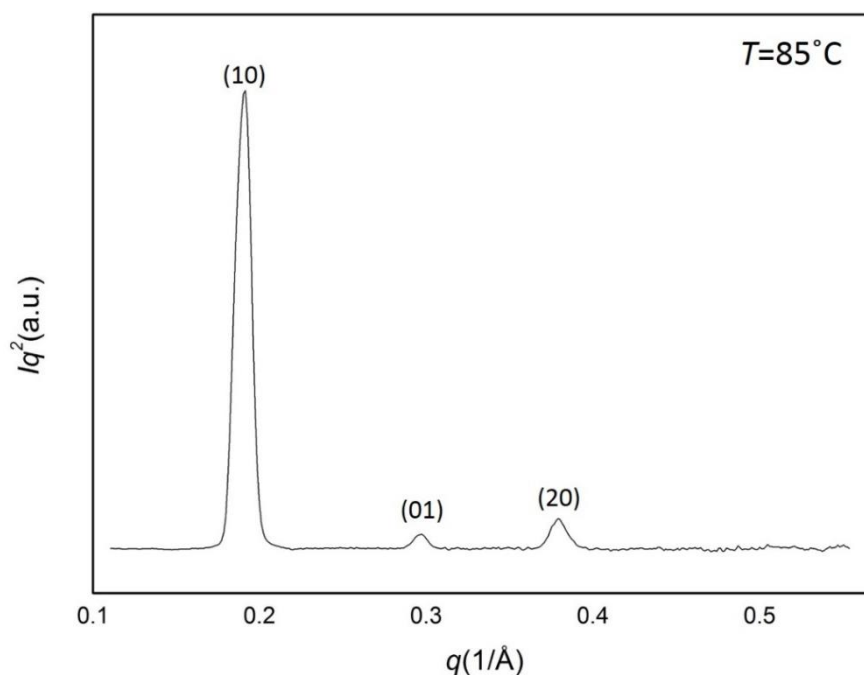


Figure 8.8 Powder diffraction pattern of compound **C18** in the $p2mm$ phase at 85 °C.

Table 8.3 Experimental and calculated d -spacings of **C18** in the $p2mm$ phase at 85 °C.

(hk)	$d_{\text{obs.}} - \text{spacing (Å)}$	$d_{\text{cal.}} - \text{spacing (Å)}$	<i>intensity</i>
(10)	33.1	33.1	100
(01)	21.1	21.1	2.55
(20)	16.6	16.6	6.59
$a = 33.1 \text{ Å}, b = 21.1 \text{ Å}$			

The higher temperature cubic phase of **C18**, however, is completely different to that found in **C16**. As shown in Figure 8.9 and Table 8.4, the four diffraction peaks observed have indices (111), (220), (311) and (222) respectively, with a lattice parameter $a = 63.9 \text{ Å}$. The extinction rule observed that (hkl) must be all even or all odd points to a face centred cubic lattice. Furthermore, (200) peak is not observed, suggesting that $(h00)$ must have $h=4n$, and the only space groups that satisfy these conditions are $F4_132$, $Fd\bar{3}$ and $Fd\bar{3}m$. We have assigned the phase to $Fd\bar{3}m$ symmetry as LC molecules tend to assemble into structures with high symmetry as it normally increases the entropy of the system.

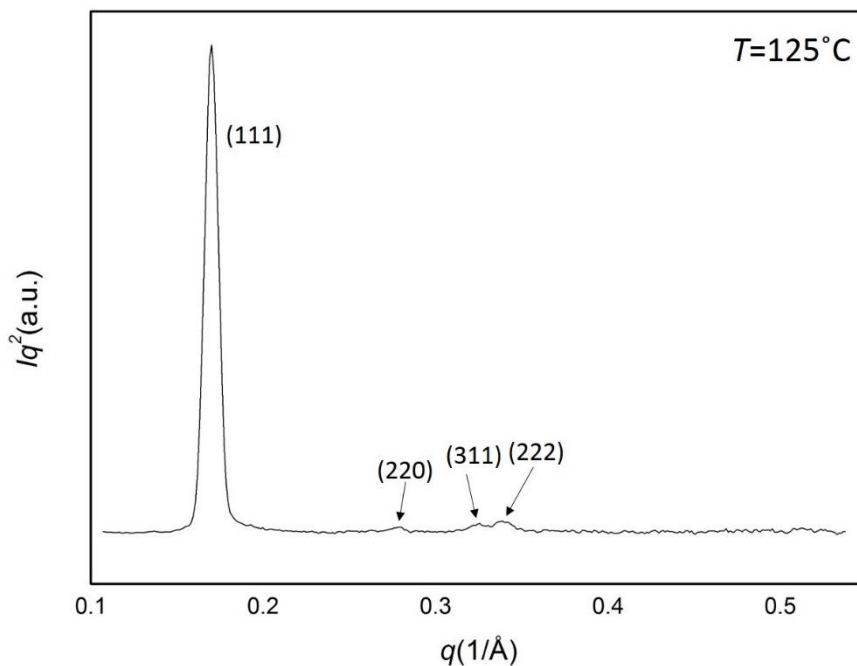


Figure 8.9 Powder diffraction pattern of compound **C18** in the $Fd\bar{3}m$ phase at 125 °C.

Table 8.4 Experimental and calculated d -spacings of **C18** in the $Fd\bar{3}m$ phase at 125 °C.

(hkl)	$d_{\text{obs.}}$ -spacing (Å)	$d_{\text{cal.}}$ -spacing (Å)	intensity	phase
(111)	36.9	36.9	100	0
(220)	22.5	22.6	0.70	π
(311)	19.3	19.3	1.46	π
(222)	18.5	18.4	2.24	0
$a = 63.9 \text{ \AA}$				

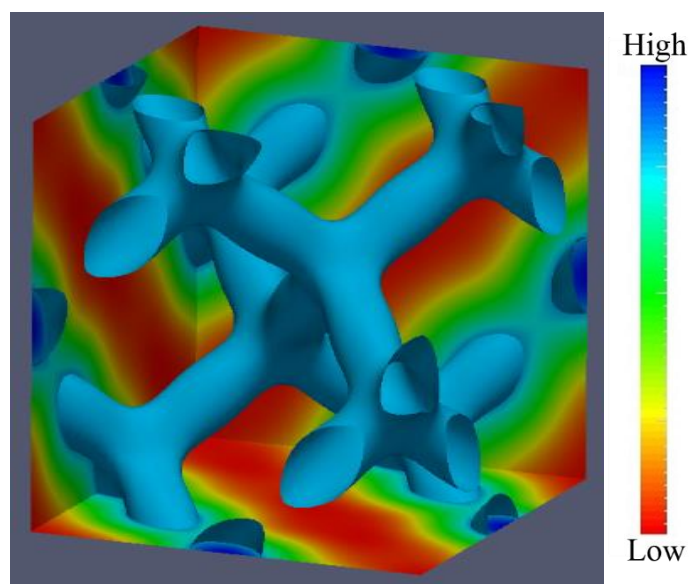


Figure 8.10 Reconstructed electron density map of the $Fd\bar{3}m$ phase of compound **C18**.

In the reconstructed electron density map of the phase (Figure 8.10), on the basis of the $Fd\bar{3}m$ space group, the high electron density regions form a network of straight segments. There are two important differences between the $Fd\bar{3}m$ network and that observed in the $Ia\bar{3}d$ phase. In the $Ia\bar{3}d$ phase there are two interpenetrating, but new intersecting, networks, but in the $Fd\bar{3}m$ phase there is only one single network. The second is that in the $Ia\bar{3}d$ phase there are three segments joining each other at one junction point, in the $Fd\bar{3}m$ phase there are four segments at each junction. It is believed that like in the $Ia\bar{3}d$ phase found in **C16**, $Fd\bar{3}m$ phase network segments are formed by bundles of rigid molecular cores, with the aliphatic side groups filling the rest of the space.

The positions of the junction points in the unit cell, is exactly the positions of carbon atoms in a diamond unit cell, and the network segments are equivalent to the covalent bondings between them. The $Fd\bar{3}m$ phase is in fact closely linked to the double diamond cubic $Pn\bar{3}m$ phase, where instead of a single diamond network, there is two interpenetrating diamond networks. Starting from the $Fd\bar{3}m$ network, one can generate the double diamond network by making of copy of the network and shift it by $(a/2,0,0)$ in the $Fd\bar{3}m$ unit cell. Therefore, we call this $Fd\bar{3}m$ phase the single diamond network cubic phase.

The length of the network segment in the $Fd\bar{3}m$ phase is proportional to the lattice parameter a with a factor of $\sqrt{3}/4$, and it can be calculated for **C18** that the segment length is 27.7Å. This value is virtually the same as found for **C16** in the $Ia\bar{3}d$ phase, and is in line with our molecular models that in both cases the network segment is formed from a bundle of molecular cores, the length of it is determined as a consequence by the length of the rigid molecular core. The number of molecules in each segment/bundle is found to be 10, slightly fewer than the 13 in the $Ia\bar{3}d$ phase of **C16**.

It should be noted that cubic phase with $Fd\bar{3}m$ space group has been observed before in Lyotropic systems [3]. However, there the surfactant molecules form spherical micelles instead of being continuous in our case. This $Fd\bar{3}m$ phase is the first bicontinuous single diamond network cubic phase in liquid crystals, including both thermotropic and lyotropic.

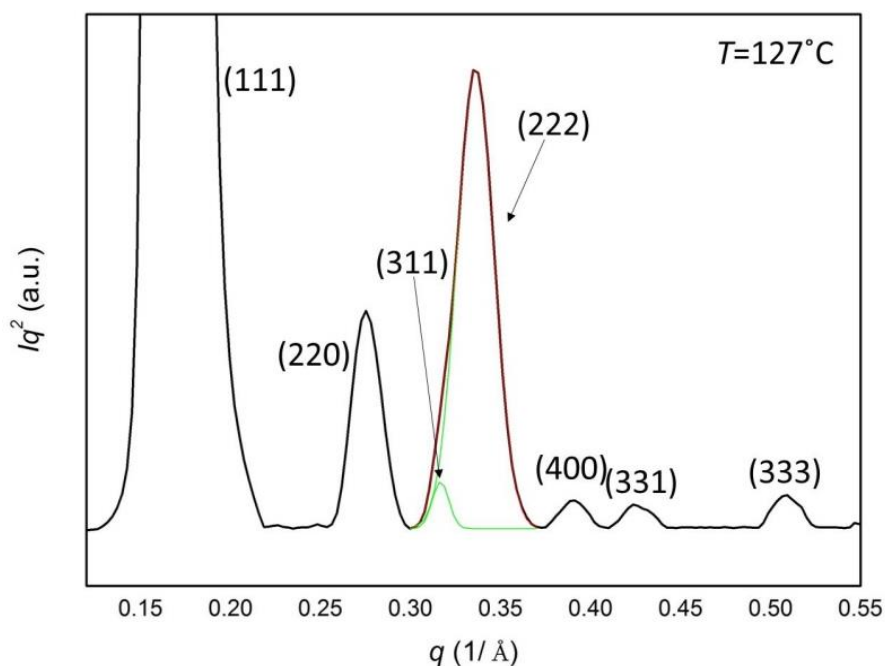
8.2.3 Compound **C20**

Figure 8.11 Powder diffraction pattern of **C20** in the $Fd\bar{3}m$ phase at 127 °C.

Table 8.5 Experimental and calculated d -spacings of the $Fd\bar{3}m$ phase in **C20** at 127 °C.

(hkl)	$d_{\text{obs.}}$ –spacing (Å)	$d_{\text{cal.}}$ –spacing (Å)	Intensity	Phase
(111)	37.4	37.4	100	0
(220)	22.8	22.9	1.84	π
(311)	19.8	19.5	0.230	π
(222)	18.7	18.7	5.22	0
(400)	16.1	16.2	0.189	0
(331)	14.8	14.9	0.167	0
(333)	12.4	12.5	0.247	0
$a = 64.8 \text{ \AA}$				

In compound **C20**, only $Fd\bar{3}m$ phase is found. The lattice parameter (Table 8.5) is very slightly increased to 64.8 Å (63.9 Å in **C18**), with segment length 28.1 Å (27.7 Å in **C18**). Again, this is in line with our proposed model of the phase. There are 10 molecules in each bundle/segment, the same as in **C18**. In this compound seven diffraction peaks, (111), (220), (311), (222), (400), (331) and (333) are observed, consistent with the $Fd\bar{3}m$ space group. The reconstructed electron density map (Figure 8.12), shows clearly the single diamond network formed by rigid molecular cores.

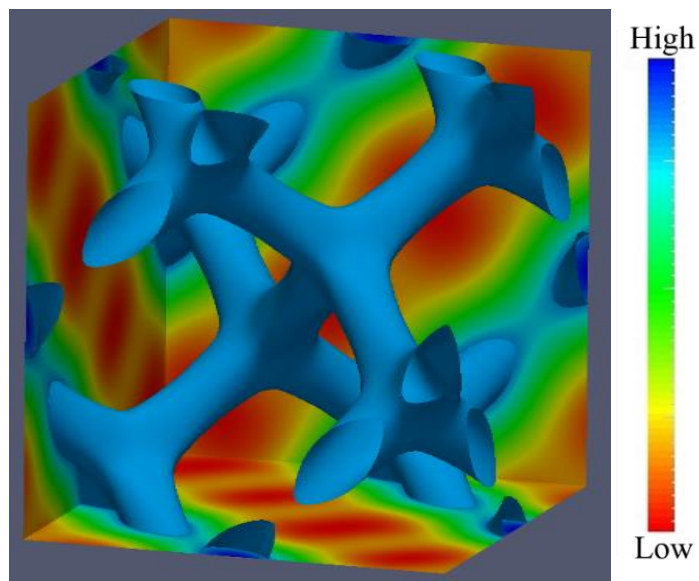


Figure 8.12 Reconstructed electron density map of the $Fd\bar{3}m$ phase of **C20**.

8.2.4 Compound **C22**

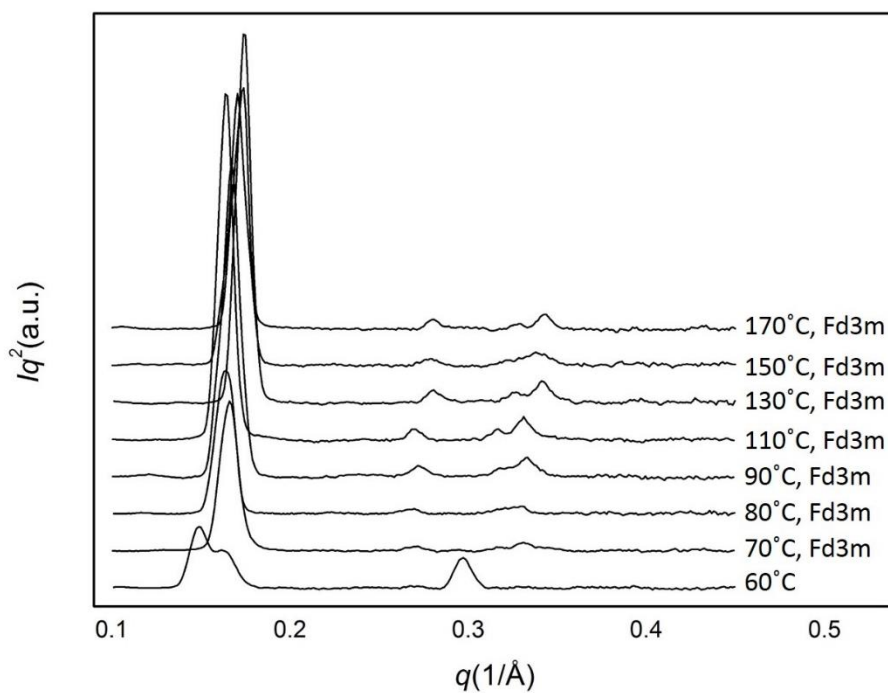


Figure 8.13 SAXS diffractograms of **C22** from 60 °C to 170 °C in the first heating scan.

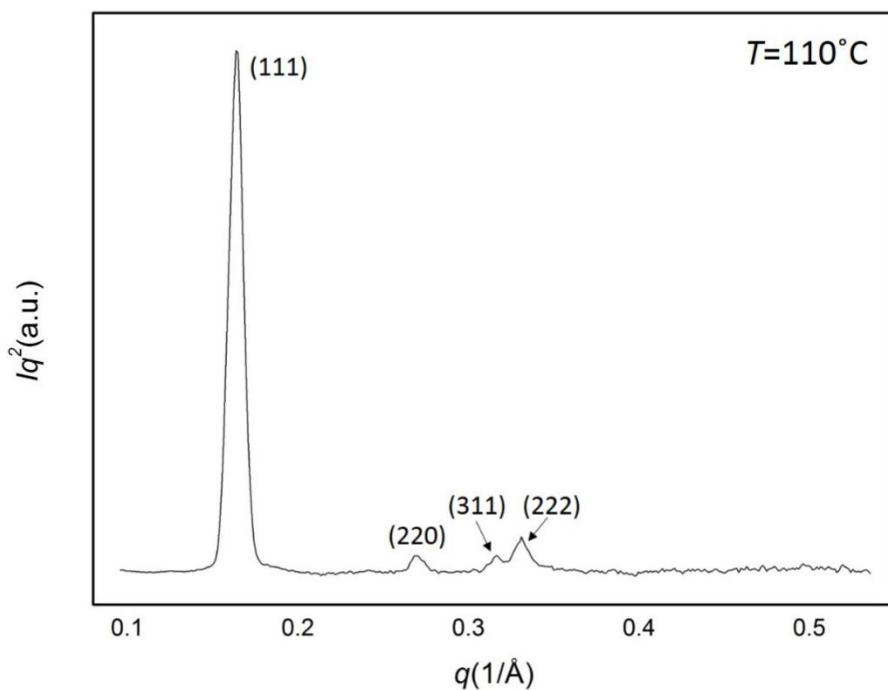


Figure 8.14 Powder diffraction pattern of **C22** in the $Fd\bar{3}m$ phase at 110 °C.

Table 8.6 Experimental and calculated d -spacings of **C22** in the $Fd\bar{3}m$ phase at 110 °C

(hkl)	$d_{\text{obs.}}$ -spacing (Å)	$d_{\text{cal.}}$ -spacing (Å)	<i>intensity</i>	<i>phase</i>
(111)	38.3	38.3	100	0
(220)	23.3	23.4	2.57	π
(311)	19.9	20.0	2.50	π
(222)	19.0	19.1	6.18	0
$a = 66.3 \text{ \AA}$				

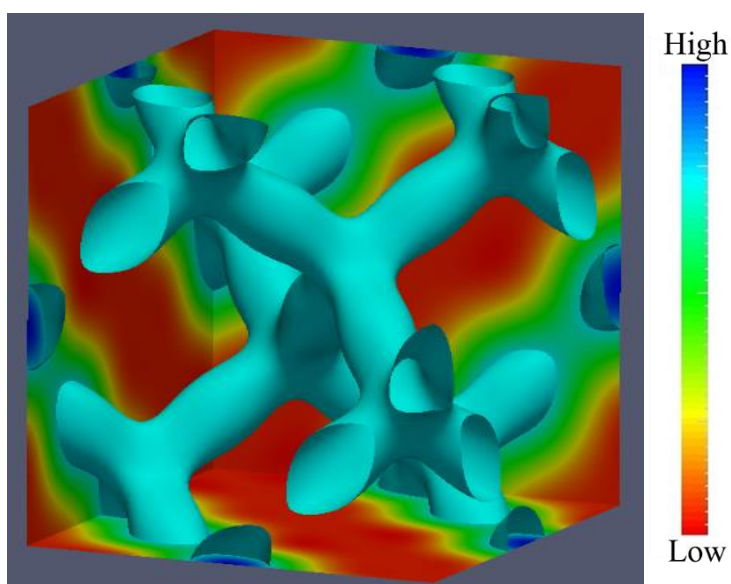


Figure 8.15 Reconstructed electron density map of the $Fd\bar{3}m$ phase of **C22**.

In compound **C22**, only LC phase found is the $Fd\bar{3}m$ phase. The lattice parameter a (Table 8.6) is increased to 66.3 Å (63.9Å in **C18**), with segment length 28.7 Å (27.7Å in **C18**). Again, there are 10 molecules in each bundle/segment, the same as in **C18** and **C20**. The reconstructed electron density map is shown in Figure 8.15.

8.3 Conclusion

A series of bolaamphiphiles, with a terphenyl core, two glycerol end groups, and a swallow-tailed side group of different lengths, were studied. Three different LC phases were observed, including two bicontinuous cubic phases with $Ia\bar{3}d$ and $Fd\bar{3}m$ space group symmetries, respectively. In both cubic phases, the rigid cores of the molecules (about 10 of them) come together and form a bundle, and these bundles connected with each other through H-bonding between their end-groups, and form networks. While in the $Ia\bar{3}d$ phase there are two interpenetrating networks, in the $Fd\bar{3}m$ phase there is only one, the first of its kind in liquid crystals.

Reference

1. F. Liu, M. Prehm, X. B. Zeng, C. Tschierske, G. Ungar, *J. Am. Soc. Chem.* **136**, 6846–6849 (2014).
2. X. B. Zeng, M. Prehm, G. Ungar, C. Tschierske, F. Liu, *Angew. Chem. Int. Ed.* **55**, 8324–8327 (2016).
3. P. M. Duesing, R. H. Templer, J. M. Seddon, *Langmuir* **33**, 351-359 (1997).

Conclusions and Future Work

The results presented in this PhD thesis show how simple modifications of classic liquid crystalline compounds could lead to a variety of 2D and 3D complex modes of self-assembly. The determination of such structures and understanding of how molecules self-assemble to form such phases have provided us unprecedented insight into the controlling parameters of such phases. For example, there is now strong evidence to support that helical columns formed by polycatenar compounds is in fact a universal underlying feature of all bicontinuous phases they form.

X-shaped polyphiles, composed of a rigid aromatic rod and two flexible lateral chains, have been found to form a series of 2D and 3D structures at different temperatures. The mesophase separation is caused by the incompatibilities of different moieties in the molecules. As the temperature influences in varying degrees on the volumes of the lateral chains, structures with different symmetries can be formed. 2D “single colour” and “two colour” (chessboard-like) square honeycombs, as well as rhombic honeycombs are observed. Also, 2D-3D transitions take place, resulting in distorted columns or a “double-wigwam” cage-like tetragonal phase.

Polycatenar liquid crystalline molecules usually consist of a long rigid rod-like aromatic central core and a number of flexible side chains in terminal positions. In polycatenars, the highly conjugated aromatic cores of the neighboring molecules are attracted together due to van der Waals forces. This attraction leads to microphase separation and results in the formation of liquid crystal structures. A variety of mesogenic phases can be observed by changing the length or number of the terminal chains. Here, the achiral bicontinuous $Ia\bar{3}d$ phase, the chiral tri-network $Im\bar{3}m$ phase and many complex 3D phases, such as SmQ, $P2_12_12_1$, distorted $Ia\bar{3}d$, distorted $Im\bar{3}m$ phase, are observed. Also, the dynamic mirror symmetry breaking phenomena is found in the isotropic liquid formed by achiral polycatenar liquid crystalline compounds, which leads to the formation of the chiral isotropic phase.

For the swallow-tailed T-shaped bolaamphiphiles, three different LC phases were observed, including two bicontinuous cubic phases with $Ia\bar{3}d$ and $Fd\bar{3}m$ space group symmetries, respectively. In both cubic phases, the rigid cores of the molecules come together and form a bundle, and these bundles connected with each other through H-bonding between their end-

groups, and form networks. While in the $Ia\bar{3}d$ phase there are two interpenetrating networks, in the $Fd\bar{3}m$ phase there is only one, the first of its kind in liquid crystals.

The current project also points to many directions to further explore and some of them are listed below.

In X-shaped molecules

- Study of critical transitions between single and two-coloured honeycomb columns with square cross-sections.
- Design molecules for “multi-colour” columnar liquid quasicrystals.

In polycatenar compounds

- Study, more quantitatively, the transitions from chiral isotropic phases to bicontinuous cubic phases by spectroscopy. This should be combined with molecular modelling.
- Determine the structures of a number of newly discovered non-cubic phases and achieve a better understanding of their relationship to previously known bicontinuous cubic phases.

In bolaamphiphiles

- Understand the parameters that control the formation of the single network cubic phases and how it is linked to double network cubic phases.
- Design molecules that can possibly form other single network cubic/non-cubic phases.